CERN-THESIS-2011-295

DISS. ETH NO. 19538

Evaluation of Particle Yields in 30 GeV Proton–Carbon Inelastic Interactions for Estimating the T2K Neutrino Flux

A dissertation submitted to

ETH Zurich

for the degree of

Doctor of Sciences

by

Claudia Strabel

Dipl. Phys. Goethe University Frankfurt/M.

Born on 7th of July, 1982

Citizen of Germany

Accepted on recommendation of

Prof. André Rubbia, examiner

Prof. Günther Dissertori, co-examiner

2011

Abstract

The NA61/SHINE (SPS Heavy Ion and Neutrino Experiment) experiment at the CERN SPS combines a rich physics program in various fields. One of its main purposes is to perform hadron production measurements in proton–carbon interactions targeted for an accurate neutrino flux prediction of the T2K experiment in Japan.

T2K is a long baseline neutrino oscillation experiment at J-PARC, Japan, with the aim to precisely measure the $\nu_\mu \rightarrow \nu_e$ appearance and ν_μ disappearance. To generate neutrinos, a high intensity 30 GeV proton beam impinging on a 90 cm long carbon target is used, whereby hadrons (π, K, etc) are produced, which decay into neutrinos ($\nu_{\mu,e}$). The neutrino flux is then measured 2.5° off-axis, both, in a near detector, located 280 m behind the target, and in the 295 km far away Super-Kamiokande detector (SK). Neutrino oscillations can be probed by comparing the neutrino flux measured at SK to the one predicted at SK. In order to predict the flux at SK one uses the near detector measurements and extrapolates them with the help of Monte Carlo (MC) predictions to SK. Up to now, these MC predictions depend on hadron production models of deficient predictive power. For more precise predictions, measurements of the hadron production off the carbon target are essential to tune the available MC codes. The aim of the NA61/SHINE measurements for T2K is to provide these hadro-production measurements.

The NA61 detector is a large acceptance hadron spectrometer at the CERN SPS. Its main components represent four large volume time projection chambers (TPCs), which provide high momentum resolution and good particle identification (PID) via specific energy loss measurements. The PID capability of the TPCs is complemented through time-of-flight measurements of various detector arrays. Two carbon targets of different lengths are used, a 2 cm long target, the so called thin target, and a 90 cm long T2K replica target. The latter allows to study the full particle yield in the T2K target, including primary as well as higher order interactions, while the thin target allows to evaluate the primary particle production in proton–carbon collisions without distortions due to target reinteractions. The proton–carbon cross section measurements are not only important for determining the direct contribution–the largest one–to the neutrino flux in T2K, but are of great interest on their own right.

During the pilot run in October 2007 approximately 660k events with the thin target and 230k events with the T2K replica target were registered with a 30 GeV proton beam. Upon successful completion of the test run, efforts were joined for the calibration and analysis of the thin target data to extract first results on the inclusive particle cross sections and the mean

multiplicities in inelastic interactions.

For the determination of the inclusive hadron production and the mean multiplicities from the measured particle yields, various steps of normalization and corrections are indispensable. These steps followed to obtain the normalized spectra of the different particle types are the main subject of this thesis and will be described in detail. One of the main results is the determination of the total inelastic proton–carbon cross section.

Zusammenfassung

Das NA61/SHINE (SPS Heavy Ion and Neutrino Experiment) Experiment am CERN SPS umfasst ein umfangreiches Forschungsprogramm in verschiedenen Bereichen der Physik. Eines seiner Hauptziele stellt die Messung der Hadronenproduktion in Proton–Kohlenstoff Kollisionen für eine präzise Vorhersage des Neutrinoflusses des T2K Experiments in Japan dar.

T2K ist ein Neutrinooszillationsexperiment am J-PARC in Japan, welches das Ziel verfolgt die $\nu_\mu \rightarrow \nu_e$ und $\nu_\mu \rightarrow \nu_{x\neq\mu}$ Oszillation genau zu messen. Mit Hilfe eines hochenergetischen Protonenstrahls (30 GeV), der auf ein 90 cm langes Kohlenstofftarget gerichtet ist, werden Hadronen (π, K, etc) produziert, die in Neutrinos ($\nu_{\mu,e}$) zerfallen. Der somit erzeugte Neutrinofluss wird unter einem Winkel von 2.5° zur Strahlachse in einem nahe gelegenen Detektor, 280 m hinter der Hadronenproduktion, und einem weiteren, dem Super-Kamiokande Detektor (SK), 295 km entfernt, gemessen. Neutrinooszillationen werden untersucht, indem man den Neutrinofluss, den man in SK gemessen hat, mit Vorhersagen vergleicht. Letztere basieren auf den Messungen des nahgelegenen Detektors, welche mittels Monte Carlo (MC) Simulationen zum SK-Detektor extrapoliert werden. Bisher hängen diese Simulationen von Modellen zur Hadronenproduktion ab, welche unzulängliche Vorhersagekraft aufweisen. Um genauere Vorhersagen erreichen zu können, werden Messungen der Hadronenproduktion in Proton–Kohlenstoff Reaktionen benötigt. Solch Messungen könnten dann dazu verwendet werden, die MC Simulationen zu präzisieren. Das Ziel des NA61/SHINE Experiments in Bezug auf T2K besteht darin, die gefragten Hadronenproduktionsmessungen durchzuführen.

Der NA61 Detektor ist ein magnetisches Spektrometer am CERN SPS mit einer großen Akzeptanz für geladene Hadronen. Als Hauptbestandteile des Detektorsystems dienen vier großvolumige Spurendriftkammern (TPCs), die eine hohe Impulsauflösung und Identifizierung geladener Teilchen anhand ihres spezifischen Energieverlustes bieten. Die Teilchenidentifikation in den TPCs wird zugleich durch die Flugzeitinformationen einer Reihe von Szintillationsdetektoren unterstützt. Als Target dient ein 2 cm langes Kohlenstofftarget als auch ein 90 cm langes Kohlenstofftarget, das eine Nachbildung des T2K Targets ist. Mit Letzterem kann die gesamte Teilchenproduktion in dem T2K Target untersucht werden, die sich aus den primär und sekundär (oder höherer Ordnung) erzeugten Teichen zusammensetzt. Mit dem kurzen Target lässt sich die primäre Teilchenproduktion in Proton–Kohlenstoff Kollisionen ohne Verzerrung durch Sekundärwechselwirkungen mit dem Target bestimmen. Die Messung des Proton–Kohlenstoff Wechselwirkunsquerschnitts ist nicht nur bedeutend für die Bestimmung des direkten Beitrags zum Neutrinofluss in T2K, welcher den größten Anteil ausmacht,

sondern ist auch als unabhängiges Resultat von Interesse.

Während der ersten Messzeit von NA61 im Oktober 2007 wurden ungefähr 660k Ereignisse mit dem kurzen Target und 230k mit der T2K Targetnachbildung mit einem 30 GeV Protonenstrahl aufgenommen. Daraufhin wurden die Daten kalibriert und analysiert um erste Ergebnisse für die inklusiven Wirkungsquerschnitte und die mittlere Multiplizität verschiedener Teilchensorten zu erhalten.

Um die inklusiven Wirkungsquerschnitte und die mittlere Multiplizität bestimmter Teilchen aus den gemessenen Teilchensprektren bestimmen zu können, müssen sie entsprechend normalisiert und bezüglich verschiedener Effekte korrigiert werden. Die einzelnen Schritte, die dazu notwendig sind, bilden den Hauptbestandteil dieser Arbeit und werden im Detail beschrieben. Eines der Hauptresultate ist die Messung des totalen inelastischen Proton–Kohlenstoff Wirkungsquerschnitts.

Acknowledgements

At this concluding stage of my studies I would like to express my gratitude to all of those who have supported me during my Ph.D. in many ways and have therewith contributed to this work. This gratitude is first of all directed towards André Rubbia for giving me the opportunity to work on this interesting project. Thank you for your valuable suggestions, knowledge of this subject and for supporting and encouraging me to participate in the many informative and interesting conferences and courses, which greatly helped me to advance in the work and understanding of the topic. I owe a great debt to Alberto Marchionni for his supervision and continuous comprehensive support throughout my work. Your ideas and explanations formed an indispensable basis for this analysis.

Thanks to Andreas Badertscher for his critical literary eye when reading drafts of this thesis. I also want to thank Ben Still, not only for proof-reading, but for his many instructive and inspiring discussions and explanations on physics and T2K.

I am fortunate to have been able to work with my colleagues at ETH, who each contribute in their own way to making it a pleasant working environment. Thanks to all of you and in particular to Luigi Esposito and Silvestro di Luise for their patience when giving computing and programming advice.

This analysis would not have been possible without the great effort and hard work of the members of the NA61 collaboration. I want to thank Marek Gazdzicki and Boris Popov particularly for their valuable suggestions, which helped me to progress with this work. I am indebted to Anselmo Meregaglia for his advice and cooperative support on this analysis. Furthermore, I highly appreciate having worked together with Nicolas Abgrall and Sebastien Murphy. Thank you for the memorable time.

I am deeply thankful for the support and encouragement I have received from my family and friends in all circumstances. It is the basis for all I have reached.

Contents

Chapter 1

Introduction

The neutrino was born in 1930, when Wolfgang Pauli postulated the existence of a light neutral particle with spin $^1/_2$ in order to save energy and angular momentum conservation in β-decay. A theoretical framework for this concept was first given by Enrico Fermi in 1934, who incorporated Pauli's neutral particle into a dynamical theory and named it neutrino – little neutral one [1]. Fermi's theory postulated a pointlike, four-fermion interaction with a weak coupling strength. It has since evolved into the Glashow-Weinberg-Salam (GWS) model of electroweak interactions where the pointlike Fermi interaction is instead mediated by either the neutral Z^0 boson or one of the charged $W^{\pm}$ bosons, with a coupling strength unified with the electromagnetic one. Together with the model of strong interactions, the GWS model forms the basis of what is nowadays known as the Standard Model of particle physics [2]. This model describes subatomic processes in terms of gauge interactions between quarks, charged leptons and neutral leptons, the neutrinos. Since its development in the 1970s the Standard Model has withstood a vast amount of experimental challenges, however it has also been demonstrated that it falls short of being a complete theory. Experimental data in the neutrino sector has thoroughly overturned the Standard Model picture of massless, left-handed, flavor-conserving neutrinos. Neutrinos therefore afford an outstanding opportunity to study physics beyond the Standard Model, which is of great importance not only for particle physics, but also for astrophysics and cosmology.

Sections 1.1, 1.2 and 1.3 introduce possible extensions of the Standard model so as to allow for neutrino masses, flavor mixing and neutrino oscillations. Current knowledge of experimental observations on neutrino oscillations are discussed in Section 1.4. Despite fundamental discoveries, a series of essential questions remain to be addressed. The ones directly connected to the long-baseline accelerator experiment T2K [3] will be summarized and future perspectives of neutrino oscillation experiments will be delineated. As the present generation accelerator neutrino experiments, such as T2K, enter a new domain of precision, systematic uncertain-

ties on the neutrino beam become more relevant. Sections 1.5 and 1.6 respectively describe the general concept of such accelerator neutrino beams and discuss why hadron production measurements are of importance for lowering their systematic uncertainties.

1.1 Neutrino Mass

In the Standard Model neutrinos are assumed to be massless particles, which alongside respective charged leptons form chirally left-handed weak isospin doublets that couple to the weak gauge bosons. Compelling experimental evidence of neutrinos changing from one flavor to another, however, demands neutrinos to have masses and to mix [4]. In order to accommodate neutrino masses one therefore has to go beyond the Standard Model and extend the theoretical framework by a mass term.

A priori, the most straightforward solution is to employ the same standard Higgs mechanism which generates masses of the other massive particles in the Standard Model and to construct a Dirac mass term. The Dirac mass term includes a right-handed component, which then allows the neutrino to acquire its mass from the left-right coupling to the Higgs field

$$\mathcal{L}_D = -m_D(\overline{\nu_R}\nu_L + \overline{\nu_L}\nu_R) \quad . \tag{1.1}$$

Here, ν_L and ν_R denote the chirally left- and right-handed neutrinos, respectively. The Dirac mass m_D is the coupling constant from the neutrino's coupling to the Higgs field, which has gauge quantum numbers from the electroweak coupling to the left-handed neutrino. It conserves the total lepton number $L = L_e + L_\mu + L_\tau$, that distinguishes neutrinos and negatively-charged leptons on the one hand from antineutrinos and positively-charged leptons on the other hand. Therefore, each Dirac neutrino mass eigenstate ν_i $(i = e, \mu, \tau)$ differs from its antiparticle $\overline{\nu_i}$ with the difference being that $L(\overline{\nu_i}) = -L(\nu_i)$.

The fact that neutrinos do not carry any electric charge also allows to assume that neutrinos are their own antiparticles. Such a symmetry between particles and antiparticles is possible only if the particle is void of gauge couplings, as the right-handed neutrino would be. Thus, once the right-handed neutrino has been included in the Standard Model, a Majorana mass term of the form

$$\mathcal{L}_M = -\frac{1}{2}M\left(\overline{N_R}N_R^{\mathcal{C}} + \overline{N_R^{\mathcal{C}}}N_R\right) \quad . \tag{1.2}$$

can be constructed out of the right handed neutrino N_R and its charge conjugate $N_R^{\mathcal{C}} = i\gamma^0\gamma^2\left(\overline{N_R^T}\right)$. In this term M corresponds to the Majorana mass. Since both N_R and $\overline{N_R^{\mathcal{C}}}$ absorb neutrinos and create antineutrinos, the Majorana mass term mixes neutrinos and antineutrinos. The Majorana mass term does therefore not conserve the total lepton number.

If one however does not adhere to total lepton number conservation, then it could be feasible that such Majorana neutrino masses are being generated.

Both Dirac and Majorana formalisms can be combined into a single term according to

$$\mathcal{L}_{DM} = -\frac{1}{2}\left(\overline{\nu_L} \quad \overline{N_R^{\mathcal{C}}}\right)\begin{pmatrix} 0 & m_D \\ m_D & M \end{pmatrix}\begin{pmatrix} \nu_L^{\mathcal{C}} \\ N_R \end{pmatrix} + h.c. \quad . \tag{1.3}$$

Such a combination is employed in the so-called see-saw mechanism [5, 6] within Grand Unification Theory (GUT). This mechanism offers the most popular explanation of why weakly interacting neutrinos, although massive, are nevertheless so light in comparison to quarks and charged leptons. In its framework neutrinos are Majorana particles, of which half are the familiar light neutrinos with masses of the order of 10^{-2} eV, while the other half are extremely heavy with masses possibly as large as the GUT scale ($10^{15} - 10^{16}$ GeV).

Experimentally the question of whether neutrinos are Dirac or Majorana particles has not been settled yet. The only path to confirm that neutrinos are indeed of Majorana type is the search for neutrinoless double β-decay ${}^{A}_{Z}X \rightarrow {}^{A}_{Z+2}X' + 2e^-$. Several experiments [7, 8, 9, 10, 11] are therefore after this process, which would not only lead to the discovery of the Majorana nature of neutrinos, but also to the measurement of the absolute neutrino mass scale. The Majorana/Dirac question is however not a crucial factor for most of neutrino physics, and in particular not for flavor mixing and neutrino oscillations.

1.2 Flavor Mixing

If neutrinos have masses, there will exist a set of mass eigenstates $|\nu_i\rangle$ $(i = 1, 2, 3)$. While these mass eigenstates describe the evolution of free neutrinos in time and space, interactions with matter are described by the flavor eigenstates $|\nu_\alpha\rangle$ $(\alpha = e, \mu, \tau)$, which couple to the weak gauge bosons. In general, the flavor eigenstates can be expressed by a coherent superposition of the mass eigenstates

$$|\nu_\alpha\rangle = \sum_i U^*_{\alpha i}|\nu_i\rangle \quad . \tag{1.4}$$

Here U denotes the unitary lepton mixing matrix, also referred to as PMNS[1] matrix. If one assumes neutrinos to be massless, this matrix were the identity matrix and the flavor eigenstates would equal the mass eigenstates. However, as already mentioned earlier, experiments demonstrate that neutrinos do change from one flavor to another, and thus have a mass and

[1]Named after Pontecorvo, Maki, Nakagawa and Sakata in recognition of their contributions to physics of mixing and oscillations [12, 13]

mix.

In the standard formalism of three neutrinos, U can be written as a product of three 3×3 matrices according to

$$U_{\alpha i} = \begin{pmatrix} 1 & 0 & 0 \\ 0 & c_{23} & s_{23} \\ 0 & -s_{23} & c_{23} \end{pmatrix} \begin{pmatrix} c_{13} & 0 & s_{13}e^{-i\delta} \\ 0 & 1 & 0 \\ -s_{13}e^{i\delta} & 0 & c_{13} \end{pmatrix} \begin{pmatrix} c_{12} & s_{12} & 0 \\ -s_{12} & c_{12} & 0 \\ 0 & 0 & 1 \end{pmatrix} \quad , \tag{1.5}$$

with $c_{ij} = \cos\theta_{ij}$ and $s_{ij} = \sin\theta_{ij}$. Here, θ_{ij} $(0 \leq \theta_{ij} \leq \pi/2)$ corresponds to the three mixing angles and δ $(0 \leq \delta \leq 2\pi)$ to the complex phase. Note, that the additional fourth complex phase matrix containing the Majorana phases is omitted here, since it does not enter in the oscillation parameters. The three presented mixing matrices describe mixing between specific mass eigenstates. The term $e^{i\delta}$ in the second matrix is referred to as the Dirac $\mathcal{CP}$ violation phase, which only contains a non-zero δ, if neutrino mixing violates $\mathcal{CP}$ symmetry.

As we will see later, there are some experiments in which only two neutrinos significantly participate in the mixing. For these cases it is sufficient to consider the two neutrino approximation with the following simplified mixing matrix which only depends on the single parameter θ

$$U = \begin{pmatrix} \cos\theta & \sin\theta \\ -\sin\theta & \cos\theta \end{pmatrix} \quad . \tag{1.6}$$

1.3 Neutrino Oscillations – Formalism

In vacuum, the propagation of the neutrino flavor eigenstates $|\nu_\alpha\rangle$ can be described by

$$|\nu_\alpha(t)\rangle = \sum_{i=1}^{3} e^{-iE_i t} U^*_{\alpha i} |\nu_i\rangle \quad , \tag{1.7}$$

signifying that a neutrino produced in a certain flavor eigenstate of energy E_i is at the time t after its production no longer described by a pure flavor state but rather by a superposition of all possible flavor states. The process where a neutrino produced at the origin in the flavor eigenstate $|\nu_\alpha\rangle$ evolves to a different flavor eigenstate $|\nu_\beta\rangle$ while propagating is referred to as

neutrino oscillation. The probability for neutrino oscillation in vacuum can be formulated by

$$\begin{aligned} P_{\nu_\alpha \to \nu_\beta} = |\langle \nu_\beta | \nu_\alpha(t) \rangle|^2 &= \delta_{\alpha\beta} \\ &- 4 \sum_{i>j} \Re \left(U^*_{\alpha i} U_{\beta i} U_{\alpha j} U^*_{\beta j} \right) \sin^2 \left(\frac{\Delta m^2_{ij} L}{4E} \right) \\ &+ 2 \sum_{i>j} \Im \left(U^*_{\alpha i} U_{\beta i} U_{\alpha j} U^*_{\beta j} \right) \sin \left(\frac{\Delta m^2_{ij} L}{2E} \right) \quad , \end{aligned} \tag{1.8}$$

where $\Delta m^2_{ij} \equiv m^2_i - m^2_j$ is the neutrino mass squared difference, $L \simeq t$ the oscillation distance and $E \simeq p \equiv p_j \simeq p_i$ the ultra-relativistic neutrino energy. It is convenient to include the previously omitted factors $\hbar$ and c and to use the following units

$$\frac{\Delta m^2_{ij} L}{4E} \simeq 1.27 \, \frac{\Delta m^2_{ij}(\mathrm{eV}^2) \; L(\mathrm{km})}{E(\mathrm{GeV})} \quad , \tag{1.9}$$

Formula 1.8 shows that if the mass eigenstates are different from each other, and if the flavor and mass eigenstates are not aligned, then neutrinos will oscillate between flavors as they propagate.

In the three-neutrino case, the transition probabilities depend on the parameter L/E, on two independent mass differences (Δm^2_{ij}) and on the elements of the neutrino mixing matrix, that can be parameterized in terms of three mixing angles ($\theta_{12}, \theta_{13}, \theta_{23}$) and one complex phase (δ) (see Section 1.2). The general expressions for the three-neutrino transition probabilities are rather cumbersome, but become less complicated if there is only one dominant mass scale. As it will be described in the following Section 1.4, solar and atmospheric neutrino measurements suggest a strong mass hierarchy $\left|\Delta m^2\right| \ll \left|\Delta M^2\right|$, with $\Delta m^2 \equiv m^2_2 - m^2_1 > 0$ and $\Delta M^2 \equiv m^2_3 - m^2_{1,2} \lesseqgtr 0$ [2]. This allows to describe the transition probabilities in neutrino experiments, for which only the largest mass squared difference ΔM^2 is relevant, by three parameters — one mass squared difference ΔM^2 and two mixing angles θ_{13} and θ_{23}

$$P_{\nu_\alpha \to \nu_\alpha} \simeq 1 - 4 \left|U_{\alpha 3}\right|^2 \left(1 - \left|U_{\alpha 3}\right|^2\right) \sin^2 \left(\frac{\Delta M^2 L}{4E} \right) \quad , \tag{1.10}$$

$$P_{\nu_\alpha \to \nu_\beta, \alpha \neq \beta} \simeq 4 \left|U_{\alpha 3}\right|^2 \left|U_{\beta 3}\right|^2 \sin^2 \left(\frac{\Delta M^2 L}{4E} \right) \quad , \tag{1.11}$$

with

$$|U_{e3}| = \sin^2 \theta_{13} \ , \quad |U_{\mu 3}| = \cos^2 \theta_{13} \sin^2 \theta_{23} \ , \quad |U_{\tau 3}| = \cos^2 \theta_{13} \sin^2 \theta_{23} \quad .$$

These expressions are often used to describe data of reactor, accelerator and atmospheric experiments, which are mainly sensitive to ΔM^2, i.e. for which $\Delta M^2 L/4E \sim \mathcal{O}(1)$. For

[2] Depending on the references, ΔM^2 is defined as $\Delta M^2 \equiv \Delta m^2_{31}$, $\Delta M^2 \equiv \Delta m^2_{32}$ or $\Delta M^2 \equiv {}^1\!/_2 \left(\Delta m^2_{31} + \Delta m^2_{32}\right)$, which is possible because $\left|\Delta m^2\right| \ll \left|\Delta M^2\right|$.

example, in a long-baseline accelerator experiment, like T2K, the three-neutrino transition probability $P_{\nu_\mu \to \nu_e}$ and the disappearance probability $P_{\nu_\mu \to \nu_x}$ can be approximated by

$$P_{\nu_\mu \to \nu_e} \simeq \sin^2 2\theta_{13} \sin^2 \theta_{23} \sin^2 \left(\frac{\Delta M^2 L}{4E} \right) \quad , \tag{1.12}$$

$$P_{\nu_\mu \to \nu_x} \simeq 1 - \cos^4 \theta_{13} \sin^2 2\theta_{23} \sin^2 \left(\frac{\Delta M^2 L}{4E} \right) \quad . \tag{1.13}$$

Here, ν_x is a superposition of ν_μ and ν_τ.

If only two neutrinos are relevant in the considered process, then Equation 1.8 reduces to

$$P_{\nu_\alpha \to \nu_\beta, \alpha \neq \beta} \simeq \sin^2 2\theta \sin^2 \left(\frac{\Delta m^2_{ij} L}{4E} \right) \quad , \tag{1.14}$$

with the single mass-squared difference Δm^2_{ij}. The two-neutrino approximation offers a fairly accurate description of several transitions, which include the atmospheric mixing $\nu_\mu \leftrightarrow \nu_\tau$, where the electron neutrino is negligible. Also for the solar case $\nu_e \leftrightarrow \nu_x$ this framework is appropriate. The two neutrino approximation is feasible for these processes due to the fact that the mixing angle θ_{13} is very small and also because the mass squared splitting $\left|\Delta M^2\right|$ is much larger than the other one $\left|\Delta m^2\right|$. Experimental evidence suggesting these facts are discussed in the following Section.

Up to now, the presented formalism has been established for neutrino oscillation in vacuum only. However, as neutrinos travel through matter, e.g. the sun or the earth, the ν_e can coherently forward-scatter off electrons they encounter along their way [14]. This causes electron neutrinos to gain an additional interaction potential energy, which gives rise to an effective mixing and mass matrix. As a result, the probability for changing from one flavor to another can be rather different than the one in vacuum [15]. This phenomenon is known as Mikheyev-Smirnov-Wolfenstein (MSW) effect. As verified by experiments (see Section 1.4) the matter effect becomes relevant for high energetic solar neutrinos passing through the large electron densities of the sun. The probability for a ν_e from the sun to be detected as an electron neutrino then becomes $P_{\nu_e \to \nu_e} = \sin^2 \theta_{12}$, which significantly differs from the one expected in vacuum $P_{\nu_e \to \nu_e} = 1 - (\sin^2 2\theta_{12})/2$. For low energy solar neutrinos, atmospheric neutrinos and typical baselines of reactor and accelerator neutrinos, however, the matter effect is to a large extent negligible.

1.4 Neutrino Oscillations – Experiments

Neutrino oscillation experiments attempt to measure changes in the flavor composition of neutrino sources over certain distances in order to extract the mass squared differences as

well as the mixing parameters (see Eq. 1.5). If oscillations occur, the signature is a flavor composition that displays periodic variations with L/E. The amplitude of the oscillations yields the mixing angles, whilst the period of the oscillation specifies the mass splittings. The optimal sensitivity to a particular mass splitting is achieved when the characteristic L/E value for the neutrino flux at the detector satisfies $\Delta m^2 L/E \simeq \mathcal{O}(1)$. With significantly smaller L/E values the transition probabilities are too small for oscillations to be detected, while with much larger L/E values, the transition probabilities vary rapidly with either L or E, therefore the transition probability simply averages to $^1/_2 \sin^2 2\theta$ and all information about the mass splitting is lost.

Effects of neutrino oscillations were first observed in the late 1960s, when R. Davis and J. Bahcall detected a deficit, compared to Standard Solar Model (SSM) predictions, in the solar neutrino flux with the Homestake mine detector. Since then, a series of experiments have been developed to address the question of neutrino oscillations. In the following sections the most important experimental results to date and constraints on the mixing parameters are discussed. They are grouped according to the different sectors of the mass-mixing parameter space.

Sector 12

Sector 12 is also referred to as solar sector since experiments probing solar neutrinos significantly contributed to the current results on θ_{12} and Δm^2. Solar neutrinos have so far been measured by chlorine (Homestake [16]) and gallium (SAGE [17], GALLEX [18] and GNO [19]) radiochemical detectors and water Cherenkov detectors using light water (Kamiokande [20] and Super-Kamiokande (SK) [21, 22]) and heavy water (SNO [23]). Low energy solar neutrinos were furthermore observed by a liquid scintillator detector (Borexino [24]). Next to the solar neutrino experiments also the long-baseline reactor experiment KamLAND [25] has eminently contributed in probing this sector.

Solar neutrinos are produced via nuclear fusion reactions in the sun. The vast majority originate from the dominant three processes $p+p \rightarrow d+e^+ +\nu_e$ (abbr.: pp), $e^- + {}^7Be \rightarrow {}^7Li + \nu_e$ (abbr.: ^7B) and ${}^8B \rightarrow {}^8Be^* + e^+ + \nu_e$ (abbr.: ^8B), that form part of the proton-proton chain. In the various steps of this chain, electron neutrinos of different energies are produced. The resulting neutrino energy spectrum from all nuclear fusion processes as predicted by the Solar Standard Model (SSM), is shown in Figure 1.1, together with the domains to which different experiments are sensitive to. For years, solar neutrino experiments observed significantly lower ν_e fluxes as expected from neutrino production calculations. This discrepancy was to be termed solar neutrino problem. It can be explained by the phenomenon of neutrino oscillations when taking matter effects into account. A direct proof that solar neutrinos undergo flavor change modified by solar matter came only recently with the Sudbury Neutrino Observatory (SNO).

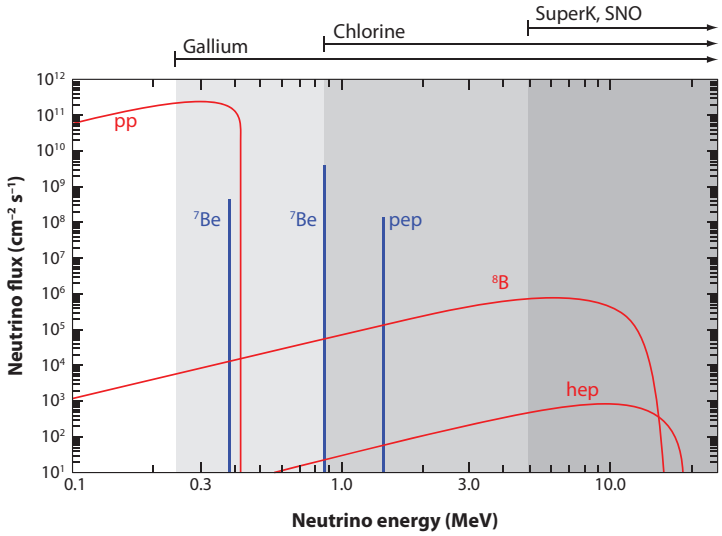

Figure 1.1: The solar neutrino energy spectrum, as predicted from the SSM, as well as the energy domains different experiments are sensitive to. The figure is taken from: [26].

Using heavy water as target, SNO is capable of measuring both the electron neutrinos through charged current[3] ($\nu_e + d \rightarrow p + p + e^-$) interactions and all active neutrino flavors through neutral current[3] ($\nu_\alpha + d \rightarrow n + p + \nu_\alpha$) as well as elastic scattering[4] ($\nu_\alpha + e^- \rightarrow \nu_\alpha + e^-$) interactions. Figure 1.2 shows results from SNO phase II[5] for the combined flux $\nu_{\mu\tau}$ versus the one of ν_e. SNO clearly observes a non-vanishing $\nu_{\mu\tau}$ flux, which evidences that some of the ν_e produced in the solar core do indeed change flavor. It also shows that the total neutrino flux measured by NC interactions is in excellent agreement with the SSM predictions. The flux results can be used to determine the averaged survival probability $\langle P \rangle = \Phi_{CC}/\Phi_{NC}$, which then allows for a precise determination of θ_{12}.

Another way to probe mixing in the Sector 12 is to study the survival of electron antineutrinos produced in nuclear power reactors under the assumption of $\mathcal{CPT}$ invariance. The Kamioka Liquid Scintillator Anti-Neutrino Detector (KamLAND) is the only reactor experiment sensitive to Δm^2. As nearly all reactor neutrino experiments, KamLAND utilizes the $\overline{\nu_e} + p \rightarrow n + e^+$ inverse β-decay reaction to detect $\overline{\nu_e}$. The antineutrinos are emitted from nuclear fission processes of 53 surrounding reactors with a flux-weighted average distance of L_0 =180 km. The KamLAND detector consists of about a kiloton of liquid scintillator allowing for low energy detection thresholds of a few MeV. It examines neutrino oscillations in the absence of the MSW effect – matter effects in the Earth's crust are negligible for the considered

[3]Charged Current (CC) interactions are mediated by a charged $W^\pm$ boson, while Neutral Current (NC) interactions are mediated by a Z boson

[4]Elastic scattering is sensitive to all neutrino flavors, however with reduced sensitivity to ν_μ and ν_τ

[5]In SNO phase II, NaCl was dissolved in the heavy water to enhance the sensitivity to the NC signals through higher large neutron capture efficiency

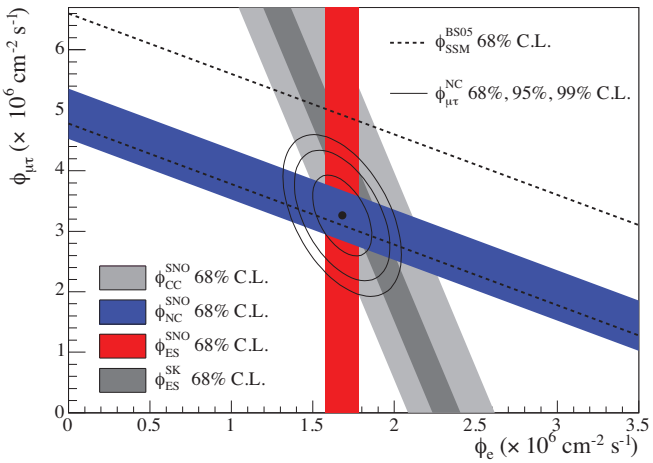

Figure 1.2: Combined flux of ν_μ and ν_τ versus ν_e. CC, NC and ES flux measurements are indicated by the filled bands. The total ^{8}B solar neutrino flux predicted by the SSM is shown as dashed lines, and that measured with the NC channel is shown as the solid band parallel to the model prediction. The narrow band parallel to the SNO ES result corresponds to the Super-Kamiokande result in [28]. The intercepts of these bands with the axes represent the $\pm 1\sigma$ uncertainties. The non-zero value of $\nu_{\mu\tau}$ provides strong evidence for neutrino flavor transformation. The point represents ν_e from the CC flux and $\nu_{\mu\tau}$ from the NC-CC difference with 68%, 95%, and 99% C.L. contours included. The figure is taken from: [29].

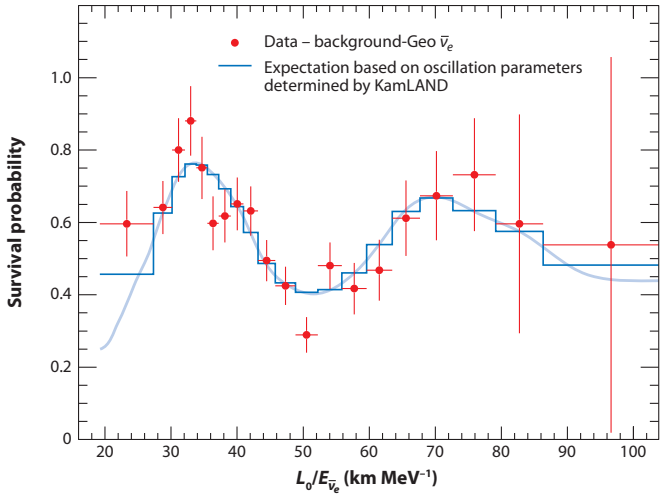

Figure 1.3: Ratio of background and geo-neutrino subtracted $\overline{\nu_e}$ spectrum as a function of L_0/E ($L_0 = 180$ km). The oscillatory pattern is statistically significant and in excellent agreement with neutrino oscillation predictions (blue line). The figure is taken from: [25].

baselines – down to the Δm^2 region of $\sim 10^{-5}$ eV^2. In 2002, KamLAND reported the first evidence for $\overline{\nu_e}$ disappearance [30]. Figure 1.3 shows more recent results on the $\overline{\nu_e}$ survival probability as a function of L_0/E. It displays a clear and statistically significant oscillatory pattern, which is in excellent agreement with the neutrino oscillation hypothesis in vacuum. KamLAND furthermore dominates the determination of the mass squared splitting Δm^2.

The comparison of the KamLAND oscillation parameter analysis with the global solar neutrino results obtained under the assumption of solar MSW oscillations is demonstrated in Figure 1.4 for the two- and three-flavor oscillation analysis. One can clearly observe the complementarity of the solar neutrino data, which tightly constrain θ_{12}, and the KamLAND measurements, which strongly constrain Δm^2. For the two and three neutrino mixing scheme the combination of the KamLAND and solar neutrino results lead to the world average values [23], respectively

$$2\nu: \qquad \Delta m^2 = \left(7.59^{+0.20}_{-0.21}\right) \times 10^{-5}\text{eV}^2 \,, \qquad \tan^2\theta_{12} = 0.457^{+0.040}_{-0.029} \quad , \tag{1.15}$$

$$3\nu: \qquad \Delta m^2 = \left(7.59^{+0.23}_{-0.18}\right) \times 10^{-5}\text{eV}^2 \,, \qquad \tan^2\theta_{12} = 0.468^{+0.042}_{-0.033} \quad . \tag{1.16}$$

Sector 23

Sector 23 is also known as atmospheric sector due to the fact that experiments studying atmospheric neutrinos considerably contributed to the current results on θ_{23} and ΔM^2. Atmospheric

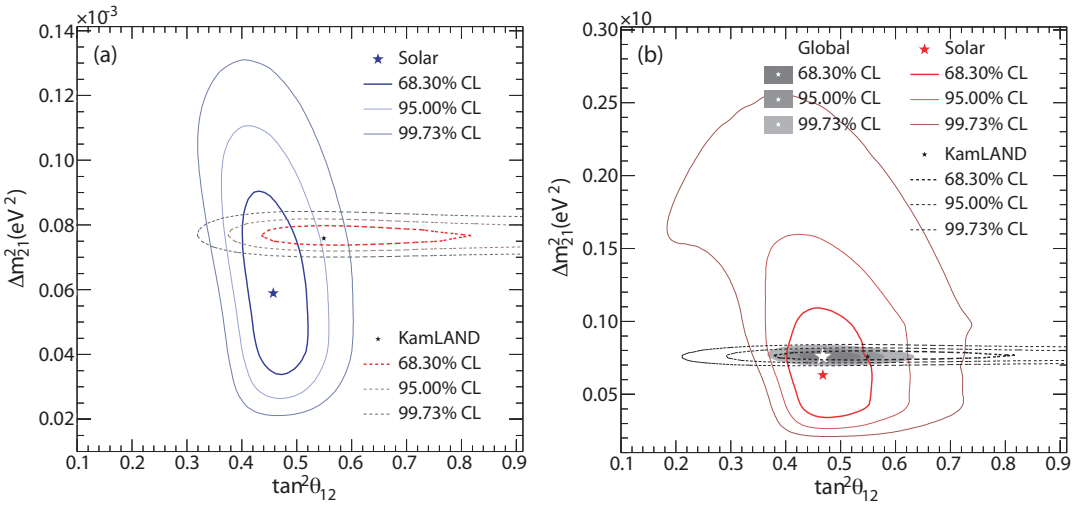

Figure 1.4: Solar and KamLAND oscillation parameter analysis for (a) a two-flavor oscillation hypothesis and (b) a three-flavor hypothesis. The solar data include SNO, Homestake, SAGE, Gallex, GNO, Borexino and SK data. The figure is taken from: [23].

neutrinos have so far been measured by the water Cherenkov detectors Kamiokande ([20]), IMB ([31]) and Super-Kamiokande ([32]) and by the ionisation/scintillation-based tracking detectors Fréjus ([33]), NUSEX ([34]), MACRO ([35]) and Soudan-2 ([36]). The long-baseline accelerator experiments K2K ([37]), MINOS ([38]) and OPERA ([39]) have also been probing this sector using man made neutrinos. While K2K employs the light-water Cherenkov detector Super-Kamiokande, MINOS uses a steel/scintillator detector and OPERA an emulsion-based hybrid detector.

Atmospheric neutrinos are produced in cascades initiated by collisions of cosmic rays with the Earth's atmosphere. In the primary collision mainly pions and some kaons are produced, decaying into muon and electron neutrinos and anti-neutrinos. Despite large uncertainties in the absolute fluxes of atmospheric neutrinos, the flavor ratio $R = (\nu_\mu + \overline{\nu_\mu})/(\nu_e + \overline{\nu_e}) \simeq 2$ is estimated to be known at the 5% level [40]. Due to the isotropy of cosmic rays and the spherical symmetry of the atmosphere, one furthermore expects atmospheric neutrino fluxes to be up-down symmetric with respect to the zenith angle. A distortion of this fundamental expectation would thus directly evidence atmospheric neutrino oscillations. To investigate this, atmospheric neutrinos are measured in deep underground detectors.

The first compelling evidence for atmospheric neutrino oscillation was presented by Super-Kamiokande (SK) in 1998 [32]. Super-Kamiokande is a 50-kiloton ring-imaging water Cherenkov detector in which μ- and e-like charged current interactions can be distinguished through their specific light patterns. The much larger detector volume with respect to its precursors allows to measure an increased percentage of fully contained μ- and e-events, where the entire energy

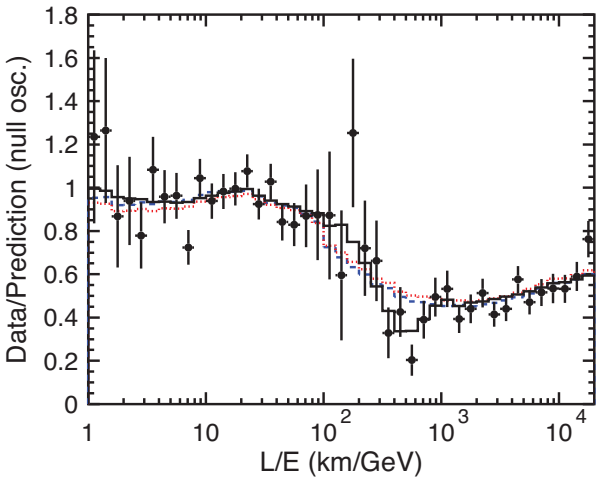

Figure 1.5: Ratio of the data to the MC events without neutrino oscillations (points) as a function of the reconstructed L/E together with the best-fit expectation for 2-flavor $\nu_\mu \rightarrow \nu_\tau$ oscillations (solid line). Also shown are the best-fit expectation for neutrino decay (dashed line) and neutrino decoherence (dotted line). The figure is taken from: [41].

from the interaction is deposited in the active detector volume, thus allowing to reconstruct the ν direction. SK measured the zenith angle distribution of the μ- and e-like events and found that the number upward traveling muon neutrinos, which are traveling the longest distance, and the resulting flavor ratio R were significantly lower than what was expected from predictions in the absence of neutrino oscillations. The observed up-down angular asymmetry of atmospheric ν_μ but not ν_e was later confirmed by MACRO [35] and Soudan-2 [36] and could be well described with the hypothesis of dominant two-flavor $\nu_\mu \rightarrow \nu_\tau$ oscillations. In 2004, Super-Kamiokande published [41] the muon disappearance probability as a function of neutrino flight length L over neutrino energy E as shown in Figure 1.5. The observed shape of the data is consistent with the sinusoidal flavor transition probability of neutrino oscillation, which strongly constrains the mixing parameters θ_{23} and ΔM^2. Alternating models of neutrino decay [42] and neutrino decoherence [43] are disfavored as they do not successfully reproduce the shape in the L/E distribution.

To investigate ν_μ disappearance in a controlled experimental setting, accelerator-based neutrino oscillation experiments were designed. KEK[6] to Kamioka (K2K) and Main Injector Neutrino Oscillation Search (MINOS) are both neutrino oscillation experiments using beams of accelerator-produced muon neutrinos from in-flight pion decay. Each includes a near detector designed to study the unoscillated beam spectrum and composition as well as a far detector. The distance of the far detector L ($L_{\mathrm{K2K}} = 250$ km, $L_{\mathrm{MINOS}} = 735$ km) and the average beam energy $\langle E \rangle$ ($\langle E_{\mathrm{K2K}} \rangle \sim 1.4$ GeV, $\langle E_{\mathrm{MINOS}} \rangle \sim 4$ GeV) are chosen such that $L/\langle E \rangle$ corresponds to

[6] High Energy Research Organization, Tsukuba, Japan

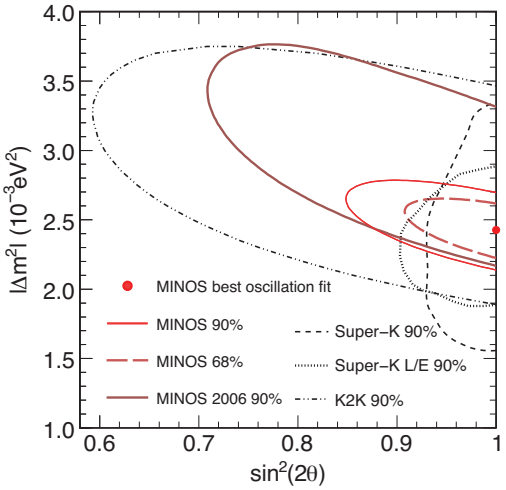

Figure 1.6: Contours of the two-flavor oscillation fit to the data from MINOS [38, 44], Super-Kamiokande [41, 45] and K2K [37]. The figure is taken from: [44].

the first oscillation maximum of atmospheric neutrinos. K2K was first to observe a distortion and suppression of the energy spectrum of accelerator-produced ν_μ. The results were consistent with a neutrino oscillation interpretation, with parameters θ_{23} and ΔM^2 compatible with those of atmospheric neutrino data [37]. Shortly after, these observations were further confirmed by MINOS, whose latest results [44] provide the most precise measurements in the atmospheric sector (see Figure 1.6). The two-flavor oscillation fit yields the following mixing parameters

$$2\nu: \qquad \Delta M^2 = (2.43 \pm 0.13) \times 10^{-3}\text{eV}^2 \,, \qquad \sin^2 2\theta_{23} > 0.90 \quad (90\%\ \text{C.L.}) \quad . \tag{1.17}$$

Currently also the Oscillation Project with Emulsion-Tracking Apparatus (OPERA) is probing the atmospheric sector by searching for the ν_τ flavor appearance in a ν_μ beam. The beam is produced using the Super Proton Synchrotron (SPS) at the European Organization for Nuclear Research (CERN). Its average energy amounts to 17 GeV, which corresponds to the maximum ν_τ charged current production rate for the given oscillation probability and the production cross section. The OPERA detector is located 732 km away from the source. It is based on photographic emulsion technology, already successfully used to observe the first ν_τCC interactions in the DONUT experiment [46]. After two years data taking OPERA identified the first candidate ν_τ CC event in an event sample corresponding to 1.89×10^{19} protons on target (p.o.t.) in which 0.54 ± 0.13 ν_τ events are expected [39]. The significance of having identified a ν_τ event and not some background fluctuation is 2.36 σ for the decay channel

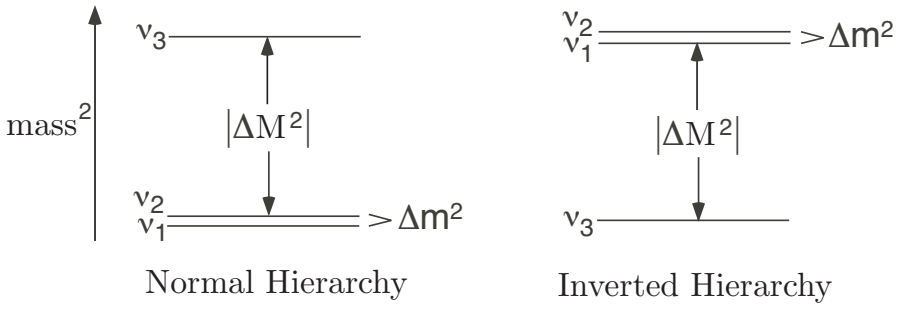

Figure 1.7: Normal and inverted neutrino mass hierarchies.

$h^-(\pi_0)\nu_\tau$. This is not yet a claim of observation of $\nu_\mu \rightarrow \nu_\tau$ oscillation. The search for more candidate events continues in the pursuit to firmly establish direct ν_τ appearance.

Sector 13

Sector 13 is home to the remaining and yet unmeasured mixing parameters: the mixing angle θ_{13} and the phase δ, which if different from zero would introduce $\mathcal{CP}$ violation amongst the leptons. From the solar and atmospheric sectors it is known that the mass spectrum is composed of two close mass states $\nu_{1,2}$ and another mass state ν_3, which is more separated in mass ($\Delta m^2 \ll \Delta M^2$). However, it is not yet understood whether ν_3 is heavier than $\nu_{1,2}$, that is to say of so-called normal mass hierarchy ($m_3 \gg m_2 > m_1$), or whether it is lighter than $\nu_{1,2}$, i.e. of inverted mass hierarchy ($m_2 \gg m_1 > m_3$). Figure 1.7 illustrates the two possible scenarios, which are addressed in the context of this sector. Only for $\theta_{13} \neq 0$ one can access the neutrino mass hierarchy via matter effects as well as δ via $\mathcal{CP}$-odd observables. Mainly sensitive to θ_{13} are short-baseline reactor experiments, while the previously introduced experiments of sectors 12 and 23 are to a minor degree sensitive to it. Short-baseline reactor experiments, which look for suppression of $\overline{\nu_e}$, include the liquid scintillator anti-neutrino experiments CHOOZ [47] and Palo Verde [48].

Nowadays, the most stringent limits to θ_{13} come from the CHOOZ reactor experiment, which has searched for the suppression of the $\overline{\nu_e}$ flux originating from nuclear reactors. With a baseline of 1 km and an anti-neutrino energy of a few MeV, CHOOZ is sensitive to the large mass squared splitting ΔM^2 as of atmospheric experiments. Like KamLAND, the experiment is based on the liquid scintillator technique to detect the $\overline{\nu_e}$'s via their inverse β-decay reaction. CHOOZ found a ratio of measured versus expected event rates of $R = 1.01 \pm 2.8\%\ (stat) \pm 2.7\%\ (syst)$ [47]. With a 90% confidence level this result presents an absence of neutrino oscillations in the $\overline{\nu_e}$ disappearance mode, which was furthermore substantiated by the measurements of Palo Verde [48]. It leads to the conclusion that the $\nu_\mu \rightarrow \nu_e$ transition is not a significant contribution to atmospheric ν_μ disappearance, thus leaving the $\nu_\mu \rightarrow \nu_\tau$ pos-

sibility. The CHOOZ null oscillation result can be combined with the determination of ΔM^2 from atmospheric and long-baseline experiments (atm. neutrino data + K2K + MINOS) and then leads to the currently best upper bound of $\sin^2\theta_{13} < 0.031$ (0.047) at 90% C.L. (3σ) [49]. So far, there are no constraints of any significance on δ nor is the mass hierarchy known.

Summary and Future Perspectives

Solar and long-baseline reactor experiments have dominantly been probing Sector 12 with Δm^2 and θ_{12}, whereas atmospheric and long-baseline accelerator experiments mainly explored Sector 23 with ΔM^2 and θ_{23}. Short-baseline reactor experiments give, in combination with other data, most stringent limits to θ_{13} of Sector 13. Various global three-neutrino analyses of the available neutrino oscillation data have been performed featuring a high degree of consistency in the parameter determination. According to [49] the resulting mixing parameters are given by

$$\begin{aligned} \sin^2\theta_{12} &= 0.318^{+0.019}_{-0.016}\ , \qquad \Delta m^2 = \left(7.59^{+0.23}_{-0.18}\right)\times 10^{-5}\mathrm{eV}^2 \quad , \\ \sin^2\theta_{23} &= 0.50^{+0.07}_{-0.06}\ , \qquad \Delta M^2 = \left(2.40^{+0.12}_{-0.11}\right)\times 10^{-3}\mathrm{eV}^2 \quad , \\ \sin^2\theta_{13} &\leq 0.031 \quad (0.047) \quad \text{at } 90\%\ \text{C.L.} \quad (3\sigma) \quad . \end{aligned} \tag{1.18}$$

Despite the multitude of experimental achievements and consequential knowledge in the field of neutrino mixings, still missing tiles in the oscillation mosaic remain to be placed. Just to stress the ones addressed by the accelerator experiment T2K experiment [3], it has not yet been possible to determine nor to exclude a non-zero value of θ_{13}, which is crucial for the determination of the still indeterminate leptonic $\mathcal{CP}$ violation phase as well as the mass hierarchy of neutrinos. That great importance is placed upon the T2K measurements becomes manifest in the large amount of oscillation experiments designed to investigate the question of θ_{13}. Besides T2K, the long-baseline accelerator experiment NOνA [50] as well as the reactor experiments Daya Bay [51], Double CHOOZ [52] and RENO [53], belong to the upcoming generation of experiments searching for θ_{13}. This multitude of experiments is very important as their combination can help to eliminate a problem known as parameter degeneracy [54]. The latter implies that measurements of $P_{\nu_\mu\to\nu_e}$ on their own cannot uniquely determine the value of θ_{13}, as multiple solutions of the three-neutrino parameter space $(\theta_{13}, \delta, \theta_{23}, \pm\Delta M^2)$ exist. Determining a single solution requires a combination of several measurements in different oscillation channels, energy ranges and baselines.

If upcoming experiments succeed to measure a non-zero value of θ_{13} or even provide a first attempt to establish the mass hierarchy and $\mathcal{CP}$ violation, the long-term prospects in neutrino physics could feature superbeams, β-beams or neutrino factories sensitive enough to make a firm discovery of $\mathcal{CP}$ violation in the leptonic sector and the neutrino mass hierarchy.

Such superbeams would push conventional neutrino beams to their ultimate performances. In combination with huge detectors, of at least one order of magnitude bigger than the present ones, these superbeams would be a possible way to attack the remaining questions. As an example, T2K could be upgraded, as already delineated in the initial letter of intent [3], by increasing the power of the J-PARC accelerator from 0.75 MW to 4 MW and building a megaton water Cherenkov detector, Hyper-Kamiokande, to be placed at the same distance and off-axis angle as the current T2K far detector, Super-Kamiokande (see Chapter 2). Continuative development of this project contemplate placing a second detector at a longer distance of about 900 km in Korea, T2KK [55], or substituting it with a 100 kiloton liquid argon detector placed at the ∼658 km far-away Okinoshima islands [56]. Next to the superbeams, also β-beams [57] and neutrino factories [58] are under discussion, which would use, respectively, fully selected, collimated β-unstable ions and muons as neutrino parents. In this way very pure, intense and precisely known neutrino beams could be designed, which would overcome the limitations resulting from intrinsic ν_e contamination in conventional neutrino beams. A more detailed overview of latest investigations on super-beams, β-beams and neutrino factories can be found in [59].

1.5 Conventional Neutrino Beams

As the current generation neutrino oscillation experiments enter a new domain of precision, limiting systematic uncertainties on the neutrino beam of accelerator experiments, like T2K, become essential. As already illustrated in Section 1.4, with the help of K2K, MINOS and Opera, accelerator experiments probe neutrino oscillations with man-made muon neutrino beams, by searching for the disappearance of the muon neutrino beam, or the appearance of a neutrino flavor other than the original muon flavor.

To produce conventional muon neutrino beams, accelerators are employed, which generate high-energy protons and direct them towards nuclear targets. When the protons impinge upon the target, secondary hadrons are produced, whose decay in turn yield a neutrino beam. The decays of pions and kaons, with their decay modes as given in Table 1.1, carry the most profitable yield to muon neutrino beams. Subsequent muon decays give rise to muon (anti-) neutrinos as well as electron (anti-) neutrinos, which are more of an undesirable background than a desired source for such beams.

The precise manipulation of the secondaries from the production target permits to control the type (ν_μ or $\overline{\nu}_\mu$) and the energy spectrum of the neutrino beam. Magnetic horns are generally used to focus secondaries of positive (negative) sign and defocus the ones of opposite sign, thus enhancing the ν_μ ($\overline{\nu}_\mu$) flux while reducing the $\overline{\nu}_\mu$ (ν_μ) background. Since the energy of neutrinos emitted along the axis of travel of the secondaries is linearly related to the secondaries

Neutrino Parent	Decay Channel	Branching Ratio [%]
$\pi^{\pm}$	$\rightarrow \mu^{\pm}\nu_{\mu}(\overline{\nu}_{\mu})$	99.9877
	$e^{\pm}\nu_{e}(\overline{\nu}_{e})$	0.0123
$K^{\pm}$	$\rightarrow \mu^{\pm}\nu_{\mu}(\overline{\nu}_{\mu})$	63.55
	$\rightarrow \pi^{0}e^{\pm}\nu_{e}(\overline{\nu}_{e})$	5.07
	$\rightarrow \pi^{0}\mu^{\pm}\nu_{\mu}(\overline{\nu}_{\mu})$	3.35
K^{0}_{L}	$\rightarrow \pi^{\pm}e^{\mp}\nu_{e}(\overline{\nu}_{e})$	40.55
	$\rightarrow \pi^{\pm}\mu^{\mp}\nu_{\mu}(\overline{\nu}_{\mu})$	27.04
$\mu^{\pm}$	$\rightarrow e^{\pm}\nu_{e}(\overline{\nu}_{e})\overline{\nu}_{\mu}(\nu_{\mu})$	100

Table 1.1: Neutrino parents with their decay channels and branching ratios. Values from [4] are quoted.

energy, a given neutrino energy of an on-axis beam can be achieved by focusing secondaries of a particular beam momentum. For off-axis decays, the relationship between the neutrino and the parent energy is weaker, so that for large off-axis angles a broad-band secondary beam can generate a narrow-band neutrino spectrum. The idea of such an off-axis scheme was first proposed in [60] and has since been adopted by MiniBooNE [61] at Fermilab and by T2K at JPARC (see Chapter 2).

Decay volumes are used behind the focusing systems to permit the secondaries to decay in flight. Often, these decay volumes are evacuated or filled with helium gas to reduce absorption and multiple Coulomb scattering. Such decay volumes must balance the needs of a long enough decay tube, allowing for as many secondaries to decay as possible, against the level of ν_e contamination in the beam, of which much arises from subsequent muon decays. To reduce neutrino production from subsequent muon decays, a beam dump is finally employed right behind the decay volumes, which defines the maximum flight time of the secondaries and tertiaries.

There are different sources of uncertainties for conventional neutrino beams. These include uncertainties on the primary proton beam such as its angle, divergence, spot size, halo and number of protons on target. To diminish these uncertainties, instrumentation is placed in the primary beam line just upstream of the target. Further systematic uncertainties on the neutrino flux come from focusing uncertainties, like absolute current deviations in the horns and misalignment of the focusing system. Monitoring the tertiary muon beam allows to lower these uncertainties. Uncertainties also come from the secondary beam production, as the produced secondaries leave the target boosted in the forward direction, but with some divergence depending on the production cross sections. Detectors placed directly in the sec-

ondary beam are rather unusual, as they must cope with high rates and can substantially affect the neutrino beam. More sophisticated is to make use of hadron production data, as discussed in the following Section 1.6, however such data may not exist for a given neutrino experiment's target material, thickness, beam energy, or relevant phase space region. In such circumstances, models of secondary production, derived by fitting and interpolating available experimental data, can be utilized; the shower cascade models, MARS [62] and FLUKA [63], and the parametric models, BMPT [64] and Sanford-Wang [65, 66], have, for example, each been employed in neutrino flux calculations. A more detailed overview of hadron production models and parameterizations can be found in [67].

1.6 Hadron Production Experiments

Current accelerator neutrino experiments are challenged to lower their systematic uncertainties in order to allow for high precision neutrino oscillation measurements. One of the main uncertainties on the neutrino beam is due to the poor knowledge of hadron production cross sections, which define the secondary hadron beam. As mentioned before, it is most suitable to diminish these uncertainties by using high precision hadron production measurements. As discussed in [70], such measurements are also valuable for optimizing the design of future projects like the neutrino factory.

Over the past, several hadron production experiments have been conducted over a range of incident proton beam momenta from 10 GeV/c to 450 GeV/c, using different target materials, mostly beryllium, aluminum, copper and lead. In spite of the multitude of experiments, only a few of them offer high precision measurements, which cover a large region of phase space [67].

Hadron production experiments can be grouped into single-arm spectrometers, such as the NA56/SPY [68] experiment at the CERN SPS, and full acceptance spectrometers, like the NA49 [69] experiment at the CERN SPS. Single-arm spectrometers direct the produced secondary particles within a small angular acceptance into a magnetic channel, in which dipoles define a finite momentum region and quadrupoles focus the secondaries within the given momentum region into the analyzing channel, usually equipped with Time OF Flight (TOF) and/or Cherenkov detectors for particle identification. Such experiments often lack in high precision on the normalization due to the difficulty of proton counting. Normalization uncertainties typically range from about 10% to 25% [67]. Measurements of higher precision are offered by the more recent full acceptance spectrometers, which employ large acceptance tracking devices, such as Time Projection Chambers (TPCs), commonly combined with TOF and Cherenkov counters for complementing the particle identification capability of the TPCs.

Some of the latest large acceptance hadron production experiments have been purposely constructed for a better simulation of neutrino experiments, overcoming the lack of suitable

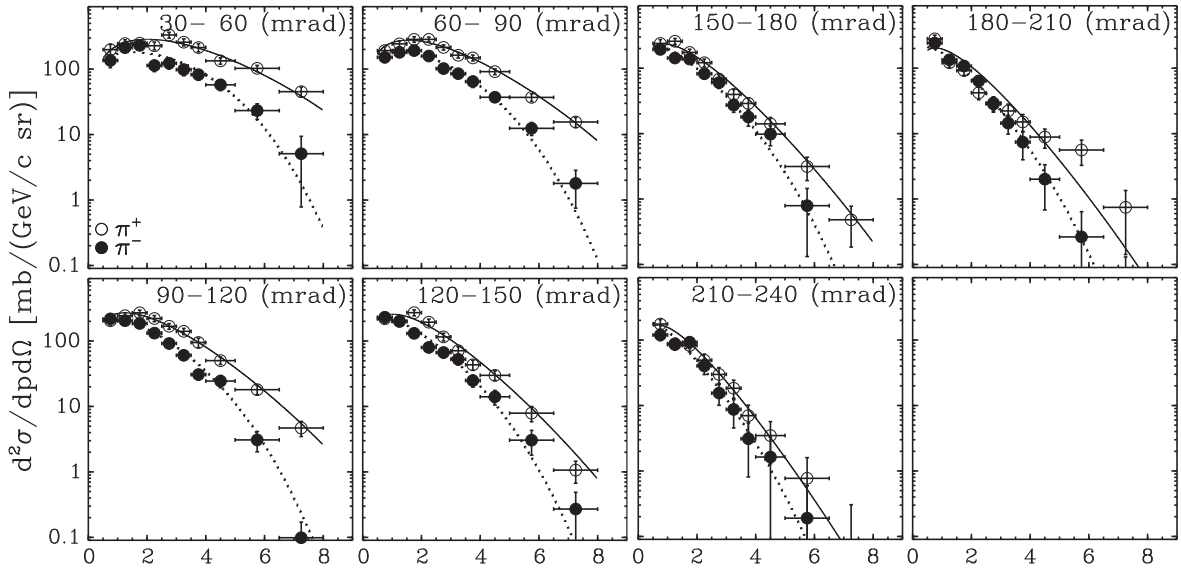

Figure 1.8: Double-differential production cross-section of positive (open circles) and negative (filled circles) pions from p–C collisions at 12 GeV/c as a function of momentum (p) in different polar angle (θ) intervals as measured by HARP. The error bars shown include statistical errors and all systematic errors (diagonal). The curves show the respective Sanford-Wang parameterization. The figure is taken from: [75].

hadron production data. HARP [70, 71] at the CERN PS was the first hadron production experiment purposely constructed for the prediction of atmospheric neutrino fluxes, characterization of accelerator neutrino beams, and quantification of pion production and capture for neutrino factory designs. HARP performed extensive measurements of hadron production cross sections and secondary particle yields, using different nuclear targets and beams of protons and pions in the energy range from 3 to 15 GeV. The results were, for example, used to calculate the properties of conventional neutrino beams, like those of K2K [37] and MiniBooNE [61]. The neutrino flux calculation for the final disappearance analysis of K2K [77] is based on the Sanford-Wang parameterization of the HARP measurements of positively charged pion production in proton-aluminum collisions at 12.9 GeV/c [72], and results presented by MiniBooNE [76] are based on the Sanford-Wang parameterization of the HARP [73] and E910 [74] cross sections for pions in proton–beryllium collisions at different beam momenta. HARP has also measured the pion production cross-sections of charged pions in proton–carbon interactions at 12 GeV/c (see Figure 1.8). These measurements were for the time being the most suitable ones for the T2K experiment, which requires proton-carbon hadron production measurements at 31 GeV/c.

Next to HARP, the MIPP E907 experiment [78] at Fermilab has been designed to study particle production in the energy range from 5 up to 120 GeV on several targets, including

beryllium and carbon, for the use of accelerator and atmospheric neutrino experiments, such as NOνA [50] and Super-Kamiokande/Hyper-Kamiokande [21, 22, 3]. To deliver adequate hadron production measurements for the forthcoming accelerator experiment NOνA, MIPP E907 has collected hadron production data on a spare NuMI target, proposed to use in NOνA, as well as on a thin carbon target using 120 GeV/c protons. Preliminary results on various particle production ratios for different carbon targets were published in [80].

Following the steps of HARP and MIPP E907, the NA61 [81, 82, 83, 84] experiment pursues a program of hadro-production measurements for the cosmic air shower experiments, Pierre Auger [98] and KASCADE [99], and the neutrino experiment T2K. The NA61 program and status connected to T2K will be covered in the following chapters.

Chapter 2

T2K and its Requirements on NA61

T2K (Tokai to Kamioka) is a second generation long baseline experiment [3] designed to observe the phenomenon of neutrino flavor change so as to further explore the mixing parameter space in the lepton sector. In particular, the third and final unmeasured mixing angle θ_{13} is of major interest. It will be investigated by studying the ν_e appearance in a ν_μ beam. Alongside this, T2K will also examine the ν_μ disappearance with the aim of improving the current precision on θ_{23} and ΔM^2. To achieve new measurement accuracies, a high luminosity narrow band neutrino beam tuned to the oscillation maximum is put to use at JPARC, Japan. It is realized by a high intensity 30 GeV proton beam impinging on a 90 cm long carbon target, whereby mesons (π, K, etc) are produced which decay into neutrinos ($\nu_{\mu,e}$). The neutrino flux is then measured 2.5° off-axis, both in a near detector, located 280 m behind the target (ND280) [85], and the 295 km far away Super-Kamiokande detector (SK) [32]. Neutrino oscillations are probed by comparing the neutrino flux measured at SK to the one predicted at SK. In order to predict the flux at SK one uses beam information and near detector measurements, which are then extrapolated with the help of Monte Carlo (MC) predictions to SK. Up to now, these MC predictions depend on hadron production models of deficient predictive power. To achieve higher precision, measurements of pion and kaon production off the carbon target are essential to tune the available MC codes. The aim of the NA61/SHINE [81, 82, 83, 84] measurements for T2K is to provide these hadro-production measurements.

The first Section 2.1 of this chapter delineates the T2K experiment with its most vital parts. It will be followed by Section 2.2 describing the goals of T2K and the requirements on the neutrino flux predictions needed to achieve them. The last Section 2.3 will relate these requirements with the NA61 experiment and will demonstrate the importance of the NA61 hadron production measurements for T2K.

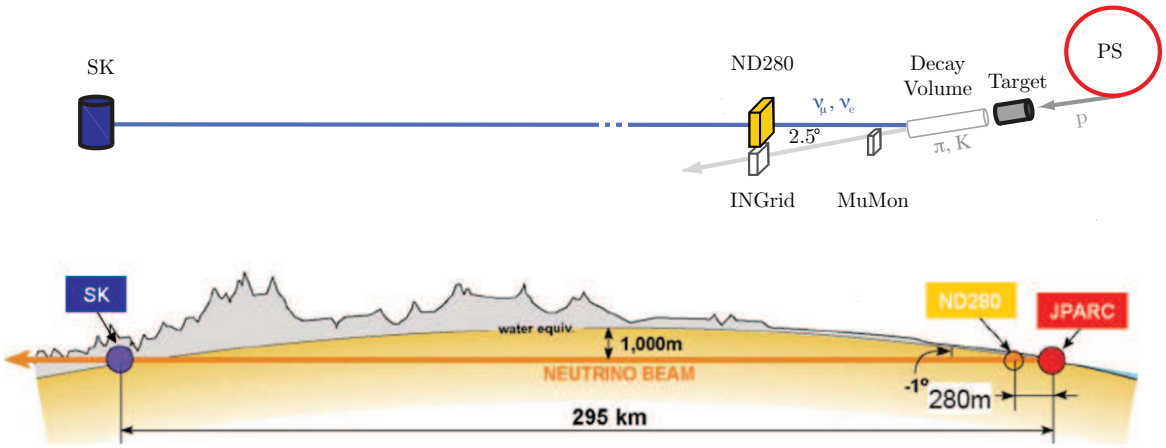

Figure 2.1: Scheme of the T2K experiment.

2.1 The T2K Experiment

The long baseline neutrino oscillation experiment T2K is located in Japan. Situated on the east coast of Japan, in Tokai-mura, the newly built Japan Proton Accelerator Research Complex (J-PARC) is used to generate the T2K neutrino beam as well as house a suite of near detectors (ND280 and Ingrid). In the west of Japan, 295 km from Tokai-mura, the Super-Kamiokande neutrino observatory (SK) is utilized as the T2K far detector (see Figure 2.1).

The starting point of the T2K experiment represents J-PARC—a multipurpose proton accelerator comprising a linear accelerator (LINAC), a Rapid Cycle Synchrotron (RCS) and a Proton Synchrotron (PS). The design energies of the three acceleration stages are 400 MeV, 3 GeV and 50 GeV, respectively. Currently, however, the energy of the LINAC and PS are limited to 200 MeV and 30 GeV, respectively. The primary neutrino beam line, as illustrated in Figure 2.2, is used to extract the proton beam and to direct and focus it with a design intensity of 3.3×10^{14} protons/pulse at a repetition rate of 0.292 Hz onto a helium cooled cylindrical graphite target of 2.6 cm diameter and 90 cm length. The target, which represents the starting point for the secondary beam line, is placed inside the first of three focusing horns designed to collimate the produced charged hadrons. The horns can be operated in both positive and negative polarity allowing to select the charge sign of the pions, which then proceed into a decay volume of $\sim$ 110 m length. The decay pipe, as well as the target station, are filled with helium gas at 1 atm to reduce absorption of in-flight pions, which subsequently decay into muons and muon neutrinos ($\pi^\pm \rightarrow \mu^\pm$ ($\overline{\nu_\mu}$)). Those that do not decay before reaching the end of the decay volume are stopped by a beam dump composed of water cooled graphite blocks. The beam dump, however, permits high energy muons to pass through and to be detected by a muon monitor (MuMon), located just behind the beam dump. The MuMon measurements will allow for monitoring the direction, profile and intensity of the beam on a spill-by-spill basis.

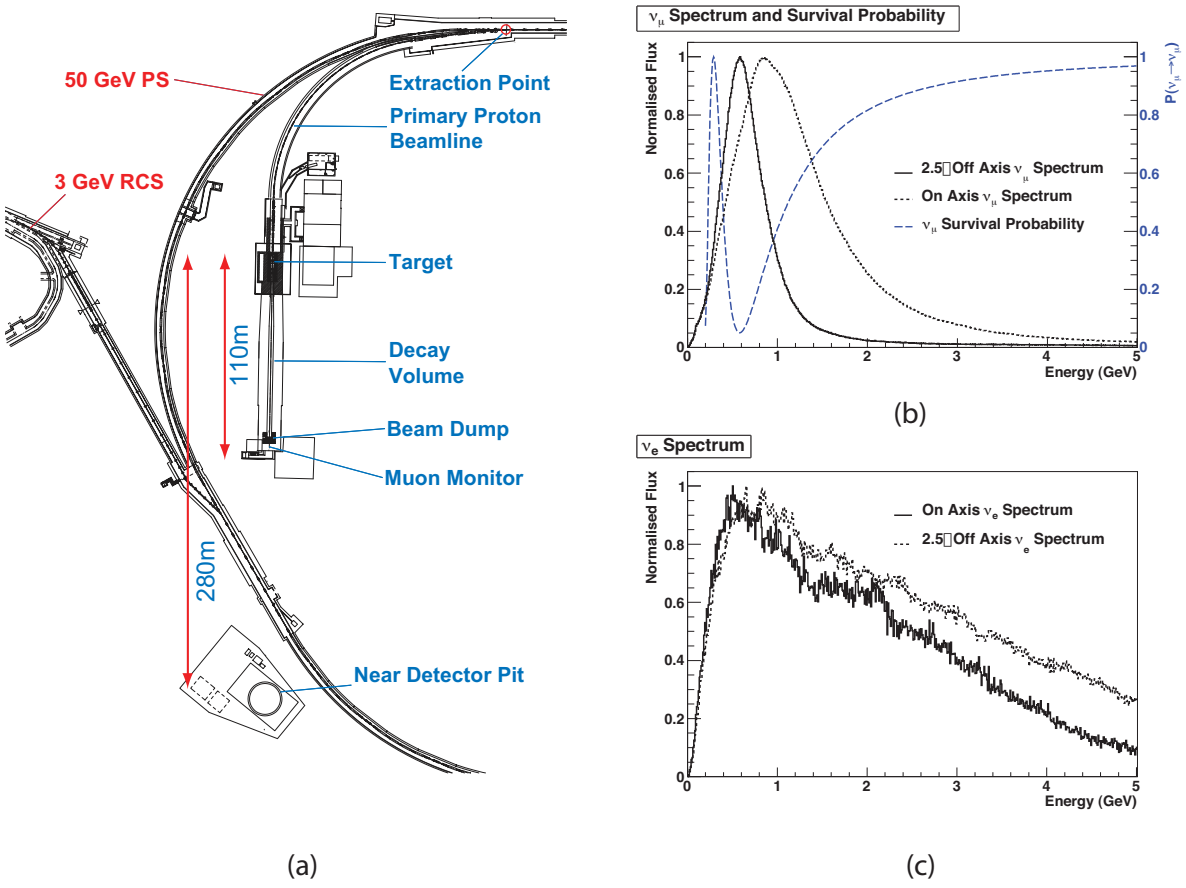

Figure 2.2: The JPARC neutrino beamline is shown in (a) along with sections of the RCS and PS. The peak normalized ν_μ (b) and ν_e (c) flux as well as the two-neutrino survival probability of ν_μ at SK (b). The figures are taken from [86].

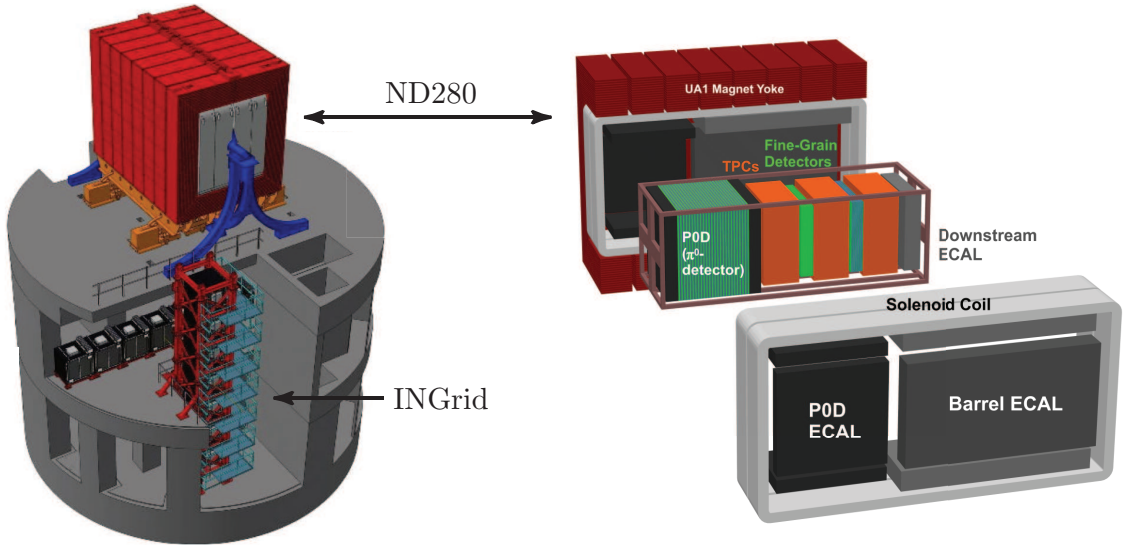

Figure 2.3: The near detector complex with INGrid and ND280. The figure is modified from [88].

The T2K neutrino beam is principally composed of ν_μ's. The average contamination level of ν_e's from the decay of kaons and muons is expected to be of the order of 1.5% [87]. As demonstrated in Figure 2.2, the on-axis beam profile is rather broad in energy, however, as one goes 2.5° off-axis one finds a low energy beam of narrow width and small high energy tail. Suppression of the latter is favorable for T2K as the neutrinos in the tail represent a large contribution to the production of neutral pions, which is a major background to electron signatures in SK. Although such an off-axis scheme [60] considerably reduces the beam luminosity, it greatly improves its quality, such that one can speak of a quasi-monochromatic beam with a peak energy resulting in an L/E ratio that coincides with the first minimum in the $P_{\nu_\mu \to \nu_\mu}$ oscillation probability. The expected ν_e contamination level in the region that corresponds to the oscillation peak (400 to 800 MeV) amounts to approximately 0.5%. It will be determined more precisely by the near detector in order to reduce systematic uncertainties on the ν_e appearance measurement. Overall, the off-axis method provides an optimal opportunity for T2K to spot a significant ν_μ disappearance as well as ν_e appearance signal.

The characteristics of the neutrino beam before oscillations are measured by a near detector complex located 280 m behind the target. This complex involves the on-axis detector INGrid (Interactive Neutrino Grid) to monitor the beam profile and the off-axis detector ND280 (Near Detector 280 m) to measure the flux and background of the neutrino beam in the direction of SK, as well as to measure neutrino cross-sections (see Figure 2.3). The INGrid detector is composed of 16 identical modules ($1 \times 1 \times 1$ m^3) made of 9 iron plates sandwiched between ten scintillator tracking planes each. 14 of the modules are arranged in such a way that they form a cross perpendicular to the beam direction, while the two others are placed at the bottom-

left and top-right parts of that cross (see Figure 2.3). Even in the early beam commissioning phase, INGrid is powerful enough to register sufficient event statistics to determine the beam direction to better than 1 mrad on a day-by-day basis, corresponding to a 1 mm beam shift at the target.

Next to INGrid, the near detector complex shelters the off-axis magnetized multipurpose detector ND280 (see Figure 2.3). ND280 consists of a collection of highly granulated sub-detectors all housed within a large magnet. The magnet—a solenoid—originates from the former UA1 experiment at CERN and provides a uniform, horizontal magnetic field of 0.2 T allowing for momentum determination of charged particle tracks. Careful design studies have been performed in order to optimize the restricted space inside the magnet ($3.5 \times 3.6 \times 7.0$ m^3) by maximizing the amount of active elements and simultaneously providing enough target mass for neutrino interactions. It resulted in a combination of the so-called π^0 Detector (P0D) and a tracking system. The P0D is optimized to measure ν_μ induced NC π^0 production with large statistics. The tracking system consists of three Time Projection Chambers (TPCs) interleaved with two Fine Grained Scintillator Detectors (FGDs) and will identify the Quasi-Elastic (QE) CC ν_μ and ν_e interactions, to measure the spectrum and energy of the neutrino beam and to determine the ratio of QE and non-QE CC interactions. P0D and tracker efficiencies are improved by measurements from the surrounding Electromagnetic Calorimeters (ECals), which detect showering (e^-, γ) particles escaping from the inner detectors. Plastic scintillation detectors, the Side Muon Range Detector (SMRD), are further instrumented in the magnet yoke to measure long range muon trajectories originating from the detector and to veto/trigger on cosmic particles. By combining all information from the different sub-detectors, ND280 aims to provide a precise and detailed knowledge of the neutrino beam parameters and neutrino interactions, by measuring the ν_μ energy spectrum, the absolute rate of the ν_μ-induced CC interactions, the ratio of QE over non-QE cross sections and the ν_μ NC π^0 production rates. This information on the neutrino beam before oscillation is essential for predicting the neutrino flux and backgrounds at the far detector. More details on the ND280 detector can be found in [85].

The far detector is provided by the Super-Kamiokande detector, which has already successfully been employed in solar, atmospheric and accelerator experiments (see Chapter 1). To date, SK represents the world's largest contained water Cherenkov detector. Situated under Mt. Ikenoyama, it is shielded from all but the highest energy[1] cosmic ray muons. As illustrated in Figure 2.4, the detector is a cylindrical, vertically oriented, stainless steel tank of 39 m in diameter and 42 m in height, containing 50 kilotons of water. A second cylinder divides the detector internally into an Inner (ID) and Outer Detector (OD). Both sides of the dividing wall are mounted with photomultipliers (PMTs), 11,146 50 cm PMTs on the inside facing inward, providing a 40% area coverage, and 1,885 20 cm PMTs on the outside facing both inwards and

[1] 1.3 TeV of minimum energy are necessary for penetration.

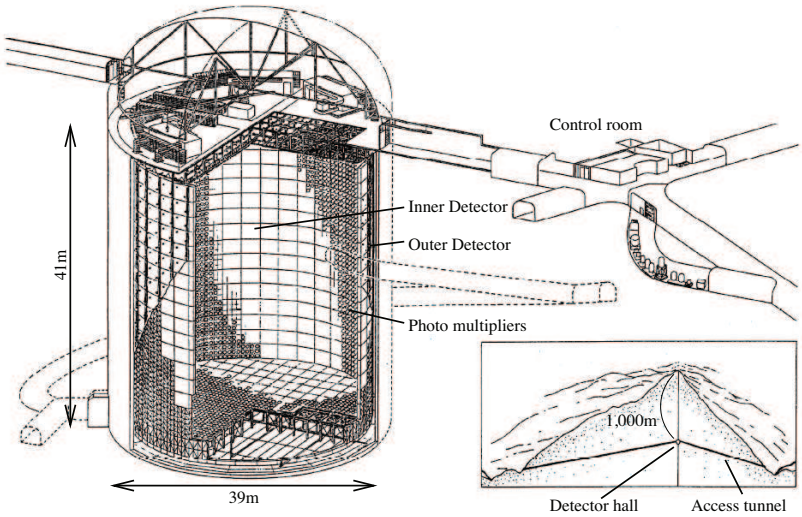

Figure 2.4: A schematic view of the Super-Kamiokande detector. The figure is taken from [3].

outwards and used as an anti-counter to identify entering/exiting particles to/from the ID. The PMTs detect the Cherenkov light produced by relativistic charged products of neutrino interactions. The shape of the resulting Cherenkov rings is clear for non-showering minimally ionizing (MIP) particles (μ or π) and fuzzy for showering electromagnetic (EM) particles (e or γ), allowing for good e/μ separation. Pulse height and timing information of the PMTs are fitted to reconstruct the vertex, direction and energy of the incoming neutrinos and for particle identification from the Cherenkov rings. In order to identify only those neutrinos at SK which have been produced at JPARC, T2K uses the Global Positioning System (GPS) for synchronizing the timing between the beam pulse extraction time at the accelerator and the trigger time at SK. Muon neutrinos are then detected at SK using CCQE interactions, in which the muons produce muon-like rings, while electron neutrinos are identified via CCQE interactions leaving electron-like rings. Mis-reconstruction of ν_μ induced neutral current π^0 events as electron-like events results in a major background to the ν_e appearance measurement in T2K. To reduce systematics of this background, the ν_μ NC π^0 cross-section measurements from the ND280 detector will come into play.

A major milestone for the completion of the T2K experiment has been achieved when the first protons were successfully transported to the T2K production target and beam was detected by the MuMon on April 23$^{\text{rd}}$, 2009. Installation of the on-axis (INGrid) and off-axis (ND280) detectors was (mainly[2]) finished for the first physics run conducted from January

[2]A part of the ECals (Barrel ECal and P0D ECal (see Figure 2.3)) was missing for the first physics run, but has been completed during the shutdown in summer 2010.

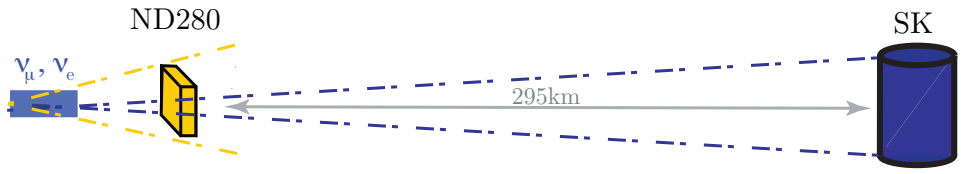

Figure 2.5: Schematic comparison of the angular acceptance of ND280 and SK.

23rd to June 26th, 2010. With a stable beam power of about 50 kW, a total data of 3.28×10^{19} protons on target (pot) has been accumulated. Continuous running resumed after the summer shutdown in November 2010 and first physics results are expected early 2011.

2.2 Goals of T2K

The T2K experiment aims to search for $\nu_\mu \rightarrow \nu_e$ appearance with a sensitivity to $\sin^2 2\theta_{13} \approx 0.008$ (90% C.L.) [89], which is an improvement by more than an order of magnitude with respect to present limits. Due to the fact that the appearance probability not only depends on θ_{13} but also on the atmospheric oscillation parameters θ_{23} and ΔM^2 (see Equation 1.12), it is of importance to further make precision measurements of these mixing parameters. Measuring the atmospheric parameters yet is rewarding on its own right, given that it is of great interest to test whether θ_{23} is maximal. T2K will therefore also investigate the ν_μ disappearance. The nominal T2K statistical power, assuming 5 years of running with 0.75 MW on target, would allow for improving current measurements from MINOS, SK and K2K (see Chapter 1) to a precision of $\delta(\sin^2 2\theta_{23}) = 0.01$ and $\delta(\Delta M^2) = 10^{-4}$ eV^2 [3].

Both oscillation analyses are probed by comparing observations at SK with predictions with or without oscillations. Predictions of the ν_μ and ν_e fluxes at SK (Φ_μ^{SK} and Φ_e^{SK}) are determined as products of the ND280 measurements (Φ_μ^{ND} and Φ_e^{ND}) and the far-to-near (F/N) ratios, denoted R_μ and R_e, respectively, as defined by the following equation:

$$\Phi_{\mu,e}^{SK}(E_\nu) = R_{\mu,e}(E_\nu) \cdot \Phi_{\mu,e}^{ND}(E_\nu) \quad . \tag{2.1}$$

In case of a point-like and isotropic neutrino source the F/N ratio is given by the solid angle and is energy independent. In practice, however, as illustrated in Figure 2.5, the near detector is located rather close to the decay tunnel and is therefore sensitive to the finite length (∼110 m) of it. Consequently, the near detector accepts a broader solid angle of the neutrino beam than the far detector does. This leads to a complicated F/N ratio spectrum (see Figure 2.6), which depends on the neutrino energy and is determined by the momentum distributions of hadrons at production and on the geometry of the neutrino source. Thus, in order to evaluate the central value and error of the F/N ratio and, hence, of the predicted SK observables, detailed

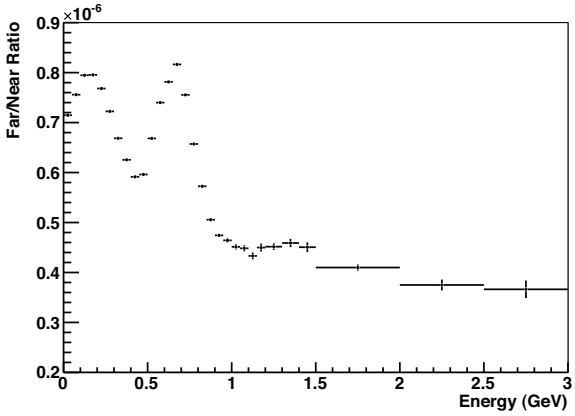

Figure 2.6: Energy dependence of the F/N ratio for ν_μ's based on MC simulations. The figure is taken from [90].

information on the hadron production off the T2K target is needed.

Up to now, no direct measurements of the production of pions and kaons—the main contributors to the neutrino flux in T2K (see Section 2.3)—exist for 30 GeV proton–carbon interactions (see Section 1.6). The closest available data points are for pions at 12 GeV from HARP [94], for which no information is yet published on the kaons, and for pions at 158 GeV from NA49 [95]. This experimental situation would necessitate to rely on hadron production models used to treat primary and secondary interactions in the T2K beam simulation (JNUBEAM[3]).

Systematic uncertainties on the neutrino flux predictions and the F/N ratio that would come from the use of hadronization models, have been estimated by comparing the results from three different models—GCALOR [93], GFLUKA [92] and GHEISHA [92]. Figure 2.7 shows the ν_μ and ν_e flux predictions for the different models. It clearly demonstrates that discrepancies between these models are notable and that they lead to differences in the absolute neutrino fluxes of up to a factor 2. Such large uncertainties on the flux predictions would strongly degrade the precision of the neutrino cross section measurements in the near detector. Variations of the neutrino fluxes would furthermore influence the far-to-near ratio. In Figure 2.8 it is demonstrated that differences between the models can lead to discrepancies between the respective F/N ratios which are larger than 3%. Such a large uncertainty is not acceptable for the designated T2K goals, taking into account that there are other contributions to the overall systematic error on the oscillation analyses coming from the near detector measurements, neutrino cross sections, efficiencies etc. To reduce the error on the F/N ratio to a negligible level compared to other contributions, a precision of $\delta(R_{\mu,e}) \leq 3\%$ is required. For achieving this precision on the F/N ratio, and thus, the original T2K goals, adequate particle production

[3]Detailed information about JNUBEAM can be found in [91].

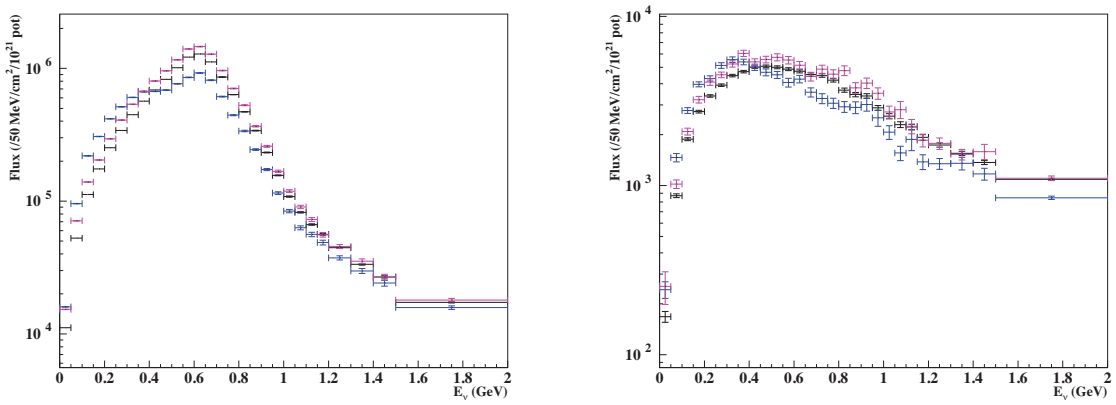

Figure 2.7: ν_μ (left) and ν_e (right) flux at SK using different models for simulating primary and secondary interactions: GCALOR (black), GFLUKA (purple) and GHEISHA (blue). Both figures are taken from: [91].

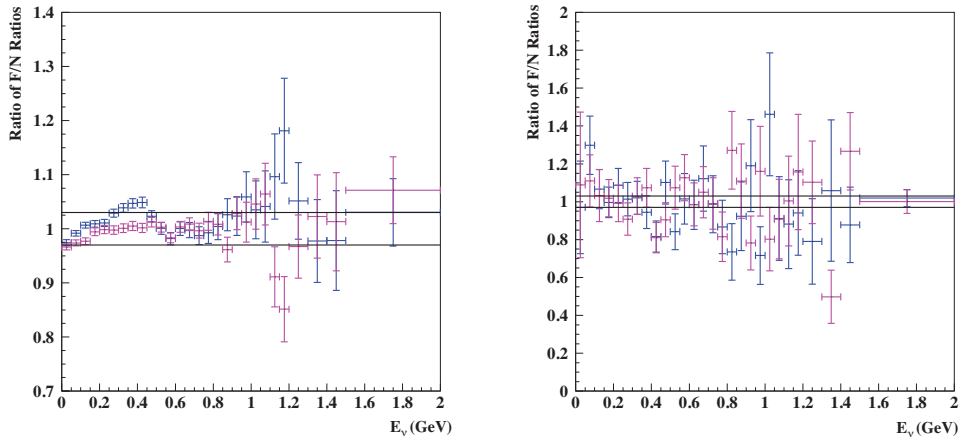

Figure 2.8: Ratios of F/N ratios computed with GHEISHA (blue) and GFLUKA (purple) with respect to the reference ratio computed with GCALOR for ν_μ (left) and ν_e (right). The horizontal black lines show the $\pm 3\%$ band. Both figures are taken from: [91].

measurements are essential to tune the MC codes and enhance their predictive power. The aim of the NA61/SHINE measurements for T2K is therefore to provide precise hadro-production measurements.

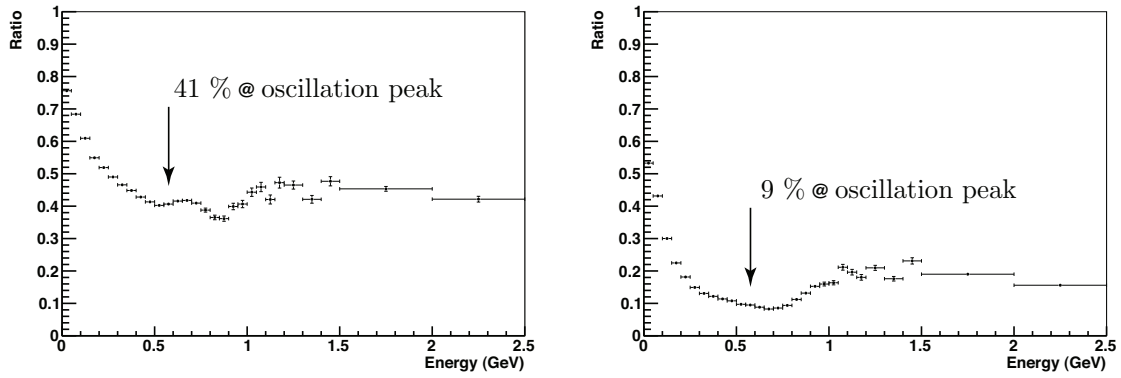

Figure 2.9: The ratio of indirect contribution over total (left) and the ratio of out-of-target over total (right) for ν_μ's at SK. The indirect contribution adds approximately 41% to the region under the oscillation peak ($\sim$ 650 MeV) and the out-of-target contribution about 9%. Both figures are taken from [90].

2.3 T2K Requirements on NA61

The T2K experiment requires adequate hadro-production measurements from the NA61/SHINE experiment for a reliable calculation of the neutrino fluxes. In order to reach a precision on the F/N ratio of less than 3%, requirements on the NA61 measurements were formulated, which are matched to the particular needs of T2K.

The first requirement from T2K concerns the beam energy used for measuring the hadron production in inelastic p+C collisions. As the current T2K beam energy is limited to 30 GeV, initial measurements in NA61 should be conducted with 30 GeV kinetic energy protons. Subsequent measurements at 40 and 50 GeV may be necessary later on.

The data to be collected for T2K should comprise different carbon target configurations. With a thin carbon target, of no more than 2 cm length ($\sim$ 0.04 interaction length), the p+C nucleus cross sections are to be evaluated. These are important for measuring the primary particle production in p+C collisions without distortions due to target reinteractions. These measurements can then be used to tune the JNUBEAM simulation for the direct contribution to the neutrino flux coming from primary interactions in the T2K target. Neutrino parents are however not only produced in the primary proton interaction, but can also stem from reinteractions inside or outside of the T2K target. The contribution to the neutrino flux that is coming from these neutrino parents of higher generation is called indirect contribution. Figure 2.9 shows that the indirect parents from reinteractions inside the T2K target significantly contribute to the neutrino flux. To take this into account, NA61 measurements should also be performed with a T2K replica target, of 90 cm length ($\sim$ 1.9 interaction lengths) and 2.6 cm diameter, which allows to study the full particle yield in the T2K target including primary as

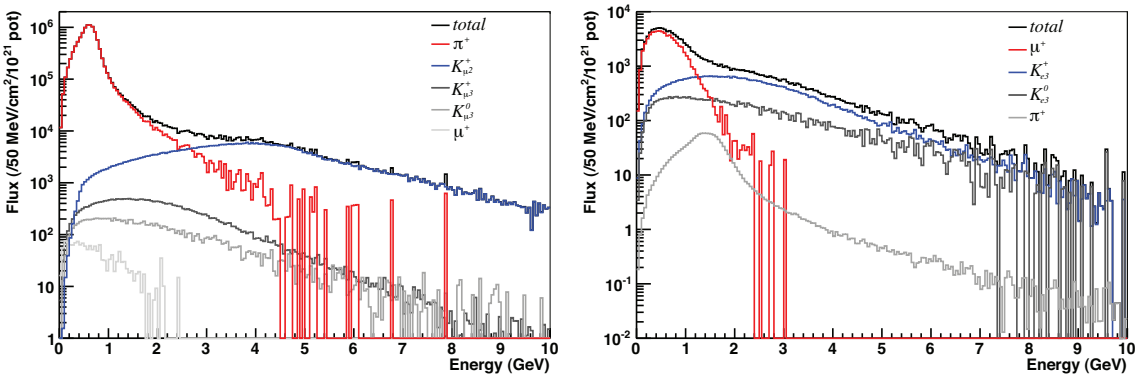

Figure 2.10: ν_μ (left) and ν_e (right) energy spectrum at SK. ν_μ's are primarily produced via π^+ (95.2% for $E_\nu \leq 3$ GeV) and K^+ (4.5% for $E_\nu \geq 3$ GeV) two-body decays, and ν_e's via μ^+ (54.2% for $E_\nu \leq 1.6$ GeV) decays and three body decays of K^+ (31.7%) and K^0_L (13.1%) for higher energies. Protons and Λ's only contribute indirectly to the neutrino flux. Precise numbers have not been estimated yet. Both figures are taken from [90].

well as higher order interactions. The particle spectra measured with the replica target can further be used as input to the beam MC simulation. Both, the thin and T2K replica target, are provided by the T2K Collaboration, so that they are built out of the exact same graphite grade as the T2K targets are.

For the various p+C measurements NA61 is requested to provide incoming proton normalized and efficiency as well as acceptance corrected particle yields over a wide range of phase space, while keeping the systematic error on the determination of the absolute yield within a few percent. As $\pi^\pm$, $K^\pm$, K^0_S and Λ^0 particles contribute directly or through decay chains to the neutrino production in T2K (see Figure 2.10), it is of importance to measure the yields for all of these particle species. Further data on protons should be provided to be used for a proper simulation of the additional contribution to the neutrino flux, which is coming from reinteractions in the T2K target itself, the surrounding target cooling envelope and the focusing horns. The phase space region to be covered for the various particle types is summarized in Table 2.1. They have been estimated with the JNUBEAM simulation by studying the momentum and angular distribution of the particles contributing to the neutrino flux in the T2K detectors. For positively charged pions, which represent by far the main contributor to the neutrino flux, a typical precision of 5% should be reached. For positively charged kaons, which come second in the neutrino flux contribution, it is fair to determine the K^+/π^+ ratio integrated over the whole phase space within 10%. To reach such a precision at least 200k reconstructed π^+ tracks are required for the thin target configuration, while for the replica target it is a few times the thin target statistics which is needed. A more precise quantitative requirement for the

Particle Species	Momentum Range [GeV]	Angular Range [mrad]
$\pi^{\pm}$	$0.5 - 10$	$0 - 400$
$K^{\pm}$ and K^0_S	$1 - 20$	$0 - 300$
Λ^0	$2 - 25$	$0 - 200$

Table 2.1: Phase space to be covered by the NA61 hadro-production measurements. Values are taken from [97].

replica target statistics is still under investigation as it depends on the binning scheme, that is currently formulated. Recent studies [96] have shown variations of the absolute neutrino fluxes and the far-to-near ratio predictions as a function of the neutrino parent particle exiting point from the target as well as of the beam profile used in the simulation (pencil beam, centered or shifted beam position, beam divergence etc). Therefore, sufficient data with the replica target should be taken to allow for differential reconstruction in longitudinal bins along the target (exiting point of tracks on the target skin) and radial bins (impact point of beam protons on the target). For each data set, the transverse profiles of the incident proton beam are furthermore of importance, so as to be able to compare it to the respective profiles of T2K.

Chapter 3

The NA61/SHINE Experiment

The NA61/SHINE (SPS Heavy Ion and Neutrino Experiment) experiment is a large acceptance hadron spectrometer combining a rich physics program in various fields [81, 82, 83, 84]. Besides performing measurements for the T2K experiment, it takes a variety of data used for the description of cosmic-ray air showers in the Pierre Auger [98] and KASCADE [99] experiments, as well as for studying the behavior of strongly interacting matter at high density. To successfully complete such a broad physics program, a detector is required, which meets the needs of the different objectives. The NA49 detector [69] was seen as an ideal starting point as its large acceptance spectrometer was developed for the study of hadron production in p+p, p+A, and A+A collisions, offering a typical precision on the measured particle yields of about $5-10\%$ (3% for p+p data). NA61 therefore inherited its main detector components from NA49 and upgraded it with a few additional detectors well adapted for the particular requirements. The detector is located in one of CERN's experimental sites, the so-called North Area, from which also the name NA61 derives. It is a fixed target experiment served with the H2 beam line of the Super Proton Synchrotron (SPS).

In the following Section 3.1 a quick glance at CERN's accelerator complex with the focus on the SPS is taken. Section 3.2 then briefly describes the experimental setup of NA61 while concentrating on the parts relevant for T2K data taking. For more information about the NA61 detector please refer to [81, 69]. In the final Section 3.3 emphasis is placed on the setup of the beam line with its targets, trigger and beam detectors, which is of importance for the cross section measurements discussed in Chapter 6.

3.1 CERN's Accelerator Complex

CERN's accelerator complex has been developed and modified over the past half century [101, 102, 103]. Nowadays, it comprises a large variety of accelerators to supply the various ex-

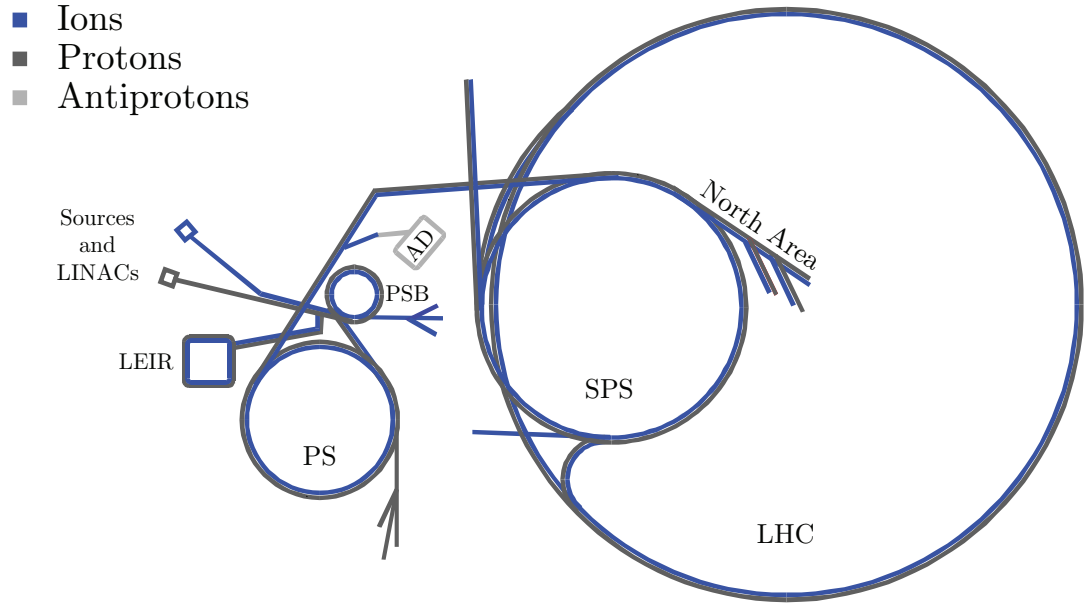

Figure 3.1: CERN's accelerator complex with its sources and LINACs, the Antiproton Decelerator (AD), PS Booster (PSB), Low Energy Ion Ring (LEIR), Proton Synchrotron (PS), Super Proton Synchrotron (SPS) and the Large Hadron Collider (LHC), as well as the North Area, where NA61 is located. Sketch is not to scale.

periments in the field of particle and heavy ion physics with lepton, hadron and ion beams. Figure 3.1 depicts its most essential parts. The different accelerators are linked together building a chain of accelerators with increasing energy. For protons this chain starts with the linear accelerator LINAC2, then continues with the PS Booster (PSB), the Proton Synchrotron (PS), the Super Proton Synchrotron (SPS) and finally the Large Hadron Collider (LHC). Their operation is realized in so called super-cycles allowing to combine acceleration cycles for different purposes and serving several users at the same time. During NA61 data taking for T2K, the SPS super-cycle took 40 s. Part of this time was used to accelerate protons for NA61 in the PS to 14 GeV/c and to fill them into the SPS (6.9 km diameter), where they were further accelerated to 400 GeV/c. Thereby, beam intensities of about $3 \cdot 10^{13}$ protons per spill, which lasted about 9 s per super-cycle, were reached.

The SPS beam can be extracted for serving fixed-target experiments located in the experimental halls of the North (NA) and the West Area (WA). North Area is where the NA61 experiment is located and supplied with a beam from the H2 beam line. The H2 beam line offers primary protons at 400 GeV/c, as well as secondary hadrons, electrons or muons of energies between 10 and 360 GeV/c. Secondary beam particles are produced by directing the primary beam onto the so-called T2 target located at the beginning of the H2 beam line. A row of collimators is then used to control the momentum and intensity of the secondary beam, while fine steering and focussing towards the experiments is performed with bending

magnets (BENDs), correction dipoles (TRIMs) and quadrupoles (QUADs). In addition, the H2 beam line is equipped with a Cherenkov Differential counter with Achromatic Ring Focus (CEDAR) [122], which allows for tagging particles according to their velocity and, due to the fixed beam momentum, also according to their particle mass. Desired particle types can furthermore be selected by a threshold gas Cherenkov counter. Pressure settings for both Cherenkov counters during the NA61 data taking for T2K and the resulting beam purity are discussed in Chapter 5. Further beam detectors and counters as well as the material budget in the beam line right in front of the NA61 detector are discussed in Section 3.3.

3.2 Overview of the Experiment

The NA61 experiment is a large acceptance hadron spectrometer for the study of hadronic final states produced in collisions of various beam particles (e.g. p, π, Pb, C, Si) with different fixed targets. The detector layout is presented in Figure 3.2 (see also Figure 3.4). The main tracking devices are four large volume Time Projection Chambers (TPCs), which allow for the detection of approximately 70% of charged produced hadrons.

Two of the time projection chambers, the Vertex TPCs (VTPC-1/-2), are located within two superconducting dipole magnets (VTX-1/-2) providing a magnetic field perpendicular to the beam direction of up to 1.5 T and 1.1 T (standard configuration for 158 GeV/c data taking, *std*), respectively. Together, the magnets result in a maximum bending power of 9 Tm and can be operated in both polarities (*std*+/-). During the T2K data taking at 30 GeV beam energy the magnetic field was reduced by a factor of eight ($^1/_8$ *std*+) in order to optimize the overall geometrical acceptance. The magnetic field allows to expand the produced particle cone, thus to reduce the track density, as well as to identify the particle momenta via the following expression

$$p\ [\mathrm{GeV/c}] = 0,3 \cdot q\ [\mathrm{e}] \cdot B\ [\mathrm{T}] \cdot R\ [\mathrm{m}] \cdot \frac{1}{\cos\lambda} \quad , \tag{3.1}$$

Here, p and q denote the particle momentum and charge, respectively, B the magnetic field, R the radius of curvature of the track and λ the angle between the track and the bending plane. Depending on the phase space region a resolution of $\sigma(p)/p^2 \cong (0.3 - 7) \cdot 10^{-4}$ $(\mathrm{GeV/c})^{-1}$ is reached. Two more time projection chambers, the Main TPCs (MTPC-R/-L), are situated downstream of the magnets, symmetrically to the beam line. Note that the geometrical acceptance of the Vertex and Main TPCs are limited by the fact that the region around the beam axis is excluded from the sensitive volumes. Altogether, the TPCs offer identification of charged particles ($\pi^{\pm}$, $\mathrm{K}^{\pm}$, p, $\overline{p}$, $\mathrm{e}^{\pm}$, d and $\overline{d}$) via measuring the particles' ionization energy loss per unit of length ($\mathrm{d}E/\mathrm{d}x$[1]) in the TPC gas. Thereby a resolution of $\sigma(\mathrm{d}E/\mathrm{d}x)/<\mathrm{d}E/\mathrm{d}x> \approx 0.04$

[1]The energy loss of a charged particle when it passes through matter depends on the particle's velocity

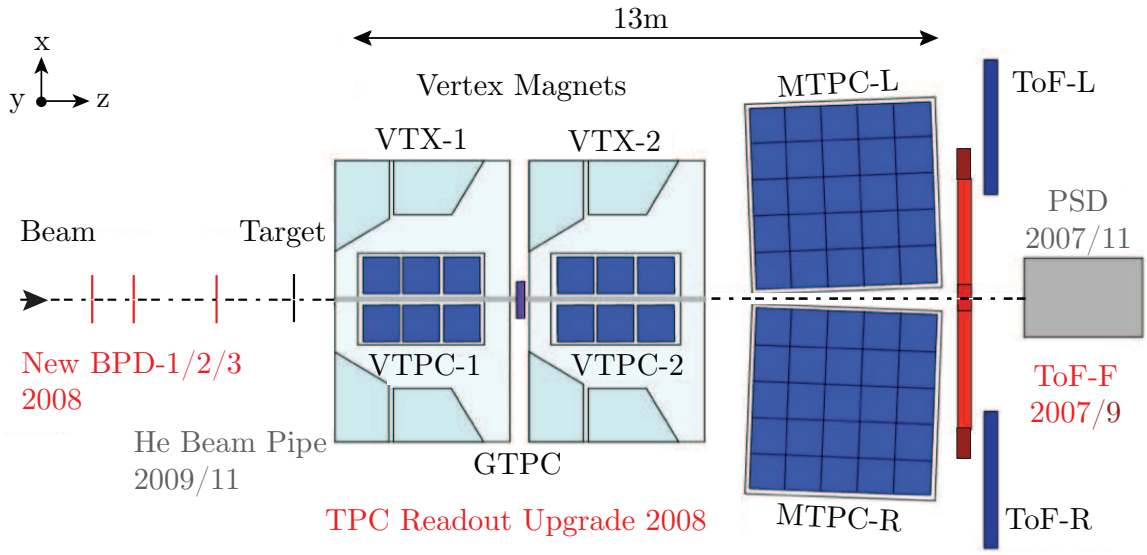

Figure 3.2: Schematic setup of the NA61/SHINE experiment at the CERN SPS. Basic upgrades and years of their realization relevant for the T2K data taking are indicated in red. The magnetic field bends charged particle trajectories in the $x - z$ (horizontal) plane.

is reached. More technical details about the NA61 TPCs and the principle of their operation are discussed in the following subsection.

The presented TPC system is extended in the beam direction with a small-size chamber, the Gap-TPC (GTPC). The device is placed between VTPC-1 and VTPC-2 such that the beam passes through its sensitive volume. It allows to measure short piece trajectories of high momentum charged particles, which are passing through the gap of the VTPCs and MTPCs. In particular for the analysis presented in this thesis the GTPC plays a relevant part. More technical details about the GTPC are presented together with the other TPCs in the following subsection.

The particle identification (PID) capability of the TPCs is complemented through time of flight measurements[2] using several Time Of Flight (TOF) detector arrays in the phase space region, where the specific energy loss functions of different particles overlap. Two of the NA61 TOF detectors, the TOF-Right and -Left (TOF-R/-L), stem from NA49 and have a time measurement resolution of $\sigma \approx 60$ ps. An additional TOF wall, the Forward TOF (TOF-F),

and is described by the Bethe-Bloch formula. Particles can thus be identified by simultaneously measuring their momentum and $\mathrm{d}E/\mathrm{d}x$. For more detailed explanations about particle identification via $\mathrm{d}E/\mathrm{d}x$ see for example [123].

[2]Measuring a particle's time of flight over a known distance allows to determine its velocity. If, in addition to that, one knows the particle's momentum, which is in NA61 given from the TPC measurements, one can determine the particle's mass. For more detailed explanations about particle identification via TOF measurements see for example [124].

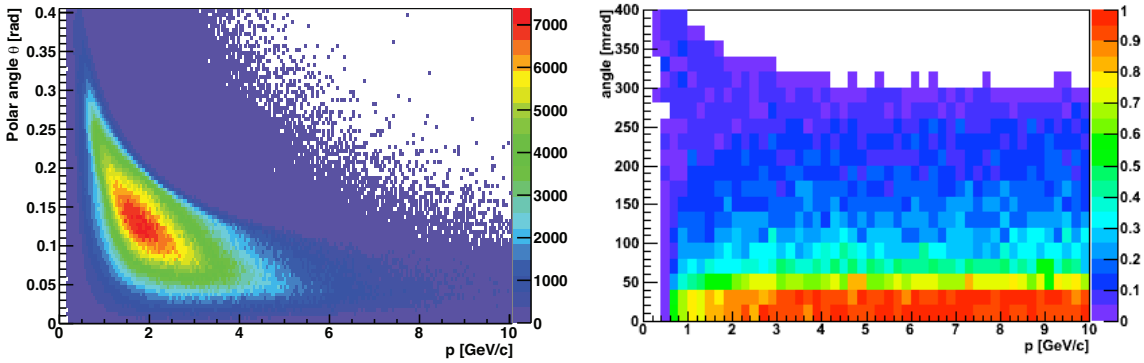

Figure 3.3: *Left:* MC particle distribution in momentum and polar angle plane for π^+ giving neutrinos in SK. The figure is taken from: [90]. *Right:* Combined geometrical acceptance of all 3 TOF detectors (TOF-R/-L/-F). The figure is taken from: [124].

was installed in 2007 in order to extend the PID acceptance to low momenta ($p < 4$ GeV/c). It allows to fully cover the phase space region of interest for T2K, as demonstrated in Figure 3.3, where the Monte Carlo (MC) distribution of π^+ yielding neutrinos in SK is compared to the overall TOF geometrical acceptance region in NA61. The TOF-F detector consists of eight modules with eight scintillator bars ($120 \times 10 \times 2.5$ cm^3) each, oriented vertically, and read out on both sides with Hamamatsu R1828 photo-multipliers. It has an expected resolution of $\sigma \approx 120$ ps. For the 2009 data taking (see Chapter 4) the forward TOF was extended by two further modules resulting in an improved acceptance at lower momentum. For more information see [124].

Targets are placed on the beam axis in front of the VTX-1 magnet. More details about the targets, which have been used for the T2K data taking, are presented in Section 3.3. Also the beam and trigger detectors, which are located in the beam line, will be discussed later on (see Section 3.3).

While during the 2007 data taking only one trigger configuration could be recorded at a time, changes of the trigger logic introduced for the 2009 run now allow to simultaneously record data of different trigger conditions prescaled by a certain factor. Once a given trigger condition is fulfilled, the readout of the different detectors starts. Digitized detector signals are reduced in raw data size and then transferred to the central Data AcQuisition (DAQ) system. The DAQ brings the raw data of all detectors in a standardized form and transfers them to the CERN Central Data Recording (CDR) facility where they are written to disk storage. The new trigger logic furthermore stores the trigger monitor scalers a second time in the so-called trigger monitor files. Since the TPC readout and DAQ upgrade in 2008, an event rate of ∼70 events/sec is reached, which corresponds to an increase of a factor 10 with respect to the original NA49 DAQ system [125]. A detailed description of the current central DAQ can be

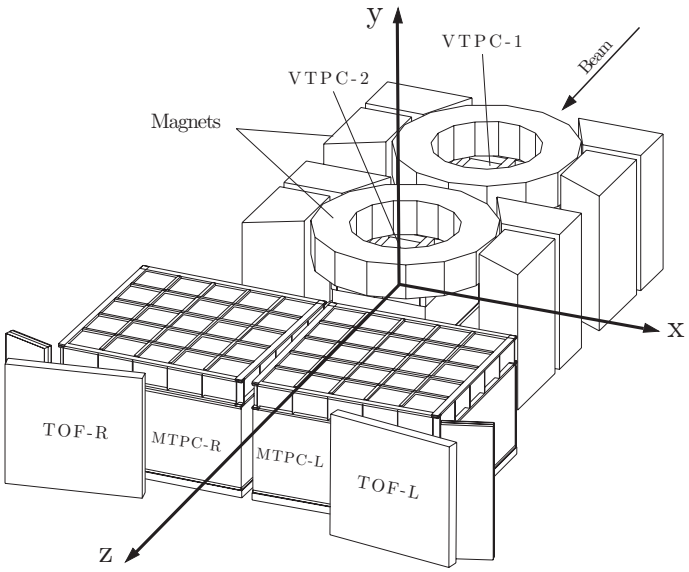

Figure 3.4: The NA61 coordinate system.

found in [126]. The raw data files are stored on the CERN Advanced STORage (CASTOR) management system, from where they can be accessed for data processing (see Chapter 4).

The NA61 coordinate system is a right-handed Cartesian coordinate system with origin in the middle of VTPC-2 (see Figure 3.4). The orientation of the coordinate system is defined by the direction towards the Jura mountains (x), the drift direction of electrons in the TPCs (y) and the beam axis (z). For the magnetic field configuration *std+*, which has been used during the T2K data taking, positive particles are bent toward the positive x-axis, which means towards the left side of the detector. Coordinates presented in the course of this thesis refer to the NA61 coordinate system.

The NA61 Time Projection Chambers

The NA61 time projection chambers are essentially multi-wire proportional chambers which are extended by a drift volume. They allow for three-dimensional track reconstruction and mainly consist of a multi-wire section, a readout plane and a sensitive drift volume, which is filled by a gas and surrounded by field shaping electrodes that form a homogeneous electric field.

In NA61, the sensitive TPC volumes have a cuboidal shape with a readout chamber in the $x - z$ plane on the top end. This is illustrated in Figure 3.5 using the example of the GTPC. A homogeneous field is produced between the base plate and the readout chamber by strips of Mylar foil coated with aluminum which are surrounding the sensitive volumes. The dimension

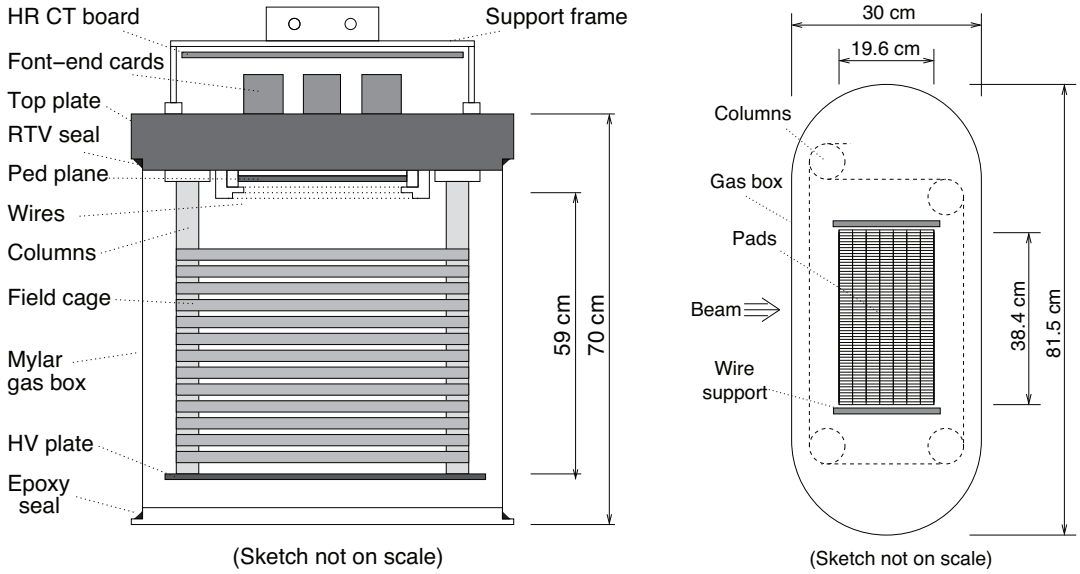

Figure 3.5: Schematic setup of the GTPC. *Left:* Front view from the beam direction. *Right:* View from the bottom. Both figures are taken from: [100].

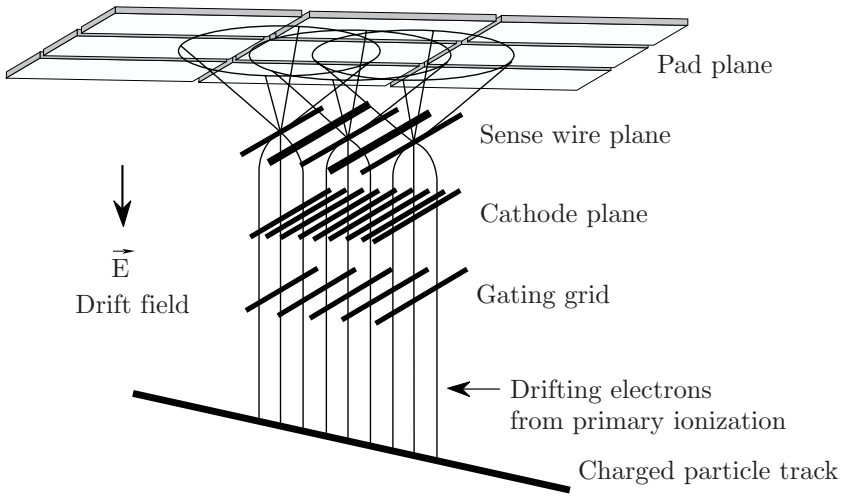

Figure 3.6: Layout of the TPC readout chamber. The figure is taken from: [69].

	VTPC-1/2	MTPC-L/-R	GTPC
Volume [m^3]	$2 \times 2.5 \times 0.98$	$3.9 \times 3.9 \times 1.8$	$0.384 \times 0.196 \times 0.590$
Gas	Ar/CO_2 (90/10)	Ar/CO_2 (95.5/5.5)	Ar/CO_2 (90/10)
Drift Voltage [kV]	13	19	11
Drift Velocity [cm/μs]	1.4	2.3	$\sim$1.2
Number of Pads	27648	63360	672
Pad Dimension [mm]	3.5×16/28	3.6/5.5×40	4×28

Table 3.1: Technical parameters of the NA61 TPCs.

and gas compositions of the sensitive volumes are listed in Table 3.1 together with additional technical parameters of the NA61 TPCs.

When charged particles traverse the sensitive detector volume they ionize the gas along their trajectory due to Coulomb interaction. Free electrons from the ionization process then drift in the electric field towards the read-out chamber (see Figure 3.6). Their drift-velocity does not only depend on the electric field, but also on the composition, pressure and temperature of the gas, which is why these parameters have to be monitored constantly to allow for a precise track reconstruction. When the drifting electrons arrive at the readout plane they first have to pass the gating grid. The gating grid is open during readout time, which means that it is at the same potential as the drift field at that point, thus letting the electrons drift through. The gating grid is followed by a cathode plane which is at 0 V and which separates the drift volume from the amplification region. After the electrons have passed the cathode plane they are accelerated in the electric field of the sense wire plane producing an avalanche of electrons. While the electrons are quickly absorbed by the wires, the remaining, much heavier, positively charged ions induce a mirror charge on the readout pads before they slowly drift towards the cathode plane. At that time the gating grid is closed meaning that alternating wires are brought to $\pm$100 V relative to the drift field. This prevents the ions from drifting in the sensitive detector volume as well as unwanted drift electrons from entering the readout chamber.

Pad signals are read out in 256^3 time samples of 200 ns each and then amplified, shaped and digitized by Front-End Cards (FEC) located directly on the back of the readout plane. Since the TPC readout upgrade, Mother boards (MB) collect the FEC signals, perform pedestal subtraction, noise suppression and zero compression and send the data to Concentrator Boxes (CB). The CBs serialize the incoming data streams and multiplex them into a single 32-bit

[3] 512 time samples of 100 ns each for some calibration runs.

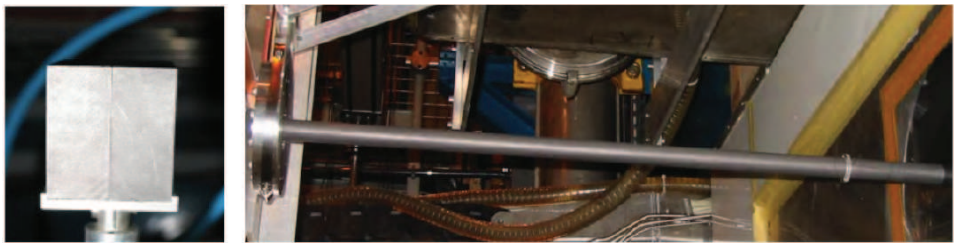

Figure 3.7: Pictures of the thin (left) and T2K replica (right) targets, which are used for the NA61 data taking for T2K.

	Thin Target	**Replica Target**
Material	Isotropic Graphite	Isotropic Graphite
Density [g/cm^3]	1.8395	1.831
Dimension [cm]	$2.5 \times 2.5 \times 2.0$	$\varnothing = 2.6$, length $= 90$
Interaction length	$\sim 0.04\lambda$	$\sim 1.9\lambda$
$z-$position [cm]	-580.4	-607.7

Table 3.2: Summary of thin target and replica target properties. The $z-$position is given with respect to the target center.

wide data stream, which is then transmitted to the server PCs of the central DAQ. More about the TPC DAQ can be found in [126]. During data processing of the raw data pixels are merged into space points allowing for reconstruction of the particle tracks (see Chapter 4).

3.3 Setup of the Beam Line

Targets for T2K Data Taking

T2K data taking is performed with two carbon targets of different lengths (see Figure 3.7). One is referred to as thin target and the other one as T2K replica target. As the name of the latter already implies, it is a replica of the target used in T2K. Table 3.2 summarizes the dimension, material properties and $z-$position of the target center with respect to the NA61 coordinate system for both targets.

The replica target is used to study all particles produced in the T2K target, regardless of whether they stem from primary, secondary or higher order interactions. More on the analysis and use of the long target data can be found in [121]. In contrast, the thin target is used to

	Dimension [cm]	Position [cm]
S1	$6 \times 6 \times 0.5$	-3638
S2 (2007)	$2 \times 2 \times 0.2$	-1442
S2 (2009)	$\varnothing = 2.8$, length $= 0.2$	-1442
V0	$\varnothing = 8$, length $= 1$, $\varnothing = 1$ hole	-1413
V1	$10 \times 10 \times 1$, $\varnothing = 1$ hole	∼-675
V1′ (2009)	$30 \times 30 \times 1$, $\varnothing = 2$ hole	∼-678
S4	$\varnothing = 2$, length $= 1$	-212

Table 3.3: Dimension of the scintillator counters in the beam line and their $z-$position with respect to the NA61 coordinate system.

measure only primary interactions in the target, which allows to evaluate the proton–carbon nucleus cross section. Work presented in this thesis is based on the thin target data.

Trigger and Beam Setup

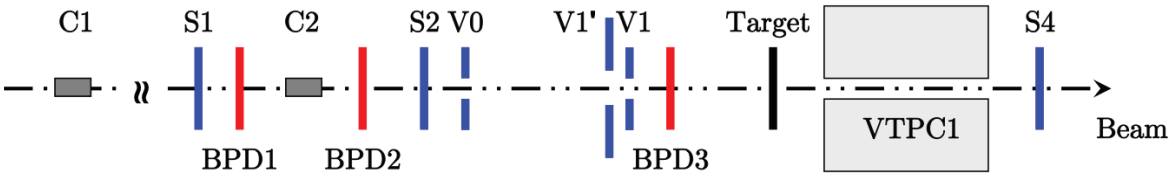

Figure 3.8: Layout of the NA61 beam and trigger counters. Sketch is not to scale. Note, that V′ has not been used during the 2007 data taking. See text for details.

The NA61 cross section measurements with the thin carbon target necessitate a minimum bias trigger in order to select interactions in the target, which are generated by a clean sample of protons of 31 GeV/c. Therefore, a trigger and beam setup as illustrated in Figure 3.8 is used. With this setup, beam particles in the secondary hadron beam are identified by two Cherenkov counters, a Cherenkov Differential counter with Achromatic Ring Focus (CEDAR) [122] and a threshold counter, labeled C1 and C2, respectively. The CEDAR counter, through the use of a 6-fold coincidence, provides positive identification of protons, while the threshold Cherenkov counter, operated at pressure lower than the proton threshold, is used in anti-coincidence in the trigger logic. The CEDAR pressure was set to 3.3 bar and one of the threshold Cherenkov counters to 1.65 bar. Two scintillator counters, S1 and S2, provide beam

	Coordinate	2007 Position [cm]	2009 Position [cm]
BPD1	x	-0.0125	0.345
	y	0.4675	0.115
	z	-3623.58	-3628.58
BPD2	x	0	0.335
	y	0.4425	0.3
	z	-1484.54	-1489.54
BPD3	x	0.006	0.245
	y	0.38	0.26
	z	-662.66	-657.355

Table 3.4: Position of the BPDs with respect to the NA61 coordinate system for the 2007 and 2009 data taking with the thin target. Values are taken from the NA61 data base.

definition and timing, together with the two veto counters, V0 and V1, each with a 1 cm large hole, which reduce the background from upstream interactions. During 2009 data taking an additional veto counter of large size, called V1′, was used to further reduce fake triggers. S1 also provides the start signal for the TOF detectors. For further information about the dimension and position of the scintillator counters see Table 3.3. Beam protons are selected by the coincidence $S1 \cdot S2 \cdot \overline{V} \cdot C1 \cdot \overline{C2}$. For the 2007 data taking V represents the OR of the two veto counters V0 and V1, while for the 2009 data taking the OR of V0, V1 and V1′. The trajectory of the beam particles is precisely measured by three two-plane multi-wire proportional chambers, the Beam Position Detectors (BPDs). Their positions with respect to the NA61 coordinate system are given in Table 3.4 for the 2007 and 2009 data taking with the thin target, respectively.

Interactions in the target are selected by an anti-coincidence of the incoming beam protons with a small, 2 cm diameter, scintillation counter (S4) placed on the beam trajectory between the two vertex magnets (see Figure 3.8). This interaction trigger is a minimum bias trigger based on the disappearance of the incident beam particle. The measurement of the total inelastic cross section evaluated from the thin target data is presented in Chapter 7.

Material	Length [cm]	Position [cm]	$P_{\mathbf{coll}}$ [%]	$P_{\mathbf{int}}$ [%]	Comment
Ar/CH_4	1.2	-662.7	0.003	0.002	Middle of BPD3
Mylar	0.006	-663.9	0.015	0.010	
Air	20.0	-673.9	0.039	0.027	
Mylar	0.006	-683.9	0.015	0.010	
Vacuum	650	-978.9	0.0	0.0	Vacuum tube
Mylar	0.006	-1303.9	0.015	0.010	
Mylar	2*0.005	-1304.0	0.024	0.016	Counter
Air	136	-1372.0	0.267	0.182	
Scintillator	0.2	-1440	0.360	0.254	Disk of S2
Material between S2 and BPD3 (w/o S2 light guide)			0.738	0.511	Sum

Table 3.5: Material budget in the beam line upstream of the target, starting from the middle of BPD3 and going upstream towards the beginning of S2.

Materials in the Beam Line

The presence of the beam and trigger counters, as well as other materials in the beam line, cause the beam particles to not only interact in the carbon target, but also outside of it. In order to quantify the contribution from these materials, a list of the material budget in the beam line was compiled for the 2007 run, giving the material's length and position with respect to the NA61 coordinate system as well as its nuclear collision and nuclear interaction probability (P_{coll} and P_{int}), respectively (see Tables 3.5 and 3.6). For the calculation of the two latter values the nuclear material properties were taken from [4]. Polystyrene ($[C_6H_5CHCH_2]_n$), commonly used to construct plastic scintillators, was assumed for the scintillation material. From these summary tables one can conclude that the overall nuclear collision and nuclear interaction probability of the material between S2 and S4, aside from the target, roughly amounts to 1.7% and 1.1%, respectively. Here, the largest contribution is coming from the gas in VTPC1. In Chapter 6 these numbers will be compared to the data.

Material	**Length** [cm]	**Position** [cm]	$P_{\mathbf{coll}}$ [%]	$P_{\mathbf{int}}$ [%]	**Comment**
Scintillator	0.5	-211.6	0.922	0.649	Middle of S4
Air	41.2	-232.2	0.081	0.055	
Mylar	0.0125	-252.8	0.030	0.021	End of VTPC1
N_2	2.0	-253.8	0.004	0.003	
Mylar	0.0125	-254.8	0.030	0.021	
Ar/CO_2 (90/10)	250.0	-379.8	0.570	0.364	Middle of VTPC1
Mylar	0.0125	-504.8	0.030	0.021	
N_2	2.0	-505.8	0.004	0.003	
Mylar	0.0125	-506.8	0.030	0.021	Beginning of VTPC1
Air	13.2	-513.4	0.026	0.018	
Mylar	0.002	-520	0.005	0.003	
He	41.6	-540.8	0.013	0.010	He-bag
Mylar	0.002	-561.6	0.005	0.003	
Mylar	0.005	-561.6	0.012	0.008	
He	20.5	-571.6	0.007	0.005	He-tube
Carbon	2	-580.4	6.216	4.289	Target
He	67	-614.8	0.022	0.016	
Mylar	0.005	-648.3	0.012	0.008	
Air	13.2	-655.5	0.026	0.018	
Mylar	0.006	-661.5	0.015	0.010	
Ar/CH4	1.2	-662.66	0.003	0.002	Middle of BPD3
Material between BPD3 and S4 (w/o Target)			0.925	0.610	Sum

Table 3.6: Material budget in the beam line around and downstream of the target, starting from the middle of S4 and going upstream towards the middle of BPD3.

Chapter 4

Collected Data for T2K

The NA61/SHINE experiment was approved at CERN in June 2007 and started its first pilot run in October 2007 [84]. The main aims of this three weeks long run were to setup and test the NA61 apparatus and to take pilot physics data for T2K. The data taking was performed with a 30 GeV proton beam and two different carbon targets, the thin target and the replica target for which about 660k and 230k events were registered, respectively. Upon successful completion of the test run, efforts were joined for the calibration and analysis of the pilot data, so that in summer 2009 first results on pion production and cross section measurements were published [104, 105]. Also in summer 2009, after various detector upgrades were introduced (see Chapter 3), a 3.5 months long run followed. During this run about one month was dedicated to T2K, so that approximately 4.4M events with the thin target and 2.4M with the replica target were recorded. The remaining time of the data taking period was devoted to register a variety of data for the description of cosmic-ray air showers and the study of strongly interacting matter, which are not discussed here. Calibration of the 2009 data is still under investigation, which is why only some results from the 2009 run will be discussed in the course of this thesis. Most studies presented in Chapters 5 and 6 will be based on the 2007 data. In 2010, NA61 was served with another run period, of which about two weeks were again dedicated to T2K. During this time only replica target data were registered ($\sim$10M triggers, of which $\sim$7M are standard pot triggers), which are not topic of discussion in this thesis and therefore not further covered.

Section 4.1 and 4.2 summarize information on the different data sets, which were collected for the thin target data analyses during the 2007 and 2009 runs, respectively. How this data is further processed in order to allow for extracting physics results is addressed in Section 4.3.

Target	Trigger	Magnetic Field	N_{trig}
Thin Target	$S1 \cdot S2 \cdot \overline{V} \cdot C1 \cdot \overline{C2} \cdot \overline{S4}$	$^1/_8$ *std+*	671k
No Target	$S1 \cdot S2 \cdot \overline{V} \cdot C1 \cdot \overline{C2} \cdot \cdot \overline{S4}$	$^1/_8$ *std+*	46k
Thin Target	$S1 \cdot S2 \cdot \overline{V} \cdot C1 \cdot \overline{C2}$	$^1/_8$ *std+*	26k
Thin Target	$S1 \cdot S2 \cdot \overline{V} \cdot C1 \cdot \overline{C2} \cdot S4$	$^1/_8$ *std+*	10k
Thin Target	S1	$^1/_8$ *std+*	12k
No Target	$S1 \cdot S2 \cdot \overline{V}$	*std+*	5k
No Target	$S1 \cdot S2 \cdot \overline{V} \cdot C1 \cdot \overline{C2}$	*std+*	11k
No Target	$S1 \cdot S2 \cdot \overline{V} \cdot C1 \cdot \overline{C2}$	ramp up	10k
No Target	$S1 \cdot S2 \cdot \overline{V}$	ramp down	6k

Table 4.1: Summary table of data collected with a 30 GeV proton beam during the 2007 pilot run. The first part summarizes the runs with standard settings, while the second part those with special settings. In the trigger definition V represents the OR of V0 and V1. For more information on the special runs with trigger on beam see also Table B.1

4.1 2007 Data Sets

The number of triggers (N_{trig}) from the various data sets, that were collected during the pilot run in 2007, are summarized in Table 4.1. They all have a 30 GeV proton beam in common, but differ in target, trigger and magnetic field settings.

For the thin target measurements, here also referred to as target-in (T_{in}) measurements, the standard trigger to select interactions in the target is defined by an anti-coincidence between the triggered beam protons and the S4 counter ($S1 \cdot S2 \cdot \overline{V} \cdot C1 \cdot \overline{C2} \cdot \overline{S4}$) (see Section 3.3). The same trigger condition has also been used for the standard data taking without a target. The so-called target-out (T_{out}) data is, as we will see in Chapter 6, of importance for the cross section evaluation. For both, target-in and -out standard data sets, the magnetic field had been reduced by a factor of eight with respect to its maximum value in order to optimize the geometrical acceptance for particle production in the T2K phase space region (see Section 3.2).

Next to the standard data sets, several target-in and -out runs with different trigger and/or magnetic field conditions have been registered. These special runs are relevant for the systematic studies described in Chapters 5 and 6.

Run Period	Configuration	Trigger	Prescaling
8350 – 8479	`config_standard1`	T1: $S1 \cdot S2 \cdot \overline{V} \cdot \overline{V1'} \cdot C1 \cdot \overline{C2}$	100
		T2: $S1 \cdot S2 \cdot \overline{V} \cdot \overline{V1'} \cdot C1 \cdot \overline{C2} \cdot \overline{S4}$	1
		T3: $S1 \cdot S2 \cdot \overline{V} \cdot \overline{V1'} \cdot C1 \cdot \overline{C2} \cdot S4$	130
		T4: $S1 \cdot S2 \cdot \overline{V} \cdot \overline{V1'} \cdot \overline{S4}$	55
8483 – 8563	`config_T2Kv1`	T1: $S1 \cdot S2 \cdot \overline{V} \cdot \overline{V1'} \cdot C1 \cdot \overline{C2}$	100
		T2: $S1 \cdot S2 \cdot \overline{V} \cdot \overline{V1'} \cdot C1 \cdot \overline{C2} \cdot \overline{S4}$	1
		T3: $S1 \cdot S2 \cdot \overline{V1'} \cdot C1 \cdot \overline{C2} \cdot \overline{S4}$	200
		T4: $S1 \cdot S2 \cdot \overline{V} \cdot \overline{V1'} \cdot \overline{S4}$	100
8577 – 8599	`config_T2Kv2`	T1: $S1 \cdot S2 \cdot \overline{V} \cdot \overline{V1'} \cdot C1 \cdot \overline{C2}$	100
		T2: $S1 \cdot S2 \cdot \overline{V} \cdot \overline{V1'} \cdot C1 \cdot \overline{C2} \cdot \overline{S4}$	1
		T3: $S1 \cdot S2 \cdot \overline{V1'} \cdot C1 \cdot \overline{C2}$	200
		T4: $S1 \cdot S2 \cdot \overline{V} \cdot \overline{V1'}$	100
8600 – 8768	`config_T2Kv3`	T1: $S1 \cdot S2 \cdot \overline{V} \cdot \overline{V1'} \cdot C1 \cdot \overline{C2}$	100
		T2: $S1 \cdot S2 \cdot \overline{V} \cdot \overline{V1'} \cdot C1 \cdot \overline{C2} \cdot \overline{S4}$	1
		T3: $S1 \cdot S2 \cdot \overline{V1'} \cdot C1 \cdot \overline{C2} \cdot \overline{S4}$	200
		T4: $S1 \cdot S2 \cdot \overline{V} \cdot \overline{V1'} \cdot \overline{S4}$	100

Table 4.2: Summary table of trigger configurations used for the data taking in 2009. V represents the OR of V0 and V1.

4.2 2009 Data Sets

During the 2009 data taking it was possible to register data with several trigger conditions at the same time (see Section 3.2). Table 4.2 summarizes the various trigger configurations used for the target-in and -out data taking. Each of these configurations incorporates four different triggers, which have been prescaled by a given factor and recorded simultaneously. Note, that the trigger on beam (T1) and the trigger on interactions (T2), as well as their corresponding prescaling factor, are the same for all of the specified configurations. Next to these standard triggers, the special triggers T3 and T4 were recorded, which had different definitions throughout the data taking. The special triggers are again useful for systematic studies. Furthermore, one can note, that the anti-coincidence of the V1′ counter has been included in all of the configurations because the V1′ signal blocks the S1 signal from giving the start signal for the TOF detectors.

The overall number of recorded triggers for the data taking in 2009 is presented in Table 4.3. Roughly 4.4M triggers of the total thin target data correspond to interaction triggers.

Target	N_{trig}
Thin Target	5598k
No Target	780k

Table 4.3: Summary table of all the triggers collected with a 30 GeV proton beam during the 2009 run. Note, that these numbers give the overall number of registered triggers and have not been verified in detail for their quality yet. Roughly 4.4M interaction triggers for the thin target data have been recorded.

4.3 Event Reconstruction

In order to interpret the recorded data one has to extract from it the essential information such as charge, momentum and specific energy loss of the produced particles. For this purpose a software called reconstruction chain has been developed. It is made up of different client processes and is based on the client/server data manager DSPACK [106].

The reconstruction chain with its main processes and clients is depicted in Figure 4.1. It starts with the MINICLIENTS, which consist of several smaller clients mainly used to extract scaler data from the beam counters (`beam`), to calculate the drift velocities for the different TPCs (`vdrift`) and to reconstruct charge clusters and the beam track from the BPD information (`bpd`). After execution of the MINICLIENTS the cluster reconstruction in the TPCs starts. Charge clusters from the TPC raw data are first localized and then corrected for inhomogenities in the electric field (`edisto`), as well as distortions due to $\vec{E} \times \vec{B}$ effects (`vt_ncalc`). Remaining position deviations between the reconstructed points and tracks is corrected for by the residual corrections (`res_corr`). After space point reconstruction is completed, main tracking starts. It is performed in the framework of a global tracking scheme, which combines the advantages of the different VTPCs and MTPCs. It subsequently runs local tracking in single TPCs and connects the obtained local tracks to points in other TPCs to form global tracks (`mtrac`, `patrec`, `mpat`). More about this procedure can be found in [107]. The momentum of the global tracks is determined from their curvature in the magnetic field with the help of the momentum-reconstruction module `r3d`.

For the proton–carbon data the interaction vertex, called the Main Vertex, is evaluated with the so-called pA option of the `vtx` client. For this option the Main Vertex corresponds to the BPD Vertex[1]. The BPD Vertex has a fixed z-position, which equals to the nominal z-position of the target (-581.41 cm), and a (x, y)-position, which is obtained from the extrapolation of the beam track to the z-position of the target. In case the beam track cannot be reconstructed

[1] In case the BPD Vertex fit fails, for instance if there are less than two clear hits in the BPDs for x- or y-direction, then the Fitted Vertex is used as the Main Vertex. If the Fitted Vertex also fails, then the nominal (x, y, z)-position of the target is used as the Main Vertex.

for one or both of the x/y-coordinates because of missing BPD information, the corresponding x/y-position is set to zero. Next to the BPD Vertex, a Fitted Vertex is evaluated, which has the same (x, y)-position as the BPD Vertex[2], its z-position is however evaluated from a fit on the closest approach of all global tracks. Track momenta are once again determined with the assumption that the tracks stem from the Main Vertex.

After the Main Vertex has been established, the number of potential points is calculated by counting how many pad rows are traversed by a given track (`ppoints`). In case the GTPC has been used during data taking one can furthermore call the `gtpc_track` client to reconstruct the GTPC tracks. With the obtained information on the particle tracks the last step of the tracking procedure is carried out, which removes split tracks. Split tracks are unmatched track segments which belong to the same particle. For this purpose two different clients were developed. While the `domerge` client was optimized for the high-multiplicity environment of heavy ion collisions, for which the GTPC is not employed, the `reform` client was optimized for accurate matching in the lower-multiplicity environment of proton-nucleus and proton-proton collisions, where the GTPC is included. Once further track segments have been matched, their momentum is refitted using vertex constraint and the Main Vertex is redetermined. Information from the tracking is stored in two different data structures called `rtrack` and `track`. While the first one, the raw track structure, holds information on the particles which are independent from the assumption of the Main Vertex, the `track` structure contains the information only valid under the assumption that the particle originates from the Main Vertex. For each `track` there is a link to a `rtrack`.

Once tracking is completed the particle's time of flight and energy loss is determined (`ftof_client`, `tofl_client`, `tofr_client`, `dedxna61`). At the end of the reconstruction chain vertices from V_s^0 or Ξ decays are searched for with the `v0find` and `xi_find` clients. More information on the V_s^0 or Ξ reconstruction can be found in [108, 109].

All information from the reconstructed data is stored on so-called Data Summary Tapes (DSTs) on CASTOR. They can directly be accessed, however are not so handy when analysing many events. To further simplify and speed-up analysis of the data, DSTs are converted to mini-DSTs (mDSTs). These mDSTs are arranged as ROOT trees containing only the information, which is relevant for the various analyses. ROOT [110, 111] is a object oriented analysis framework, that has been developed in the context of NA49. It is based on C++ and uses the C++ interpreter CINT. It contains a variety of classes for visualization and analysis of the data, which have been extended to ROOT61 [112] by adding the T61 classes specific to NA61.

As the reconstruction software, which originates from the NA49 experiment, has been improved and modified since the initiation of the NA61 experiment in order to match the

[2]If the BPD Vertex has failed, the Fitted Vertex is evaluated with the nominal (x, y)-position of the target.

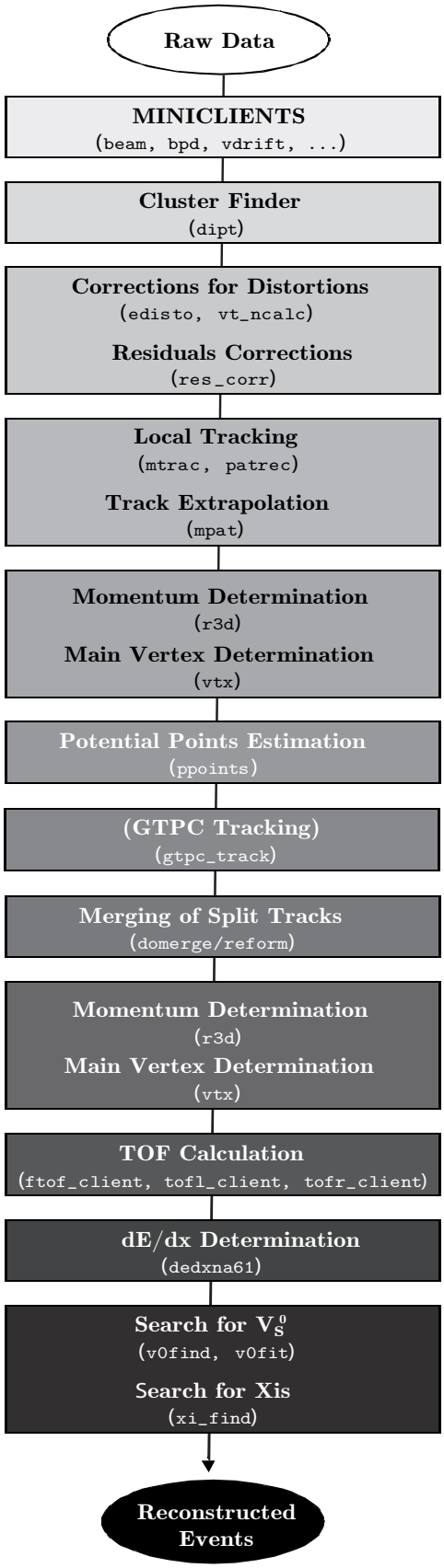

Figure 4.1: Flow chart of the reconstruction chain with its main processes and clients.

Production	Software	GTPC	Comment
07A	v1r2	x	
07F	v1r3	√	
07H	v1r4–1	x	Used for results presented in Summer'09
07I	v1r4–1	√	
07L	v2r0–1b	√	Threshold lowered in BPD client

Table 4.4: Summary of available productions of the 2007 data. Software (pre-)release, whether the GTPC has been included (√) for the reconstruction or not (x) is indicated. For each new production calibration constants have been improved and the data base has been updated.

needs that are particular to NA61, several software (pre-)releases have been conducted. These (pre-)releases include changes in the reconstruction chain clients themselves, but also changes in the ROOT61 and Data Base (DB) structures, for instance additional T61 functions and new calibration constants. With each software (pre-)release the raw data has been reprocessed resulting in a new production of DSTs and mDSTs to be analysed. The most important productions for the 2007 data are summarized in Table 4.4. For each production it is stated which software (pre-)release they are based on and whether the GTPC had been included for the processing or not, i.e. whether the `reform` or the `domerge` client had been used. Thanks to many fixes and updates of the software, clear improvements in the reconstructed data quality have been achieved. The first production showing sufficient quality to extract physics results is the 07H production, on which also the preliminary results from summer 2009 [104, 105] are based on.

An example of a reconstructed thin carbon target event from the 2007 data taking with a 30 GeV proton beam is shown in Figure 4.2. One can observe different track topologies, including long tracks hitting the forward TOF detector.

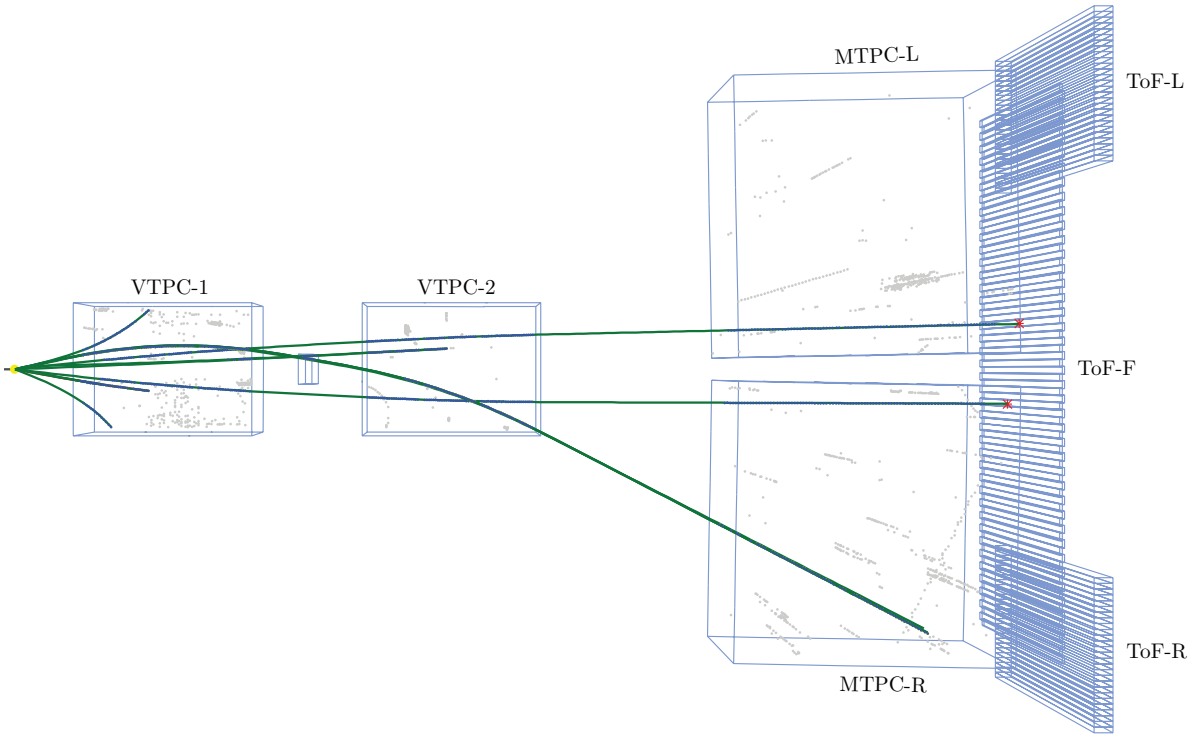

Figure 4.2: Event display of a standard thin carbon target event from the 2007 data taking with a 30 GeV proton beam. Blue points represent measured points in the TPCs, red points hits in the TOF detector, gray points noise clusters, green lines reconstructed tracks and the yellow point the Main Vertex.

Chapter 5

Proton Beam Properties

A wide range of beam studies has been performed in order to precisely define the beam properties during the NA61 data taking for T2K. Besides extracting the beam profile as well as the beam divergence from the standard data sets used to obtain the particle yields, beam momentum and purity have further been studied with the help of data sets of special trigger and/or magnetic field configurations.

Section 5.1 and 5.2 summarize the most essential results from the performed studies on the beam properties of the 2007 and 2009 thin target data taking, respectively.

5.1 Beam Properties in 2007

During 2007 data taking, beam protons were selected by the coincidence $\mathrm{S1} \cdot \mathrm{S2} \cdot \overline{\mathrm{V}} \cdot \mathrm{C1} \cdot \overline{\mathrm{C2}}$, with V representing the OR of the two veto counters V0 and V1, which have a 1 cm diameter hole each, while interactions were selected by an anti-coincidence of the beam particle and the 2 cm diameter counter S4 (see Section 3.3). The beam profiles, as measured by the three Beam Position Detectors (BPDs), are presented in Figure 5.1 for all standard thin target runs. From these distributions one can see that the beam profiles are Gaussian shaped and close to the target (BPD3) well confined by the 1 cm diameter of the veto counters' hole (see also Figure 5.2). That the selected beam profiles are well aligned with the S4 counter has been verified by several studies which were performed with runs of special trigger settings. For details please refer to the presentation of my work [113]. The measured BPD positions are used to reconstruct the beam tracks. The resulting beam divergence from the reconstructed tracks is illustrated in Figure 5.2. Both, measured beam profile and divergence, have been used for the GEANT4 simulations presented in Chapter 7.

Scans of the CEDAR and threshold Cherenkov counters measured 83.7% of pions, 14.7%

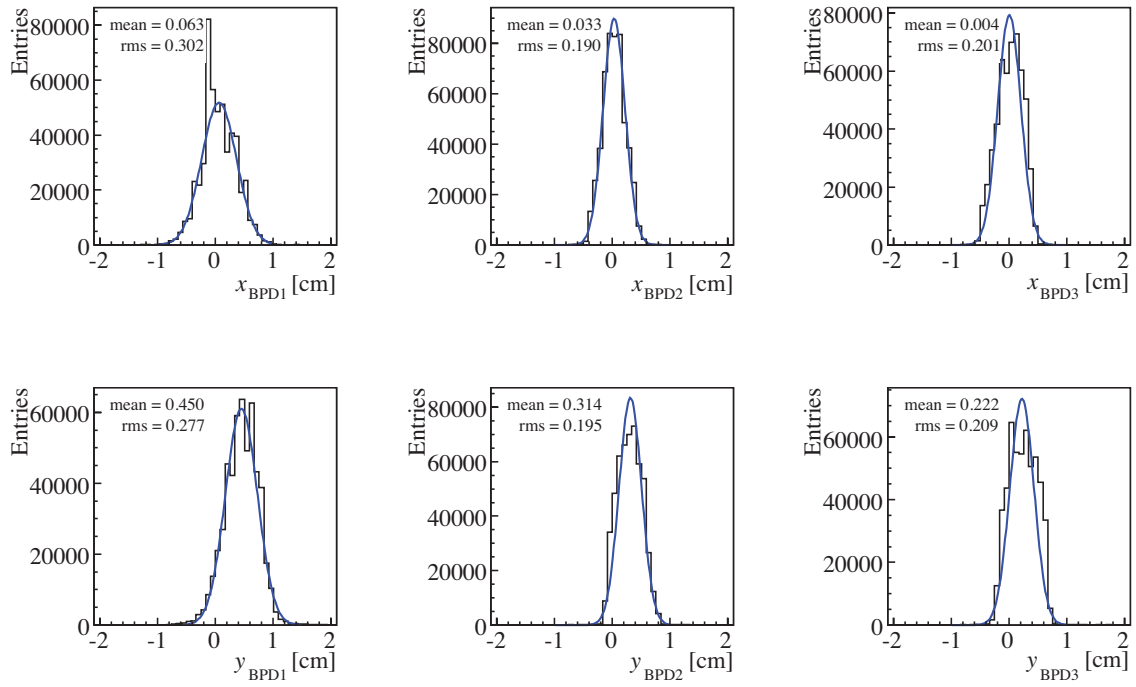

Figure 5.1: The beam $x-$ and $y-$profiles as measured by the three different BPDs. Distributions are based on all 2007 thin target runs of the 07L production, where BPD-Cut (I) and (II) have been applied (see Section 6.3). Note that the veto counters slightly bias the gaussian shape of the beam.

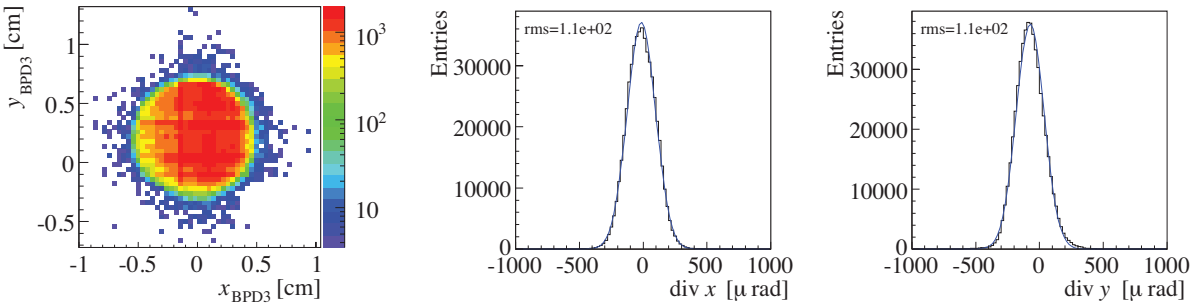

Figure 5.2: The beam spot as measured by BPD3 (left) and the $x-$ and $y-$divergence (middle and right) of the 2007 beam. Distributions are based on all thin target runs of the 07L production, where BPD-Cut (I) and (II) have been applied (see Section 6.3).

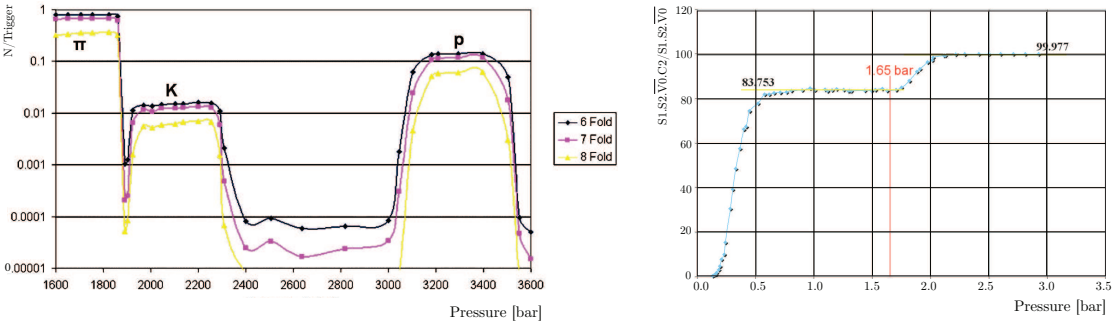

Figure 5.3: *Left:* The CEDAR 6-, 7- and 8-fold coincidence rates (N) of the 8 photomultipliers normalized to the beam intensity (Trigger) as a function of the CEDAR gas pressure. The π-, K- and p-peaks are clearly separated. To select p during data-taking the CEDAR pressure was set to 3.3 bar. *Right:* Coincidence of the threshold Cherenkov counter (C2) and the beam trigger ($S1 \cdot S2 \cdot \overline{V}$) normalized to the beam trigger as a function of C2's gas pressure. The lower plateau shows the region where the counter is efficient for π and K, while above $\approx$1.65 bar it starts to become efficient for also p. During data-taking, where C2 was used in anti-coincidence with the CEDAR and beam triggers ($S1 \cdot S2 \cdot \overline{V} \cdot C1 \cdot \overline{C2}$), the counter's pressure was set to 1.65 bar.

of protons and 1.6% of kaons in the secondary hadron beam (see Figure 5.3). To check the beam purity after the proton identification as well as the beam momentum a special target-out run was taken, where the magnetic field was set to its maximum bending power of 9 Tm over 7m length, so that the beam particles were actually traveling through the TPCs (see Figure 5.4). The measured beam momentum within the TPCs is presented in Figure 5.5. Two different triggers were then used, one with the proton identification, $C1 \cdot \overline{C2}$, in the trigger ($S1 \cdot S2 \cdot \overline{V} \cdot C1 \cdot \overline{C2}$) and the other one without ($S1 \cdot S2 \cdot \overline{V}$). The corresponding energy loss measurements from the TPCs for these runs are shown in Figure 5.6 (in MIP units[1]). The fitting of these spectra was performed in such a way that first the spectrum without the proton identification in the trigger was fitted with three single Gaussians, one for the pions, the protons and the kaons, respectively. For the fits of the pion and proton peaks all parameters – mean value, sigma and height – were left free. The resulting mean dE/dx_{fit} values for these two fits are given in Table 5.1 together with the corresponding values, dE/dx_{par}, calculated using the Bethe-Bloch parameterization [114]. A good agreement between them is observed. To fit the kaon peak, which is not clearly visible in the spectrum, several constraints on the fit parameters had to be used. The mean value of the kaon fit was therefore fixed by the average dE/dx_{par} value of 1.291 MIP which was obtained from the Bethe-Bloch parameterization for 31 GeV/c kaons. Furthermore, the sigma of the kaon fit was restricted by the sigma from the pion and proton fits and the height was restrained in such a way that the proportion of pions, protons and kaons from the fits would match the measured one from the CEDAR and threshold

[1]MIP unit – the amount of the ionization caused by a Minimum Ionizing Particle.

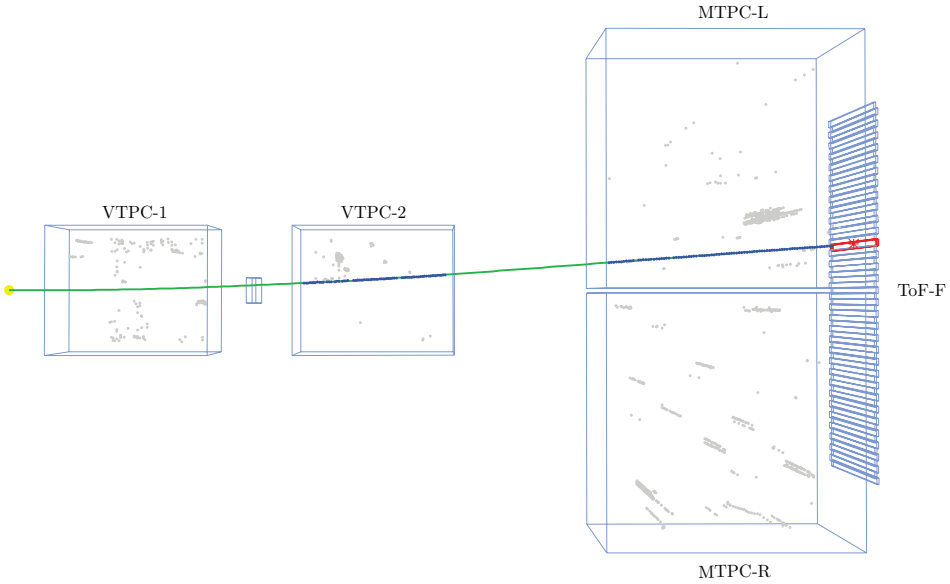

Figure 5.4: Event display of a special target-out run with full magnetic field. Blue points represent measured points in the TPCs, red points hits in the TOF detector, gray points noise clusters, green lines reconstructed tracks and the yellow point the Main Vertex. In VTPC-1 the track has no measured points as it passes the TPC close to the beam axis, which is a region excluded from the TPC's sensitive volume. The GTPC information has furthermore not been taken into account for the processing of this event (see Section 4.3).

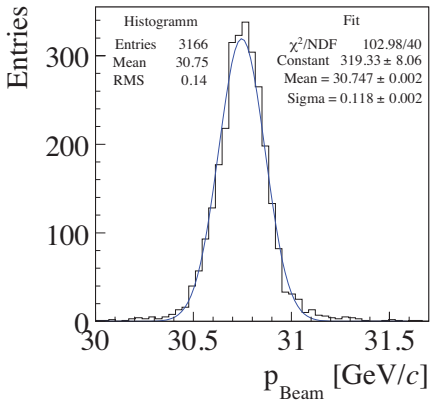

Figure 5.5: The distribution of the proton beam momentum as measured by the NA61/SHINE TPCs in the special runs 5643 and 5645.

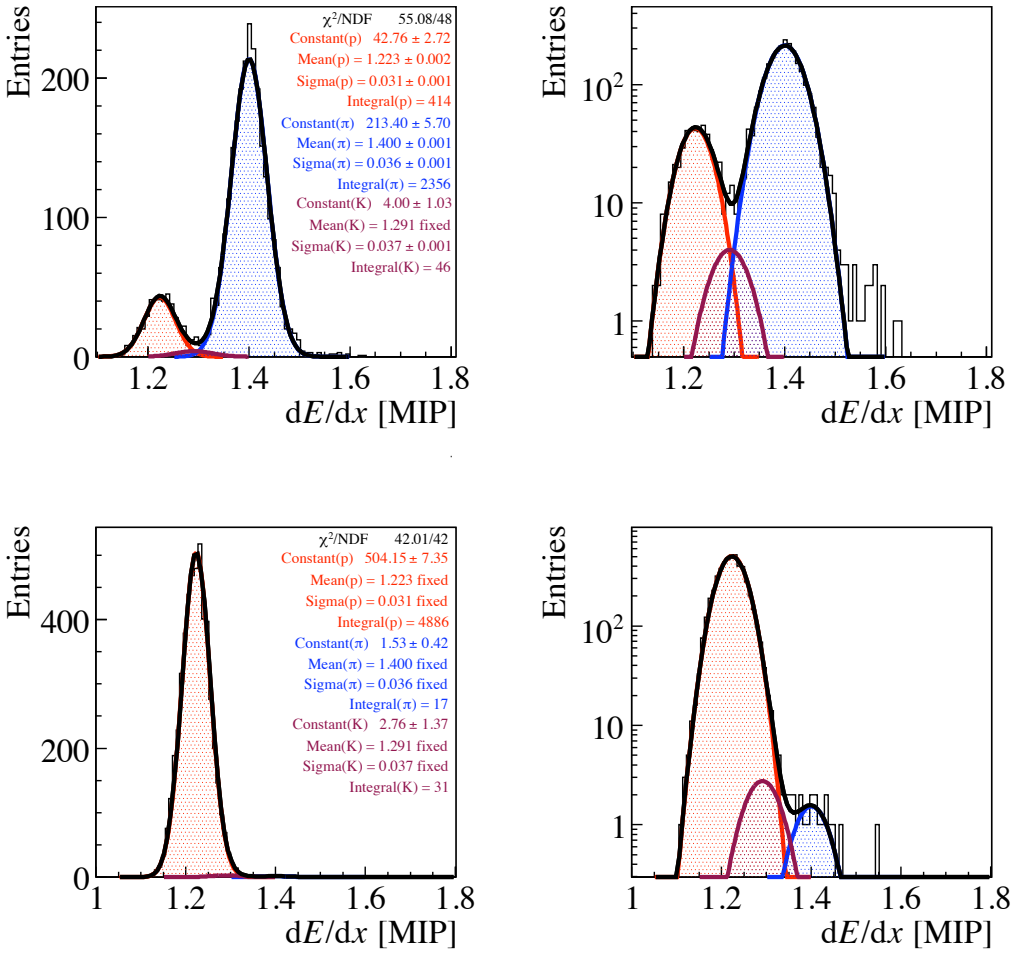

Figure 5.6: The $\mathrm{d}E/\mathrm{d}x$ spectra from special target-out runs with trigger on $\mathrm{S1}\cdot\mathrm{S2}\cdot\overline{\mathrm{V}}$ (upper panel) and $\mathrm{S1}\cdot\mathrm{S2}\cdot\overline{\mathrm{V}}\cdot\mathrm{C1}\cdot\overline{\mathrm{C2}}$ (lower panel). On the left side the plots are shown on a linear scale and on the right on a logarithmic scale. The colored regions correspond to the proton (red), kaon (purple) and pion (blue) signals evaluated from a fit represented by the sum of three Gaussians (black). Note that only events with one positive particle were considered. The tail outside of the fit at higher $\mathrm{d}E/\mathrm{d}x$ values is most probably due to positron contamination.

	$\mathrm{d}E/\mathrm{d}x_{par}$ [MIP]	$\mathrm{d}E/\mathrm{d}x_{fit}$ [MIP]
Protons	1.228	1.223
Pions	1.398	1.400
Kaons	1.291	-

Table 5.1: Mean $\mathrm{d}E/\mathrm{d}x$ values for protons, pions and kaons obtained from the parameterization and the Gauss fits using the spectrum with trigger on $\mathrm{S1} \cdot \mathrm{S2} \cdot \overline{\mathrm{V}}$ (see Figure 5.6).

Cherenkov counter scans. The resulting fits for the pions, protons and kaons are illustrated in the upper panel of Figure 5.6 together with a fit of the whole spectrum represented by the sum of the three Gaussians. The mean values as well as sigmas from the three single Gaussians were then used to fit the spectrum with the proton identification in the trigger. The resulting fits for the pions, protons, kaons and the whole spectrum are illustrated in the lower panel of Figure 5.6. These fits yield a beam composition of $(99.0^{+1.0}_{-2.8})\%$ (90% C.L.) protons, (0.6±0.6)% (90% C.L.) kaons and (0.3±0.2)% (90% C.L.) pions which demonstrates that with the help of the CEDAR and the threshold Cherenkov counters the large pion as well as the kaon contribution in the beam can effectively be reduced to a negligible level.

5.2 Beam Properties in 2009

As the calibration of the 2009 data has not been completed so far, only some results on the 2009 beam properties can be presented here. Results are based on the so called 2009 reference thin target runs, runs 8687 and 8734. These reference runs do not yet include all respective calibration parameters, the alignment of the beam counters has, however, been conducted for them. The resulting beam profiles and beam divergence are shown in Figures 5.7 and 5.8, respectively. Note, that only T2—interaction—triggers, which were selected by the coincidence $\mathrm{S1} \cdot \mathrm{S2} \cdot \overline{\mathrm{V}} \cdot \overline{\mathrm{V1}'} \cdot \mathrm{C1} \cdot \overline{\mathrm{C2}} \cdot \overline{\mathrm{S4}}$, are shown. One can see, that the beam conditions in 2009 were slightly different than the ones in 2007—the 2009 beam is more divergent, but at the same time focused stronger on the target. Differences in the beam conditions cause the observed interaction probabilities for the 2007 and 2009 target-in data to be slightly different from each other, but, as we will see in the following chapter, the real interaction probability coming from the target itself, which is computed from the interaction probabilities seen in both target-in and target-out data sets, is independent of these differences (see Section 6.2).

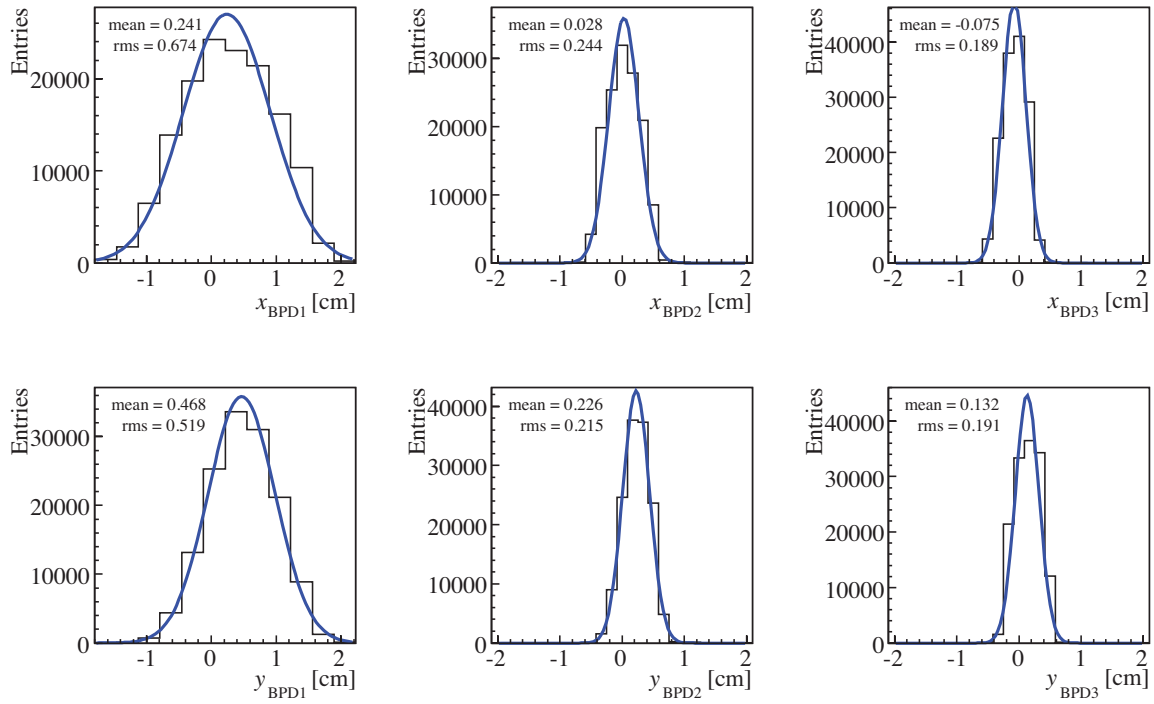

Figure 5.7: The beam $x-$ and $y-$profiles as measured by the three different BPDs. Distributions are based on the 2009 thin target runs 8687 and 8734, where $\overline{\text{BS4}}$ events after BPD-Cut (I) and (II) were selected (see Section 6.3).

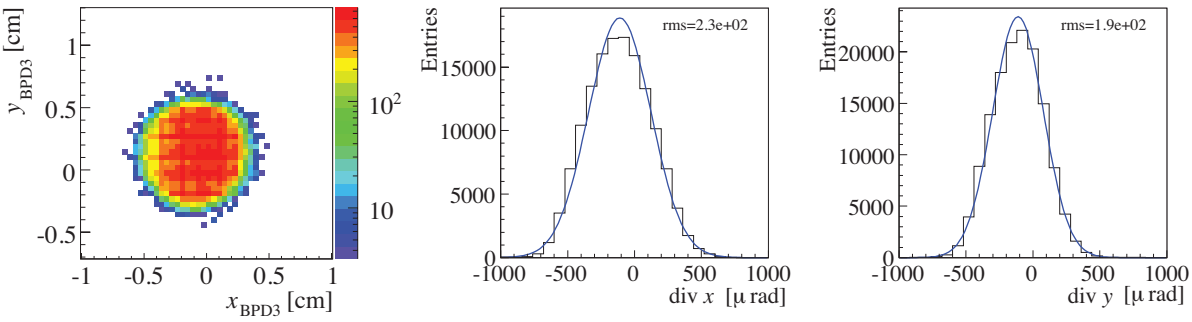

Figure 5.8: The beam spot as measured by BPD3 (left) and the $x-$ and $y-$divergence (middle and right) of the 2009 beam. Distributions are based on the thin target runs 8687 and 8734, where $\overline{\text{BS4}}$ events after BPD-Cut (I) and (II) were selected (see Section 6.3).

Chapter 6

Inclusive Particle Cross Sections

The main motivation and goal of the analysis of the data collected with the thin carbon target is to present the data in terms of mean multiplicities and inclusive particle cross sections in proton–carbon interactions. Therefore, the NA49 approach is followed, which has been used for the determination of the inclusive production of charged pions in proton–proton and proton–carbon collisions at 158 GeV/c beam momentum [115, 95]. In this approach the particle cross sections are evaluated from the data and are then corrected for all experimental biases.

Section 6.1 summarizes the steps of normalization and corrections needed to obtain the inclusive particle cross sections from the measured particle yields, as well as the trigger cross section. The trigger cross section is determined from the observed interaction probabilities and then corrected for distortions as described in Section 6.2. For the evaluation of the measured particle yields it is important to clean up the event sample from events happening outside of the target, so that the background from non-target interactions is reduced and consequently also the systematic uncertainty on the final result. Sections 6.3 and 6.4 describe how suitable event cuts were chosen and how the event selection influences the measured trigger cross section. The final result on the trigger cross section together with its systematic uncertainty is given in Section 6.4. In Section 6.5 it is then discussed how the measured particle yields can be corrected for the remaining background events. Another correction which has been investigated accounts for the bias on the shape of the measured particle spectra due to the trigger condition. It will be presented in Section 6.6. In Chapter 8 it will be demonstrated how the particle yields resulting from different particle identification methods employed in NA61 are finally normalized to the inclusive particle cross sections and mean multiplicities in proton–carbon interactions.

6.1 Scheme for the Cross Section Evaluation

The double differential inclusive[1] cross section for a particle type α is given by

$$\frac{d^2\sigma_\alpha}{dpd\theta}, \quad \alpha = \pi,\, K,\, p \quad , \tag{6.1}$$

where p and θ are laboratory momentum and polar angle of a particle at the proton–carbon interaction point. Experimentally, the double differential inclusive cross section for a fixed target setup can be expressed in the following way

$$\frac{\Delta\sigma_\alpha^{meas}}{\Delta p\Delta\theta} = \frac{1}{nN_{Beam}}\frac{\Delta n_\alpha}{\Delta p\Delta\theta} \quad , \tag{6.2}$$

with

$$n = \rho L N_A/A \quad , \tag{6.3}$$

where N_A denotes the Avogadro constant, ρ the target density, A its atomic number, L its length, N_{Beam} the number of incoming beam particles and Δn_α the number of particles from the target identified in the finite experimental bins Δp and $\Delta\theta$ as particle of type α.

Assuming a bias free[2] trigger the above equation 6.2 can be rewritten as

$$\frac{\Delta\sigma_\alpha^{meas}}{\Delta p\Delta\theta} = \frac{1}{nN_{Beam}}\frac{\Delta n_\alpha}{\Delta p\Delta\theta} = \frac{N_{trig}}{nN_{Beam}N_{trig}}\frac{\Delta n_\alpha}{\Delta p\Delta\theta} \equiv \frac{\sigma_{trig}}{N_{trig}}\frac{\Delta n_\alpha}{\Delta p\Delta\theta} \tag{6.4}$$

where σ_{trig} is called the trigger cross section

$$\sigma_{trig} \equiv \frac{1}{n}\frac{N_{trig}}{N_{beam}} \quad , \tag{6.5}$$

and N_{trig} the number of triggered events coming from the target. Several steps of normalization and correction are needed to make the measured quantity (Eq. 6.4) approach the theoretical one (Eq. 6.1). These will account for

- distortion of the trigger cross section due to events outside of the carbon target, as well as due to the exponential beam attenuation in the target (see Section 6.2),
- bias due to the offline event selection (see Section 6.3),
- distortions of the particle yield due to events outside of the carbon target (see Section 6.5),

[1] In an inclusive measurement of a reaction $A + B \rightarrow \alpha + X$ one measures the reaction product α with no other constraints on the final state, i.e. X can be anything.

[2] Generally, there is an effect due to the trigger condition, which has to be corrected for (see the following sections of this chapter).

- bias on the shape of the particle spectra due to the trigger condition (see Section 6.6).

These corrections will be discussed in turn below.

Further corrections have to be applied which are specific for the analyzed particle types. These are for example described in [124, 127, 123]. They account for

- losses of produced hadrons in registered events due to the geometrical acceptance and the reconstruction efficiency,
- absorption in the detector material,
- re-interactions in the target volume,
- weak decays of pions and kaons,
- feed-down from weak decays of strange particles.

The inclusive cross sections for positively and negatively charged pions resulting from different particle identification methods will finally be presented in Chapter 8.

6.2 Trigger Cross Section Measurement

The trigger cross section (σ_{trig}) is used for the determination of the inclusive particle cross sections as described in Equation 6.4. Assuming no beam attenuation in the target and that all interactions originate from the target it can be calculated according to the following formula

$$\sigma_{trig} = \frac{1}{\rho L N_A / A} \frac{N_{trig}}{N_{beam}} \quad , \tag{6.6}$$

where N_A, ρ, A and L denote, respectively, the Avogadro constant, the target density, its atomic number and its length.

To allow for the fact that some of the triggered events are due to events outside of the carbon target[3] one should evaluate the trigger cross section with the real interaction probability or rather the interaction probability in the target itself (P_{int})

$$\sigma_{trig} = \frac{1}{\rho L N_A / A} \; P_{int} \quad . \tag{6.7}$$

[3] An estimation of the overall material budget in the beam line is presented in Section 3.3.

The interaction probability in the target can be derived from the probabilities obtained for target-in ($P_{T_{in}}$) and target-out operation ($P_{T_{out}}$) which are composed as

$$P_{T_{out}} = P_{up} + P_{down}(1 - P_{up}) \quad , \tag{6.8}$$

$$P_{T_{in}} = P_{up} + P_{int}(1 - P_{up}) + P_{down}(1 - P_{up})(1 - P_{int}) \quad , \tag{6.9}$$

where

$$P_{up} - \text{probability of an interaction in the material upstream of the target,}$$
$$P_{down} - \text{probability of an interaction in the material downstream of the target.}$$

For both, target-in and -out, the reduction of the beam intensity due to interactions upstream of the target has been taken into account and for target-in operation in addition the reduction of the downstream interaction probability due to the target (see Figure 6.1). With equations 6.8 and 6.9 one obtains that the interaction probability in the target can be expressed by the target-in and -out interaction probabilities, $P_{T_{in}}$ and $P_{T_{out}}$, as follows

$$P_{T_{in-out}} \equiv P_{T_{in}} - P_{T_{out}} = P_{int}(1 - P_{up} - P_{down} + P_{up}P_{down}) = P_{int}(1 - P_{T_{out}}) \quad ,$$
$$\Rightarrow P_{int} \approx P_{T_{in-out}}(1 + P_{T_{out}}) \quad . \tag{6.10}$$

The target-in and -out interaction probabilities can be calculated from the number of corresponding triggered events ($N_{trig}^{T_{in}}$ and $N_{trig}^{T_{out}}$) with standard trigger condition $\mathrm{S1}\cdot\mathrm{S2}\cdot\overline{\mathrm{V}}\cdot\mathrm{C1}\cdot\overline{\mathrm{C2}}\cdot\overline{\mathrm{S4}}$ as well as the corresponding number of gated[4] beam particles ($N_{Beam}^{T_{in}}$ and $N_{Beam}^{T_{out}}$) defined by $\mathrm{S1}\cdot\mathrm{S2}\cdot\overline{\mathrm{V}}\cdot\mathrm{C1}\cdot\overline{\mathrm{C2}}$ (see Chapter 3)

$$P_{T_{in}} = \left(\frac{N_{trig}}{N_{beam}}\right)^{T_{in}} \text{ and } \quad P_{T_{out}} = \left(\frac{N_{trig}}{N_{beam}}\right)^{T_{out}} \quad . \tag{6.11}$$

Next to the correction for events outside of the target one has to correct the trigger cross section for the exponential beam attenuation in the target. This can be carried out by evaluating the trigger cross section with the help of the effective target length (L_{eff}) instead of the real target length (L)

$$\sigma_{trig} = \frac{1}{\rho L_{eff} N_A / A}\, P_{int} \quad . \tag{6.12}$$

The effective target length can be computed according to

$$L_{eff} = \lambda_{abs}(1 - e^{-L/\lambda_{abs}}) \quad , \tag{6.13}$$

[4]The number of gated beam particles corresponds to the number of beam particles counted during data acquisition lifetime, which fulfilled the trigger conditions. The number of ungated beam particles is the complement to it.

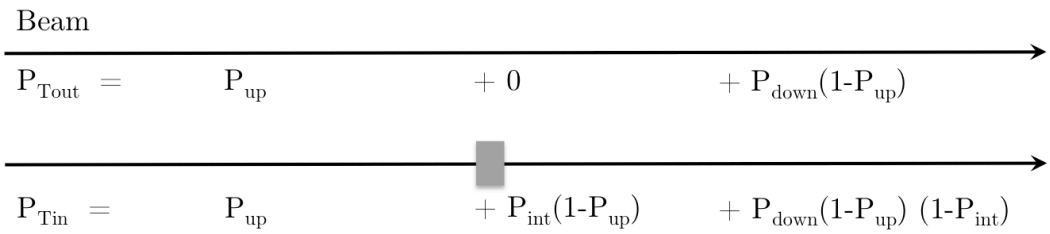

Figure 6.1: Sketch of the composition of interaction probabilities for the target-out (above) and -in (below) operation. P_{up} refers to the probability of an interaction in the material upstream of the target and P_{down} to one downstream of the target.

with the absorption length

$$\lambda_{abs} = \frac{A}{\rho N_A \sigma_{trig}} \quad . \tag{6.14}$$

The calculation of the trigger cross section is then carried out in an iterative procedure. One first estimates the trigger cross section with the real length of the target, then uses the obtained value to compute the effective target length, with which one determines a corrected value of the trigger cross section. One repeats these steps with the preliminary values for the effective length and the trigger cross section until they have converged.

During the 2007 run approximately 671k triggered events for inserted target operation (T_{in}) and 46k for target-out operation (T_{out}) were registered (see Chapter 4). Analysis of this data[5] results in the interaction probabilities for target-in of $(7.104 \pm 0.009)\%$ and for target-out of $(1.719 \pm 0.008)\%$. The interaction probabilities have also been studied on a run by run basis as presented in Figure 6.2. A detailed list of all the analyzed runs is given in Appendix A. For all the runs, the observed deviations are within statistical errors except for run 5601, which is a short run stopped on purpose due to unstable beam conditions. The instability of the beam in run 5601 is manifest in Figure 6.3, where the BPD-positions as well as the mean BPD-positions for this run are compared to the ones from all other standard target-in runs. One can note that in this run significantly more beam particles missed the BPDs and that also the mean BPD positions were systematically shifted. It was therefore decided to remove this run from the physics analyses.

The 2007 interaction probabilities for target-in and -out operation lead to a real interaction probability of $(5.477 \pm 0.012)\%$ due to the target, resulting in an effective target length of 1.9447 cm and a trigger cross section of (305.4 ± 0.7)mb. Note, that only statistical errors are given here. A summary of all the numbers is given in Table 6.1. In the remaining part of

[5]Here, numbers are based on the 07L production of the reconstructed data. Numbers based on the 07H production are given in the Appendix A. Differences between the productions lie within the statistical uncertainties.

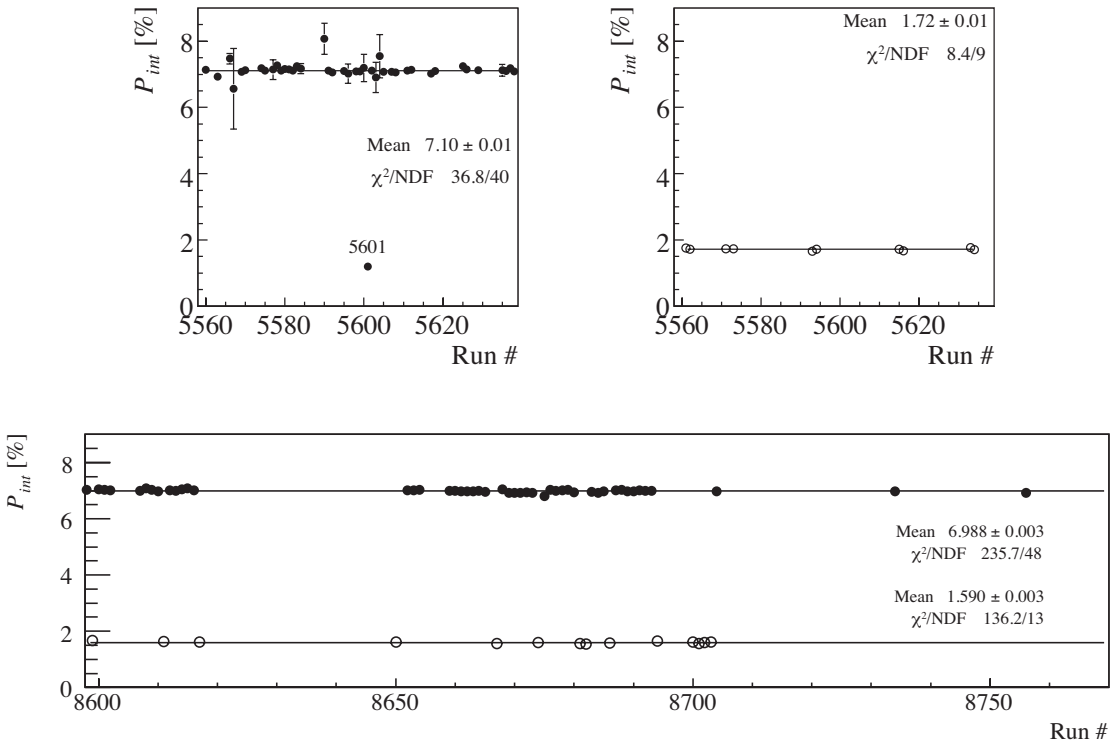

Figure 6.2: Interaction probability with the respective statistical uncertainty as a function of the run number for inserted target (full circles) and target-out operation (open circles) for 2007 (above) and 2009 data (below). Note, that run 5601 has not been taken into account for the fit. The 2009 data is based on the scaler information from the trigger monitor files.

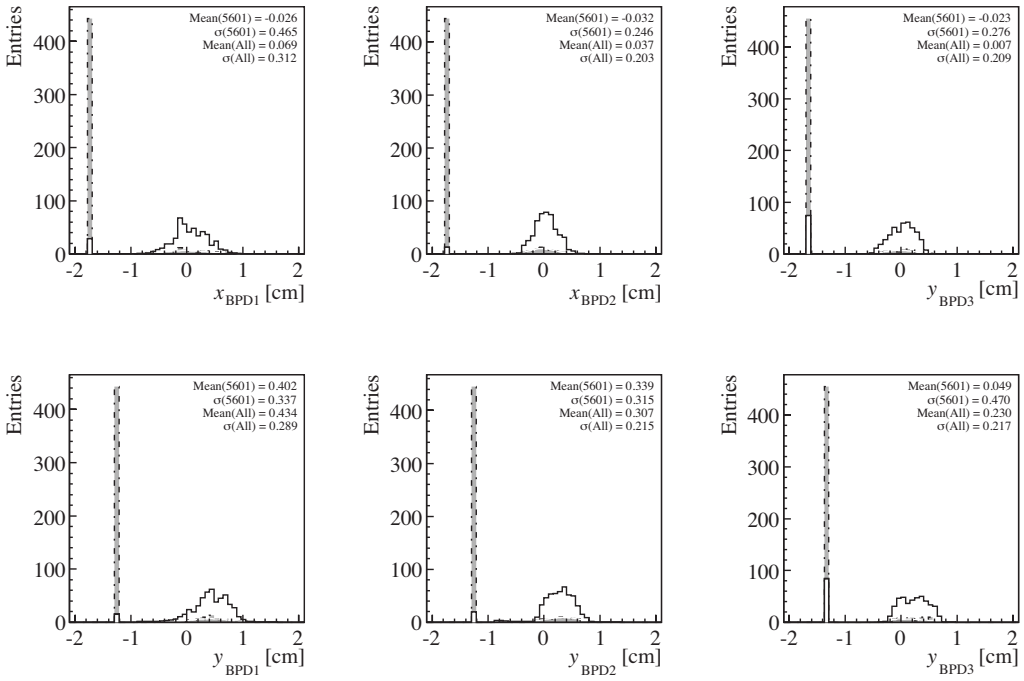

Figure 6.3: $x-$ and $y-$positions of the beam particles for the 3 different BPDs for run 5601 (dashed line, grey filling) and all other target-in runs (solid line) with interaction trigger. The outliers correspond to the cases where no signal in a given BPD plane has been measured. Mean positions and σ were obtained from a Gaussian fit in a region excluding the outliers.

	2007	**2009**
P_{Tin}[%]	7.104±0.009	6.988±0.003
P_{Tout}[%]	1.719±0.008	1.590±0.003
P_{int}[%]	5.477±0.012	5.484±0.004
L [cm]	2	2
L_{eff} [cm]	1.9447	1.9447
ρ [g/cm^3]	1.8395±0.0010	1.8395±0.0010
N_A [mol^{-1}]	6.022e23	6.022e23
A [g/mol]	12.011	12.011
σ_{trig} [mb]	305.4±0.7	305.8±0.3

Table 6.1: Summary table of values used for the evaluation of the trigger cross section before the offline event selection. Only statistical errors are given. Numbers are based on the 07L production. Recalculation of σ_{trig} after target-out background reduction and systematic error evaluation are presented in Section 6.4.

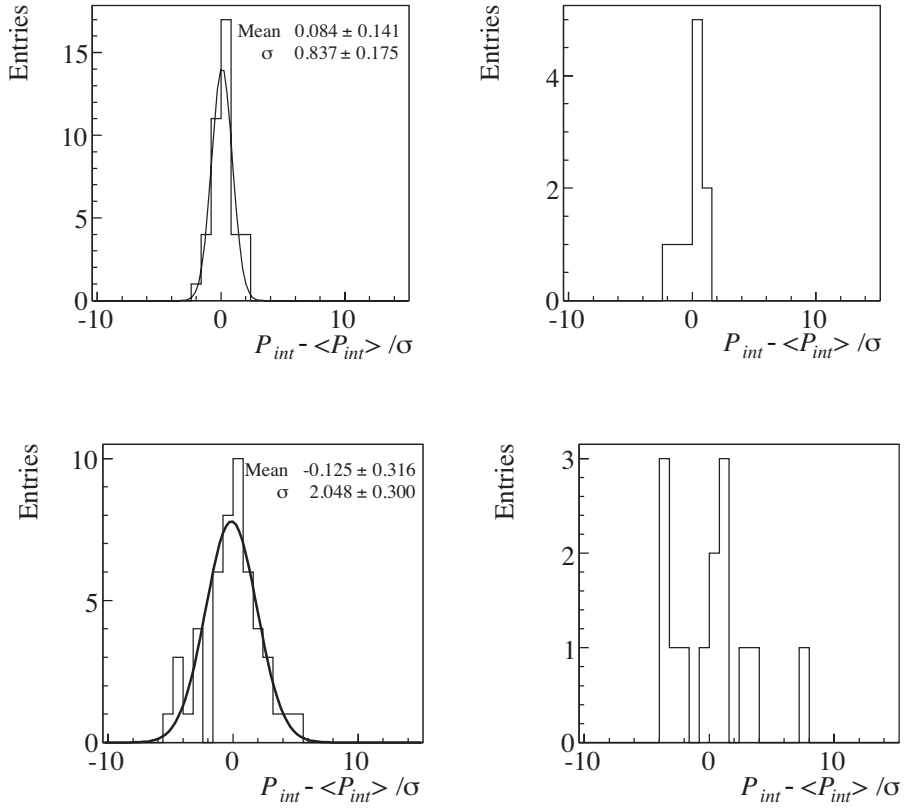

Figure 6.4: Normalized residuals of interaction probabilities for inserted target (left) and target-out operation (right) for all runs from 2007 (above) and 2009 (below).

this section studies which have been conducted to evaluate the origin of the high interaction probability outside of the target are described. Suitable event cuts are used to reduce this target-out background and to clean up the event sample (see Section 6.3). The trigger cross section is then recalculated after the event selection in Section 6.4. Also systematic errors on the trigger cross section will be presented there.

The interaction probabilities measured during the 2007 run can be cross-checked with the ones observed during the 2009 data taking. For that purpose, the scaler information[6] from the 2009 trigger monitor files has been analyzed (see Section 3.2). The corresponding results on the interaction probabilities are shown in Figure 6.2 as a function of the run number. The overall interaction probabilities for target-in and -out operation yield $(6.988 \pm 0.003)\%$ and $(1.590 \pm 0.003)\%$, respectively. Note, that only statistical errors are given here. Compared to the 2007 measurements, the ones from 2009 are dominated by systematic uncertainties. This manifests itself in the much larger χ^2/NDF values from the fit as well as in the spread of

[6]Here, numbers are based on the free running scalers (scaler unit 4).

	Hit in			Events	wrt all	Comment
	BPD1	**BPD2**	**BPD3**		**45725 Evts**	
Hits < 6	not defined			25979	57%	Tracks not measured in $\geq$1 plane
Cut-123	$\surd$	$\surd$	$\surd$	19746	43%	Non-broken tracks
Cut-12	$\surd$	$\surd$	x	19119	42%	Broken tracks
Cut-12 and $y < -0.2$ cm	$\surd$	$\surd$	x	6288	14% (33% wrt all Broken tracks)	Broken tracks in low y-region

Table 6.2: Event reduction table for the cut studies performed with the target-out data sample. $\surd$: hit in both BPD planes. x: no hit in both BPD planes. Numbers are based on the 07L production.

the normalized residuals of the interaction probabilities, which are shown in Figure 6.4. The interaction probabilities for target-in and -out operation lead to a real interaction probability of $(5.484 \pm 0.004)\%$, an effective target length of 1.9447 cm and a trigger cross section of (305.8 ± 0.3)mb, which is in excellent agreement with the value determined from the 2007 data.

Target-Out Interactions

Various studies have been conducted with the 2007 data in order to clarify where the high interaction probability of $(1.719 \pm 0.008)\%$ for target-out events, causing a fake trigger probability $\varepsilon = P_{T_{out}}/P_{T_{in}}$ of about 24%, originates from. These studies involve, amongst others, the estimation of the material budget within the beam line, which is presented in Section 3.3. It shows that the material between S2 and S4, aside from the target, roughly leads to an overall nuclear interaction probability of 1.1% and a nuclear collision probability of 1.7%. Since not only the inelastic and quasi-elastic scattering, but also the coherent elastic scattering partially[7] contributes to the interaction probability, one can conclude that the interaction probability for target-out events due to scattering within the beam line should roughly lie somewhere between 1.1% and 1.7%. Note, that the influence of the veto counters, which would lower the observed interaction probability, is not taken into account here. The estimation of the inefficiency of the S4 counter will be discussed at the end of this subsection.

The contribution from the material between S2 and BPD3 (see Table 3.5) can be cross-checked with the help of the measurements from the beam position detectors (BPDs). The idea

[7]It contributes only if the scattering angle is so large that the scattered beam particle misses S4.

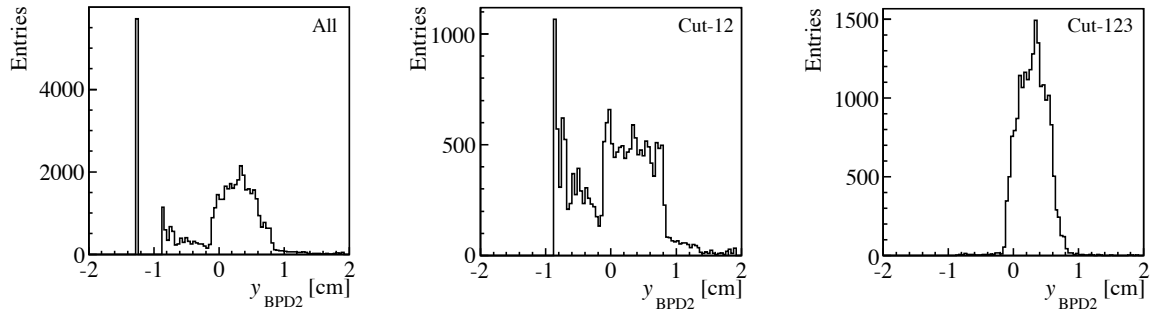

Figure 6.5: $y-$positions of the beam particles at BPD2 with interaction trigger for all events (left), events which passed Cut-12 (middle) and Cut-123 (right) for target-out operation with interaction trigger.

is, that if the triggered beam particle interacts within the beam line between S2 and BPD3, one should have hits in both planes of BPD1 and BPD2, but none in BPD3. This is of course only partly true, since some of the beam particles interacting in the beam line might still hit BPD3, thus would not be counted as interaction here, while others might have been vetoed by one of the veto counters. Studies show, that for the target-out data approximately 57% of the beam particles have not been detected in at least one plane of the three beam position detectors (see Table 6.2). Here the largest contribution, namely ∼42% of all beam particles (see Table 6.2), comes from tracks which did not have a hit in both planes of the last BPD, BPD3. A possible reason for this, besides scattering in the beam line, could be a very high inefficiency of BPD3. The contribution from the inefficiency of BPD3 has therefore been evaluated from runs taken with special trigger on beam in coincidence with S4, for which the beam tracks have surely passed through all three BPDs. It was found to be of the order of 3%, which shows that the large contribution of events with no hit in BPD3 is not mainly due to the inefficiency of the counter, but rather due to broken tracks between S2 and BPD3 which are not reaching BPD3. In order to analyze these broken beam tracks in more detail, cut studies have been performed using two different event cuts. The first cut, the so-called Cut-12, selects only those events, where the beam track had a hit in both planes of BPD1 and -2 but no hit in BPD3, i.e. those events where the beam track was broken. The other cut, Cut-123, retains only those triggered events where the beam track had a hit in both planes of all three BPDs. If one then looks at the corresponding BPD profiles, one can note a dependence of the shape of the BPD2 y-distributions on the cuts (see Figure 6.5). Whereas the distributions look reasonable for tracks hitting all three BPDs, the one for broken beam tracks show a strange enhancement in the lower y-region ($y < -0.2$ cm). This enhancement of ∼33% could be explained by beam tracks interacting in the light guide of S2. For future data taking one could therefore try to improve the trigger performance by using a different S2 counter with an air-lightguide. To summarize, one can say that ∼42% of the fake triggers is due to these broken beam tracks between S2 and

Material	$\lambda_{\mathbf{coll}}$ [%]	$\lambda_{\mathbf{int}}$ [%]	$\lambda_{\mathbf{data}}$ [%]
Material between S2 and BPD3	0.74	0.51	0.72
Material between BPD3 and S4	0.93	0.61	-

Table 6.3: Rough estimation of contributions to the fake trigger probability.

BPD3 and that probably ∼33% out of the 42% are due to interactions in the light guide of S2 (see Table 6.2). If one compares the measured fake trigger contribution from the material between S2 and BPD3 to the one determined by summing up the material budget in the beam line, one observes a quite good agreement between both (see Table 6.3).

Another possible contribution to the fake trigger probability, which has been studied, is the inefficiency of the S4 counter. It has been quantified with the help of the GTPC which is located directly behind S4. By looking at the first point distribution of tracks going through the GTPC one can see the image of S4 (see Figure 6.6). If one then counts the number of tracks within this image and normalizes it to the number of gated beam particles one finds the S4 inefficiency to be less than 0.2% for the whole thin target data sample. Note, that no event cuts (e.g. WFA[8]-Cut) have been applied here, due to the fact that one cannot apply them on the gated beam particles. Altogether, one can say that the observed fake triggers can mostly be explained by scattering within the beam line before and after the target and that a contribution from the inefficiency of the S4 counter is negligible.

One should note, that these fake triggers are not a problem when determining the trigger cross section, as one automatically corrects for them when using the real interaction probability (P_{int}), which is calculated from both probabilities obtained with and without the target (see Eq. 6.11). However, to reduce corrections needed for the target-out contribution and to minimize the systematic error on the final result, suitable event cuts are chosen, which lower the observed fake trigger probability.

6.3 Offline Event Selection

From the interaction probability of (7.104±0.009)% for inserted target operation and of (1.719± 0.008)% for target-out operation one can conclude that about 24% of the recorded events do not originate from the carbon target. To clean up the event sample and to reduce the target-

[8]The Wave Form Analyzer (WFA) collects information from the beam counters to determine the number of beam particles that traverse the detector during the TPC readout.

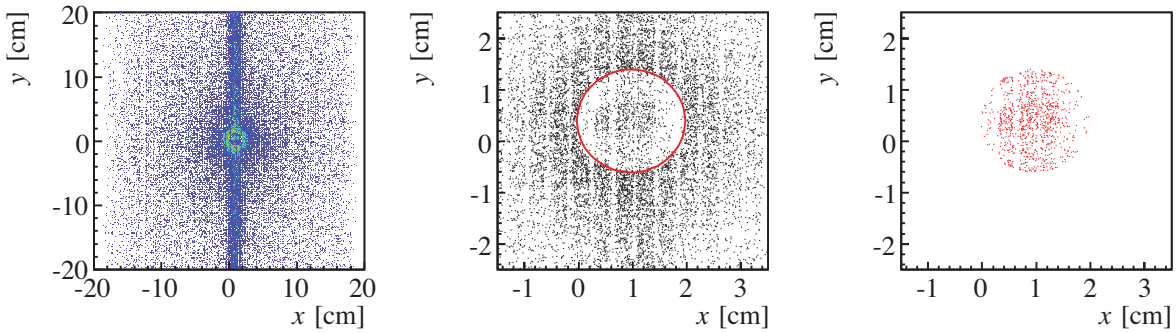

Figure 6.6: *Left and Middle:* x-$y-$position of the first points of tracks of run 5368, which are going through the GTPC for all thin target runs. Note, that the band comes from additional beam tracks, which traverse the TPC during readout time. The circle illustrates the edge of S4, which is centered to $x = +0.97$ cm (left, Jura) and $y = +0.395$ cm (up). *Right:* x-$y-$position of the first points of tracks which are going through S4 (including all additional beam tracks, which traverse the TPCs during readout).

out background, and consequently the systematic error on the final result, suitable event cuts can be chosen. In order not to create any bias due to the offline event selection, the event cuts should fulfill one of the requirements below

- either the rejection from the real target interactions is random, i.e. the rejection does not depend on topology, reconstruction efficiency, etc,
- or the cuts reject no target events at all.

The second case can be checked by ensuring that the accepted fraction of target only events is not affected by the cut. According to [100], this fraction of events happening only in the carbon target (N^C_{trig}) can be calculated from the accepted fraction of the target-in and -out event sample according to Equation 6.15, which can be derived by looking at the fraction of target-in and -out interaction probabilities ($P_{T_{in}}$ and $P_{T_{out}}$) before and after the cut

$$\frac{P'_C}{P_C} = \frac{P'_{T_{in}} - P'_{T_{out}}}{P_{T_{in}} - P_{T_{out}}} \quad .$$

Here, the prime denotes the given quantity after the cut. Note, that in this ansatz higher order corrections to the real interaction probability, that are coming from the reduction of the beam intensity in the material along its trajectory, as discussed in Section 6.2, have been neglected ($P_C \approx P_{int}$). With $\varepsilon = P_{T_{out}}/P_{T_{in}}$ it follows that

$$\frac{P'_C}{P_C} = \frac{1}{1-\varepsilon}\left(\frac{P'_{T_{in}}}{P_{T_{in}}} - \varepsilon\frac{P'_{T_{out}}}{P_{T_{out}}}\right) \quad ,$$

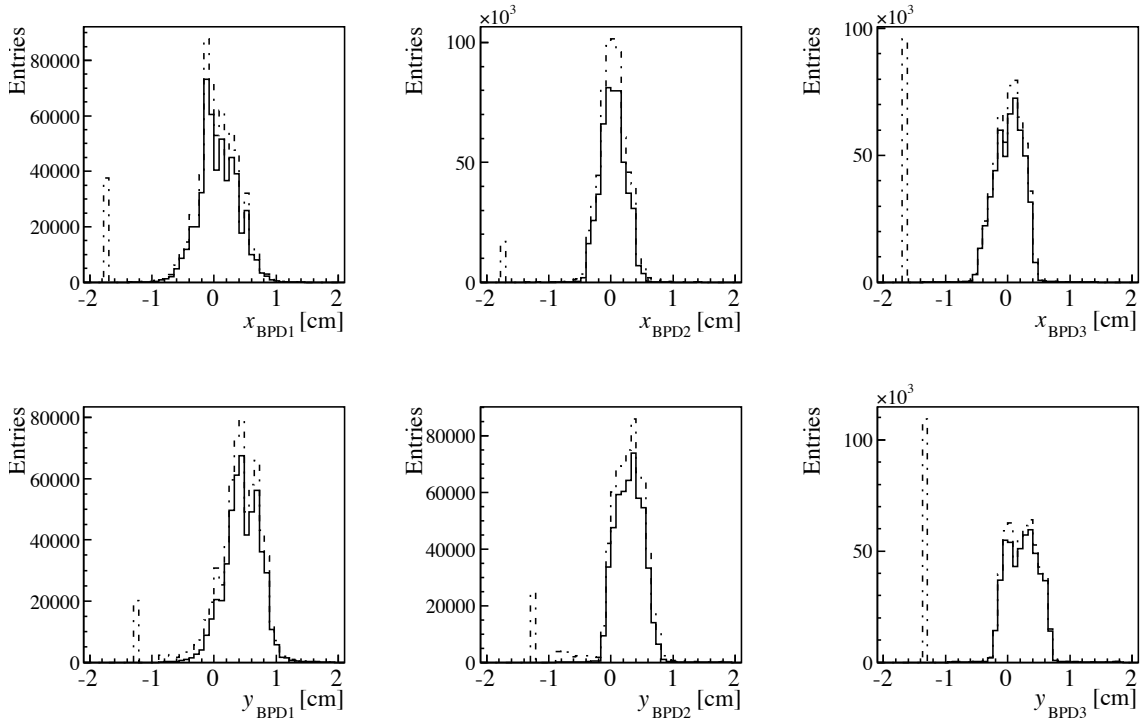

Figure 6.7: $x-$ and $y-$positions of the beam particles for the three different BPDs with interaction trigger before (dashed line) and after (solid line) BPD Cut (I).

and with $P = N_{trig}/N_{beam}$ that

$$\frac{N'^{C}_{trig}}{N^{C}_{trig}}\frac{N^{C}_{beam}}{N'^{C}_{beam}} = \frac{1}{1-\varepsilon}\left(\frac{N'^{T_{in}}_{trig}}{N^{T_{in}}_{trig}}\frac{N^{T_{in}}_{beam}}{N'^{T_{in}}_{beam}} - \varepsilon\frac{N'^{T_{out}}_{trig}}{N^{T_{out}}_{trig}}\frac{N^{T_{out}}_{beam}}{N'^{T_{out}}_{beam}}\right) \quad .$$

Using the fact that the reduction of the number of beam particles by the cut does not depend on whether a target was present or not

$$\frac{N'^{C}_{beam}}{N^{C}_{beam}} = \frac{N'^{T_{in}}_{beam}}{N^{T_{in}}_{beam}} = \frac{N'^{T_{out}}_{beam}}{N^{T_{out}}_{beam}} \quad ,$$

the fraction of events happening only in the carbon target can be expressed by

$$\frac{N'^{C}_{trig}}{N^{C}_{trig}} = \frac{1}{1-\varepsilon}\left(\frac{N'^{T_{in}}_{trig}}{N^{T_{in}}_{trig}} - \varepsilon\frac{N'^{T_{out}}_{trig}}{N^{T_{out}}_{trig}}\right) \quad . \tag{6.15}$$

A cut is bias free if the accepted number of target events is the same before and after the cut, so that their ratio has to be equal to one.

		Event Numbers		$\epsilon =$
		T_{in}	T_{out}	$P_{T_{out}}/P_{T_{in}}$
07H	Before Cuts	671398 (100%)	45749 (100%)	0.242±0.001
	BPD-Cut (I)	518590 (77%)	18044 (39%)	0.124±0.001
	BPD-Cut (II)	398634 (59%)	13582 (30%)	0.121±0.001
	BPD-Cut (I+II)	373266 (56%)	12651 (28%)	0.120±0.002
07L	Before Cuts	666874 (100%)	45725 (100%)	0.242±0.001
	BPD-Cut (I)	565498 (85%)	19746 (43%)	0.123±0.001
	BPD-Cut (II)	526036 (79%)	17616 (39%)	0.118±0.001
	BPD-Cut (I+II)	521226 (78%)	17385 (38%)	0.118±0.001

Table 6.4: Influence of BPD-Cut (I), (II) and (I+II). Numbers are given for the 07H and 07L production.

As mentioned before, most of the observed out-of-target interactions can be explained by beam particles which scatter within the beam line and do not hit S4. Therefore, cuts on the measured beam position were found to be effective in significantly reducing these fake triggers. With the help of the so-called BPD Cut (I)[9] one can ensure, that the $x-$ and $y-$direction of the beam particles has been measured by all three beam position detectors. It significantly reduces the target-out to target-in ratio ($\epsilon = P_{T_{out}}/P_{T_{in}}$) from 24.2% to 12.3%, while retaining 85% of target-in, 43% of target-out and about 98% of carbon target events. Note, that these numbers are based on the 07L production, for which the influence of the BPD cuts is different than for the 07H production and earlier ones, as the threshold settings have been changed in the BPD reconstruction client (see Table 4.4). Corresponding values for the 07H production can be found in Table 6.4. BPD Cut (I) (see Figure 6.7) significantly reduces the fake trigger probability, however it does not guarantee sufficient event quality for physics analyses, due to the fact that it retains some events where the BPD-vertex reconstruction failed for either one or both $x-$ and $y-$coordinates. The quality of the BPD-vertex is important, as its position is used to determine the momentum of produced particles. Thus, in order to not only minimize the fake trigger probability, but also the bias on the momentum determination, BPD Cut (II)[10] has been found more efficient. BPD Cut (II) ensures that the BPD-vertex reconstruction has been successful and also that both BPD3 $x-$ and $y-$positions were taken into account in the BPD-vertex fit, through which the resolution of the vertex reconstruction is improved. If one furthermore wants to ensure that also BPD1 and BPD2 $x-$ and $y-$positions were reconstructed, one can combine BPD Cut (II) with BPD Cut (I). The combination of both

[9] BPD Cut (I) can be implemented in the analyses by using `if(bpd_vtx→iflag&2)continue;`, with `bpd_vtx = (T49VertexRoot *)event→GetBPDVertex()`.

[10] BPD Cut (I) can be implemented in the analyses by using `if((bpd_vtx→iflag&1≪10) || (bpd_vtx→iflag&1≪6) || (bpd_vtx→iflag&1))continue;`

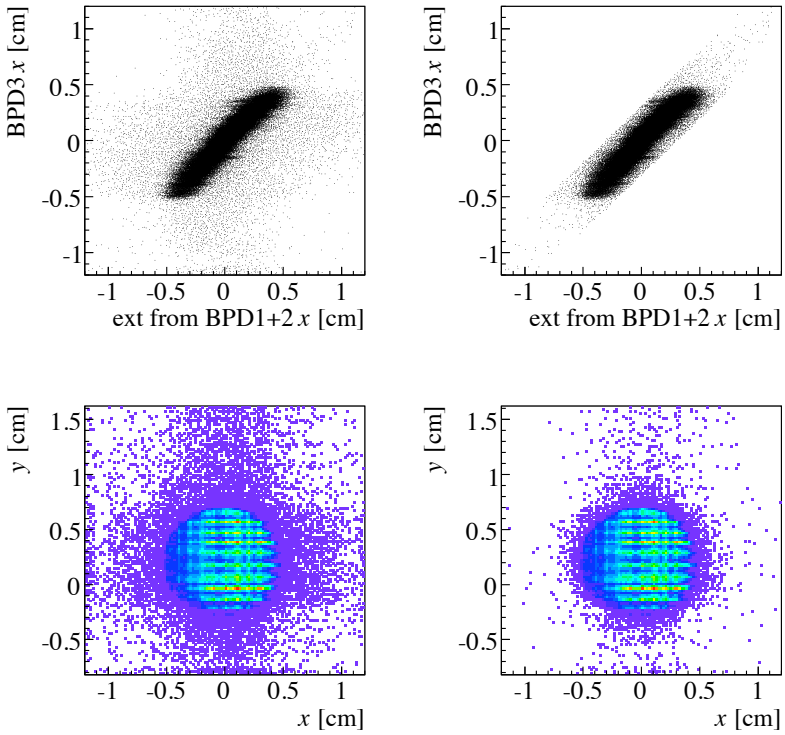

Figure 6.8: Extrapolated BPD3 x-position using BPD1 and BPD2 information versus measured BPD3 x-position (upper panel) as well as the measured beam profile at BPD3 (lower panel) before (left) and after (right) a cut of 0.3 cm for both directions.

cuts assures successful reconstruction of all the beam positions, sufficient BPD-vertex quality and satisfactory reduction of the fake trigger probability. Since no other event cuts have been found to further improve the event selection (see the following subsection), it is suggested to use BPD Cut (I+II) for physics analyses.

When applying BPD cuts, further corrections for the offline event selection are not needed, since they randomly reject real target interactions and thus fulfill the requirements of a bias-free cut.

Additional Investigated Event Cuts

Besides the event cuts presented up to now, several other cuts have been tested. However, due to the fact that they did not significantly improve the event selection, it has not been proposed to apply them for physics analyses. Two of them are also BPD Cuts. One is a circular cut on the reconstructed BPD vertex and the other one ensures that the extrapolation from BPD1 and BPD2 to BPD3 coincides with the measured beam position at BPD3, as demonstrated in

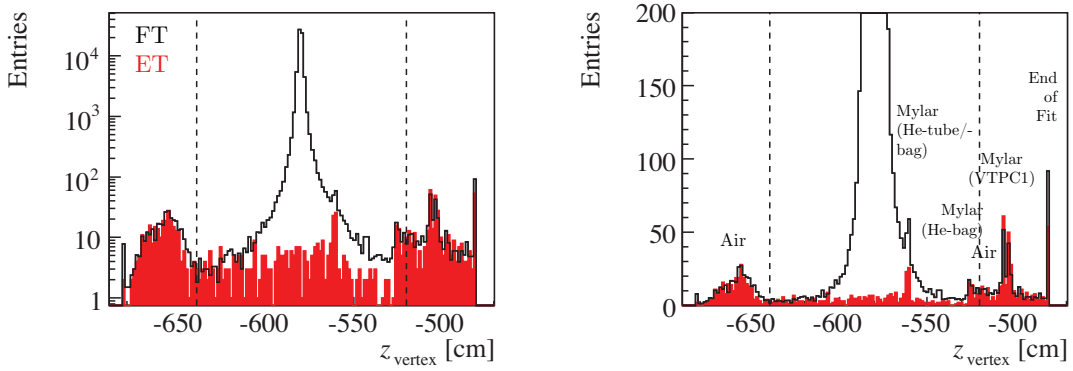

Figure 6.9: Normalized vertex distributions from target-in (black) and -out (red) on a logarithmic (left) and linear (right) scale with at least two selected tracks. The dashed lines indicate a z_{Vertex} Cut within the range of $[-640, 520]$cm. The contributions from the different materials in the beamline can clearly be seen (see Section 3.3).

Figure 6.8. In addition to BPD Cut (I) and/or (II) they however did not significantly reduce the fake trigger probability.

Next to the BPD cuts, also a track multiplicity and event topology dependent cut on the $z-$position of the reconstructed interaction vertex, z_{Vertex} Cut, has been investigated. Since the main vertex reconstruction strongly depends on the event configuration, a bias free z_{Vertex} Cut should be chosen in such a way that it does not reject any real target events. This can be guaranteed by applying the cut only to those events, where the main vertex reconstruction was reliable, while accepting all other events without the cut. Events with a reliable main vertex reconstruction were selected by requiring at least two reconstructed tracks satisfying different track quality criteria. The z_{Vertex} position of such events in the target-in and -out data sample and their reduction by a z_{Vertex} Cut within the range of $[-640, 520]$ is illustrated in Figure 6.9. Even though this cut does not affect the number of events coming from the carbon target, the $P_{T_{out}}/P_{T_{in}}$-ratio reduction is not efficient. For further details please refer to the presentation of my work [128].

6.4 Trigger Cross Section after Event Selection

In Section 6.2 the trigger cross section had been evaluated from the observed interaction probabilities for target-in and -out operation before any offline event selection had been performed. Now, that suitable bias-free event cuts have been chosen in order to reduce the target-out background, one can recalculate the trigger cross section from the reduced event sample. As the trigger cross section is a physical quantity, it should be independent of the offline bias-free

Run	N_{trig}	BPD-Cut (I)		BPD-Cut (II)		BPD-Cut (I+II)	
		N'_{trig}	A	N'_{trig}	A	N'_{trig}	A
5621	690	673	0.975 ± 0.038	632	0.916 ± 0.036	629	0.912 ± 0.036
5622	11717	11498	0.981 ± 0.009	10915	0.932 ± 0.009	10840	0.925 ± 0.009
5639	14026	13774	0.982 ± 0.008	12987	0.926 ± 0.008	12923	0.921 ± 0.008
5640	9561	9347	0.978 ± 0.010	8855	0.926 ± 0.010	8787	0.919 ± 0.010
5641	5494	5355	0.975 ± 0.013	5065	0.922 ± 0.013	5021	0.914 ± 0.013
5642	5229	5063	0.968 ± 0.014	4789	0.916 ± 0.013	4723	0.903 ± 0.013
5643	295	291	0.986 ± 0.058	275	0.932 ± 0.056	274	0.929 ± 0.056
5645	430	425	0.988 ± 0.048	406	0.944 ± 0.047	404	0.940 ± 0.047
5646	859	844	0.983 ± 0.034	782	0.910 ± 0.033	776	0.903 ± 0.032
All Runs w/o 5641, 5642	37578	36852	0.981 ± 0.005	34852	0.927 ± 0.005	34633	0.922 ± 0.005

Table 6.5: Summary table of runs with trigger on beam which have been studied for the evaluation of A. N_{trig} and N'_{trig} correspond to the number of triggered events before and after applying BPD-Cut (I/II/I+II), respectively. Numbers are based on the 07L production. The corresponding table for 07H production is given in Appendix B.

event selection according to

$$\sigma_{trig} = \frac{1}{\rho L_{eff} N_A/A}\,(P_{int}) = \frac{1}{\rho L'_{eff} N_A/A}\,(P_{int})' \quad , \tag{6.16}$$

$$\text{with} \quad P_{int} = P_{T_{in-out}}(1 + P_{T_{out}}) \quad \text{and} \quad P'_{int} = P'_{T_{in-out}}(1 + P'_{T_{out}}) \quad .$$

Here, the prime refers to the respective quantities after the event selection. Since no information on the BPD measurements of the gated beam particles has been recorded during the 2007 data taking, $P'_{T_{in}}$ and $P'_{T_{out}}$ are calculated from

$$P'_{T_{in},T_{out}} = \left(\frac{N'_{trig}}{N'_{beam}}\right)_{T_{in},T_{out}} = \frac{1}{A}\left(\frac{N'_{trig}}{N_{beam}}\right)_{T_{in},T_{out}} \quad , \tag{6.17}$$

where A is determined using runs with trigger on beam according to

$$A = \frac{N'_{trig}}{N_{trig}} < 1 \quad . \tag{6.18}$$

In Table 6.5 all the special runs with trigger on beam, which were studied for the evaluation of A, are listed. In this table numbers are based on the 07L production. Respective numbers for the 07H production can be found in Appendix B. For runs 5643, 5645 and 5646 no particle

		A	$\mathbf{P_{Tin}}$ [%]	$\mathbf{P_{Tout}}$ [%]	$\mathbf{P_{int}}$ [%]	$\mathbf{L_{eff}}$ [cm]	$\sigma_{\mathbf{trig}}$ [mb]
07H	No Cut	–	7.105±0.009	1.718±0.008	5.480±0.012	1.9447	305.5±0.7
	(I)	0.910±0.005	6.030±0.034	0.745±0.007	5.324±0.035	1.9463	296.6±2.0
	(II)	0.708±0.004	5.958±0.035	0.721±0.007	5.276±0.036	1.9468	293.8±2.0
	(I+II)	0.673±0.004	5.869±0.036	0.706±0.008	5.199±0.037	1.9475	289.5±2.1
07L	No Cut	–	7.104±0.009	1.719±0.008	5.477±0.012	1.9447	305.4±0.7
	(I)	0.981±0.005	6.141±0.032	0.757±0.007	5.424±0.033	1.9453	302.3±1.9
	(II)	0.927±0.005	6.045±0.034	0.715±0.007	5.368±0.034	1.9458	299.1±1.9
	(I+II)	0.922±0.005	6.022±0.034	0.709±0.007	5.351±0.035	1.9460	298.1±1.9

Table 6.6: Summary table of the factor A, the interaction probabilities for target-in and -out (P_{Tin} and P_{Tout}), the real interaction probability (P_{int}), the effective length (L_{eff}) and the trigger cross section (σ_{trig}) before and after BPD Cut (I) and (II). Numbers are given for the 07H and 07L production.

identification was present during data taking (see Table B.1). Therefore, the factor A has only been determined from those events, which had at least a 6-fold coincidence for the CEDAR counter. The threshold Cherenkov counter could not be taken into account for these studies, since its information had not been recorded for the 2007 data. Studies have shown, that the magnetic stray-field of the dipole magnet downstream of BPD3, VTX-1, did not have any influence on the measured BPD-positions. Moreover, it has been noticed that for runs 5641 and 5642 the vertical BPD1 position was significantly lower than for all of the other runs causing more beam tracks to fail the BPD-cuts. Therefore, these two runs were excluded from the evaluation of A. For all other runs the measured BPD positions indicated, that the same beam conditions as for the runs with standard trigger conditions were present.

With the mean factor A as given in Table 6.6, the trigger cross section after the offline event selection can be recalculated and compared to the corresponding value determined before the event selection. The resulting values are given in Table 6.6 for both the 07L and 07H production. Differences between the two productions are noticeable due to the fact, that the BPD cluster reconstruction had been improved for the 07L production leading to a smaller impact of the BPD cuts on the event reduction. As the 07L production is believed to be the most advanced, the final value of the trigger cross section presented in this work is based on it. Because of the fact, that for the strongest BPD cut, BPD-Cut (I+II), the target-out background becomes smallest, the nominal value for the trigger cross section is chosen to be the one after BPD-Cut (I+II). The largest discrepancy, which is seen between the value before

cuts and the one after BPD-Cut (I+II), is considered as systematic error on the trigger cross section. Thus, the final value of the trigger cross section is given by

$$\sigma_{trig} = (298.1 \pm 1.9 \pm 7.3)\text{mb} \quad ,$$

with the first error denoting the statistical error and the second one the systematic error. Note, that the high statistics 2009 data, for which the trigger logics have been improved to simultaneously record beam and interaction triggers throughout the run, should allow for further diminishing statistical and systematic uncertainties on the trigger cross section. As discussed in Section 8.3, the current precision on the trigger cross section, however, already now proves satisfactory for fulfilling the requirements of T2K.

6.5 Effect of the Remaining Target-Out Contribution on the Particle Yields

Event cuts have been chosen in order to reduce the background from events that happened outside of the carbon target. Even though the chosen cuts are efficient in considerably cleaning up the event sample, a small fraction of target-out events remains in the target-in data sample. To account for this remaining fraction when determining the particle yield from the target-in sample, one has to apply the following correction, that has formerly been adopted in [95, 115].

One can say, that the target-in data set (T_{in}) contains the sum of the carbon target events, C, as well as target-out events (T_{out}) happening in the material outside of the carbon target, which can be expressed with the yields and the interaction probabilities as follows

$$P_{int}\left(\frac{\Delta n_\alpha}{N_{trig}}\right)_C = \left(P_{T_{in}}\left(\frac{\Delta n_\alpha}{N_{trig}}\right)_{T_{in}} - P_{T_{out}}\left(\frac{\Delta n_\alpha}{N_{trig}}\right)_{T_{out}}\right)\cdot(1+P_{T_{out}})\,, \quad \alpha = \pi,\, K,\, p \quad . \tag{6.19}$$

Here, $\Delta n_\alpha / N_{trig}$ corresponds to the respective particle yield and $P_{int} = P_{T_{in-out}}(1+P_{T_{out}})$ to the real interaction probability in the target (see Section 6.2). With $\varepsilon = P_{T_{out}}/P_{T_{in}}$ one can rewrite this equation as follows

$$\left(\frac{\Delta n_\alpha}{N_{trig}}\right)_C = \frac{1}{1-\varepsilon}\left(\left(\frac{\Delta n_\alpha}{N_{trig}}\right)_{T_{in}} - \varepsilon\left(\frac{\Delta n_\alpha}{N_{trig}}\right)_{T_{out}}\right) \quad , \tag{6.20}$$

Note, that if event cuts, like BPD Cut (I+II) (see Section 6.3), are applied to evaluate the particle yields, N_{trig} and ε correspond to the number of events and the fake trigger probability after the cuts, respectively. Equation 6.20 shows that in order to correct the measured particle yield for the bias caused by non-target events one can in principle determine the yields in target-

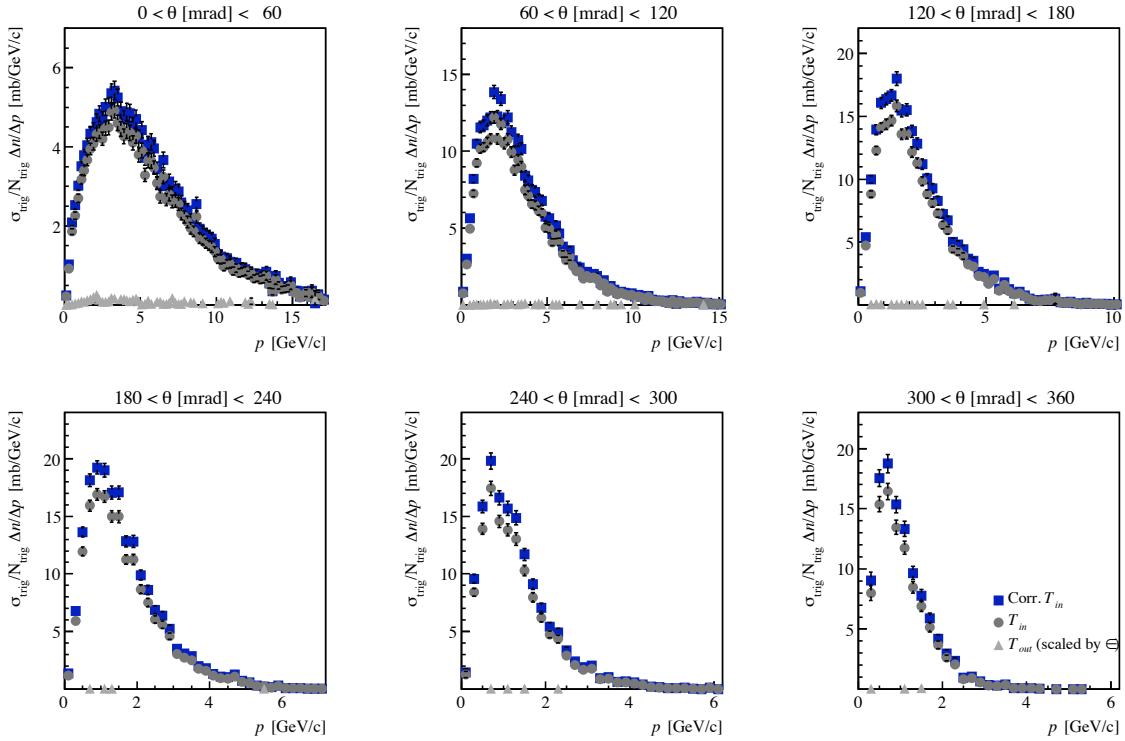

Figure 6.10: Corrected target-in (blue square), target-in (grey circle) and target-out (grey triangle) differential inclusive cross sections for π^- versus momentum in different polar angle intervals from the preliminary negatively charged hadron analysis [130] (see Chapter 8). Only statistical errors are shown. Note, that the target-out spectra are already scaled by ε and that their contribution is small (for the angular interval $(0 < \theta < 60)$mrad below 2% and for the other intervals below 0.5%). Therefore, the correction mainly comes from the normalization factor $1/(1-\varepsilon)$.

in and -out conditions separately and then subtract the target-out yield bin-by-bin from the target-in yield according to the Formula 6.20. To illustrate how this is practically done, the target-in, target-out and corrected target-in $1/N_{trig}\Delta n/\Delta p$ π^--spectra from the preliminary negatively charged hadron analysis[11] [130] are shown in Figure 6.10 for different polar angle bins. Note, that here the presented target-out spectra are already scaled by ε. From the spectra one can see, that the target-out contribution is small, hence, the correction for the remaining out-of-target contribution mainly comes from the normalization factor $1/(1-\varepsilon)$. When applying BPD Cut (I+II) on the 07L production, the resulting value for $1/(1-\varepsilon)$ amounts to $1.134 \pm 0.001(stat.)$.

6.6 Trigger Bias on the Shape of the Particle Spectra

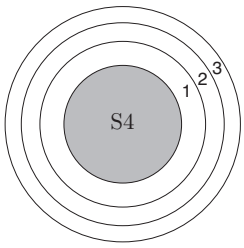

Figure 6.11: The principle of the S4 bias evaluation is based on the idea that one artificially increases S4 and then extrapolates to area (radius) zero.

The interaction trigger defined by S4 may cause a bias of the shape of the particle spectra. This bias is possible, if the loss of inelastic events is correlated with the kinematic properties of produced particles: events, in which high momentum, forward going particles are present, are more probable to be removed by S4, than others. High momentum particles, which are hitting S4, do not lie in the geometrical acceptance of the Vertex TPCs required for the particle identification analyses and would therefore not have been measured, even if the events would have been recorded. However, the other particles present in such events, might have been detected in the TPCs, if the event would not have been lost. Due to the fact, that particles are produced in a correlated way, the S4 trigger may primarily remove events of a particular event topology and may therefore affect certain phase space regions more than others and consequently distort the shape of the particle spectra.

To check, whether the shape of the particle spectra is biased by the trigger, one would ideally compare particle spectra with the trigger bias to the respective spectra without the

[11] The analysis of negatively charged particles is based on the theoretical and experimental premises, that negative particles produced by 30 GeV protons consist mainly of negative pion mesons with a small admixture of electrons, negative kaons and a negligible fraction of antiprotons. This procedure allows to obtain spectra of π^- mesons in the full momentum range.

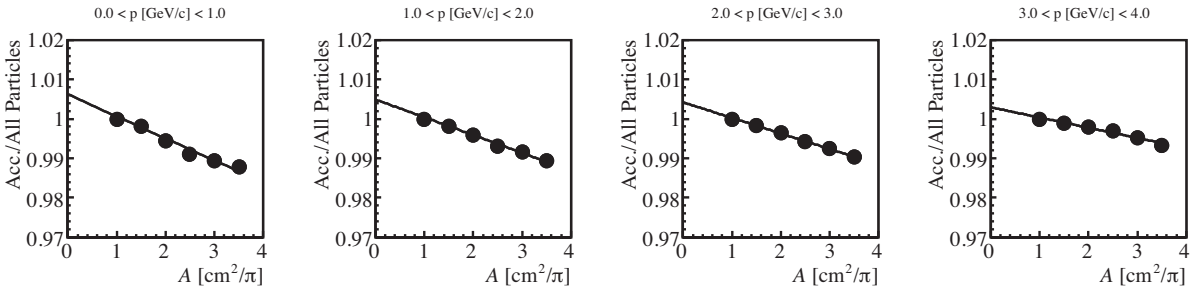

Figure 6.12: The ratio of accepted over all negative particles as a function of the S4 area for different momentum bins in the polar angle range from $60 - 100$mrad.

bias. A possible way to perform such a comparison is by using MC simulations and producing events with and without the S4 bias. This approach would however be model dependent. A model independent practice should be based on the data. As the trigger bias cannot be removed from the recorded data anymore, the idea is to further increase the bias and see, whether the spectrum shape of the particles changes. This can be done by artificially increasing the S4 counter offline and observing the effect on the particle yield (see Figure 6.11). If one sees a dependence in the change of the particle yield in a given phase space bin with growing S4, one can extrapolate this change back to S4 area zero and hence obtain the undistorted particle yields.

Studies have been performed with the thin target data, in which the S4 radius squared has been artificially increased in steps of 0.5 cm^2. With the help of the GTPC tracks, it has been checked whether any of the produced particles had a hit in the increased S4 or not. Positive and negative primary particle distributions, after the usual track selection cuts[12], have then been analyzed for all events and those events, which had no tracks hitting the increased S4. The ratio of the accepted particles over all has been evaluated as a function of the S4 area for different momentum–polar angle bins and extrapolated with a polynomial function to zero in order to obtain the correction factors (see as an example Figure 6.12). The resulting corrections were in the low momentum–angular region of the order of 1% or below and decreasing when going to higher momenta and polar angles (see as an example Figure 6.13). The phase space dependence can be explained by the fact, that through the S4 bias mainly high momentum, forward going particles are removed, which are present in events, where there has consequently only been a small momentum deposition for the other particles (if there were any other particles at all). For more information please refer to [129]. As the differential S4 bias corrections depend on the given particle species, one should in principle implement such a procedure in the respective particle identification analyses, so as to extract corrections, which

[12]The number of points in VTPC-1 and -2 has to be larger than twelve, the number of potential points has to be larger than 30 and the impact parameter has to less than 4 cm.

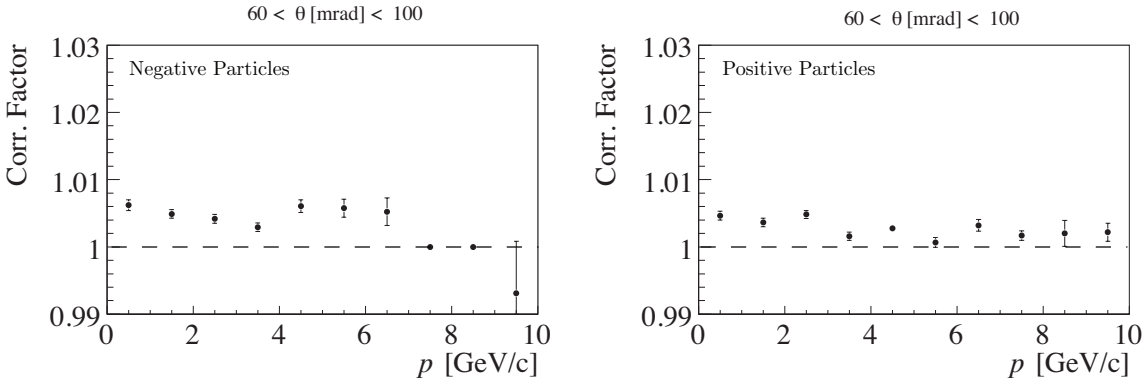

Figure 6.13: The S4 bias correction factor as a function of the momentum for negative (left) and positive (right) particles in the θ-angle interval from $60 - 100$ mrad.

are specific to the particle type and their identification (e.g. track selection). As concluded for the charged particle spectra, the S4 bias should, however, only have a minor effect.

This conclusion is consistent with the results obtained from the GEANT4 simulations presented in the following Chapter 7. The latter show, that only about 2% of the inelastic interactions are lost due to emitted particles hitting S4. They also show, that a large contribution of these losses come from incoherent elastic scattering of the incident protons on the individual nucleons of the nuclei. In these quasi-elastic events, no other secondary particles are produced, thus no bias on, for example, the measured particle yields is introduced.

Chapter 7

Inelastic p+C Cross Section

So far, the trigger cross section has been presented, which is needed for normalizing the measured particle yields to the inclusive cross section. If one, however, intends to normalize the particle yields to the mean multiplicity in inelastic proton–carbon interactions, one needs to further determine the total inelastic cross section (for details see Chapter 8). The latter is here defined in such a way, that it includes all processes due to strong interactions with the exception of the coherent elastic proton–carbon interactions. Contrary to the trigger cross section, the inelastic cross section is not only important for normalizing the particle spectra, but is also interesting as a measurement on its own right, as it represents a physical quantity that can be compared to measurements from other experiments. When conducting such comparisons, it is essential to ensure, that the same definition of the inelastic cross section has been used, as it varies in literature—sometimes the quasi-elastic contribution is, like in NA61, taken into account when computing the inelastic cross section and other times it is not. This issue has therefore carefully been taken into account. From the inelastic cross section one can furthermore calculate what here is called the production cross section, which is defined as the inelastic minus the quasi-elastic cross section. The production cross section thus only involves processes, which are actually contributing to the hadron production, because in both, coherent elastic and quasi-elastic interactions hadrons are not produced. As will be described in the final Chapter 8, the production cross section therefore forms the determining factor for the normalization of the NA61 particle yields for the T2K experiment.

Section 7.1 presents the corrections, which have to be applied in order to obtain the total inelastic proton–carbon cross section from the measured trigger cross section. Also the production cross section will be given in this section. Then in Section 7.2, the resulting value for the inelastic cross section is compared to the measurements from previous experiments.

	Standard Value	Value for Sys. Studies
Beam Divergence	110μrad	100μrad
RMS of Beam	2.1 mm	2.3 mm
Target Density	1.8395 g/cm^3	1.84 g/cm^3
Target Length	2 cm	2 cm
Radius of S4	1 cm	9.5 mm, 10.5 mm
x-Position of S4	9.00 mm	8.30 mm
y-Position of S4	0.00 mm	1.75 mm

Table 7.1: Parameters used for the GEANT4 simulation (left) and the ones used for systematic studies (right). The latter have been chosen to reflect the uncertainties seen in the data.

7.1 Inelastic Cross Section Determination

The trigger cross section can, as has been demonstrated in Section 6.5, be calculated from the interaction probability for target in and target out operation. The analysis of the 2007 run data thereby leads to a trigger cross section of $(298.1 \pm 1.9 \pm 7.3)$mb. The total inelastic cross section (σ_{inel}) can then be derived from the the trigger cross section (σ_{trig}) by applying the following three corrections:

- Subtract the contribution due to coherent elastic scattering out of S4 ($\sigma_{el-Out\ of\ S4}$):
  Remove those events, where the beam particle undergoes a large angle coherent elastic scattering on the target nuclei and does not reach the S4 counter. Therefore, a trigger on the event is present, even if no inelastic proton interaction occurred.
- Add the loss due to emitted protons hitting S4 ($\sigma_{\mathrm{loss-p}}$):
  Take into account interactions, where an emitted proton hits the S4 counter and therefore prevents from triggering on the event. Here, the quasi-elastic scattering (σ_{qe}), where the incident protons scatter off the individual nucleons of the nuclei, comes into play. For more information on quasi-elastic proton–carbon scattering see Appendix C.
- Add the loss due to emitted pions and kaons hitting S4 (see $\sigma_{\mathrm{loss-}\pi/\mathrm{K}}$):
  Take into account interactions, where an emitted pion or kaon at high longitudinal momentum hits the S4 counter and therefore prevents from triggering on the event.

These corrections have been estimated based on the GEANT4 [116] simulation of the trigger setup conducted by myself. Measured profile and divergence of the proton beam were used in

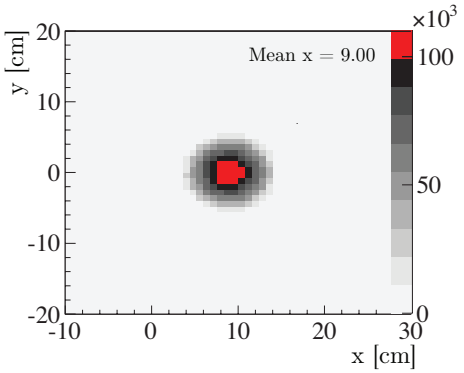

Figure 7.1: Deflection of the simulated beam in the $x-y$ plane at z = -211.6 cm, which corresponds to the position of S4.

this simulation (see Chapter 5). The beam and target parameters which were employed are summarized in Table 7.1. For an accurate description of the deflection of the simulated particles in the NA61 magnetic field, the measured field map from NA61 has been implemented in the simulation framework. To check its correct implementation, the beam deflection in the $x-y$ plane at the $z-$position of the S4 counter (z = -211.6 cm) has been studied (see Figure 7.1). A shift of 9.00 mm in $x-$direction can be observed, which is in good agreement with the measured x-position of 9.06 mm. For modeling the proton–carbon interactions at 30 GeV the string model based `QGSP_BERT`[1] physics list has furthermore been used.

The resulting angular distributions for coherent elastic scattering and quasi-elastic scattering are given in Figure 7.2. Their dependence on the four-momentum transfer squared[2] (t) is in addition presented in Figure 7.3. As expected from previous measurements, discussed in Appendix D, the coherent elastic scattering, where the nucleus remains close to its ground state, shows a steep decline in the lower t-region, while the larger t-region can instead be described by predominant quasi-elastic scattering, in which one of the nucleons present in the nucleus recoils violently enough to break the nuclear bond.

The cross section values for inelastic, coherent elastic and quasi-elastic scattering, which have been obtained from the GEANT4 simulations, have been cross-checked against available experimental measurements[3], as it is shown in Table 7.2. Good agreement between the GEANT4 simulation and the known experimental values is seen, however an 11% discrepancy on the total elastic cross section value is observed.

[1] Recommended by the GEANT4 collaboration [131]. `QGS` stands for Quark Gluon String model [132], `P` for precompound and `BERT` for Bertini cascade model [133, 134].

[2] Let p_0 be the laboratory momentum of the incoming proton and p the momentum of the outgoing proton scattered elastically at an angle Θ, then the four-momentum transfer squared is given at highly relativistic energies and at angles $\Theta \ll 1$ to a very good approximation by $|t| \approx p_\perp^2 \approx p^2\Theta^2 \approx p_0^2\Theta^2$, where $p_\perp$ is the transverse momentum of the scattered particle.

[3] Note, that although the energy dependence is rather flat, the literature values have been obtained at different proton momenta (see Table 7.4).

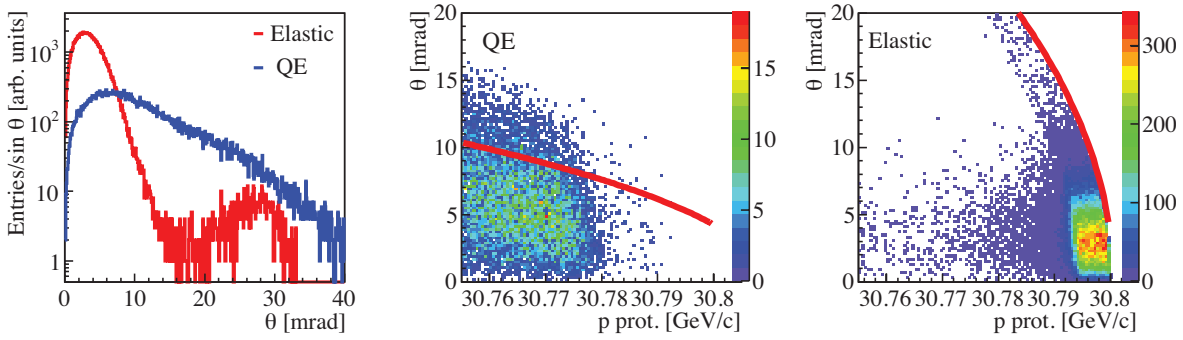

Figure 7.2: *Left:* Angular distribution of protons undergoing coherent elastic scattering on the nucleus (red) and quasi-elastic scattering on individual nucleons (blue). The second peak in the elastic distribution is most probably a secondary diffraction maximum. *Middle:* Angular distribution as a function of the momentum of protons undergoing quasi-elastic scattering on individual nucleons. The red curves correspond to the kinematical limit for target nucleons at rest, which can be exceeded in case of the quasi-elastic scattering due to Fermi motion. *Right:* Angular distribution as a function of the momentum of protons undergoing coherent elastic scattering on the nucleus. All distributions have been obtained with GEANT4 simulations.

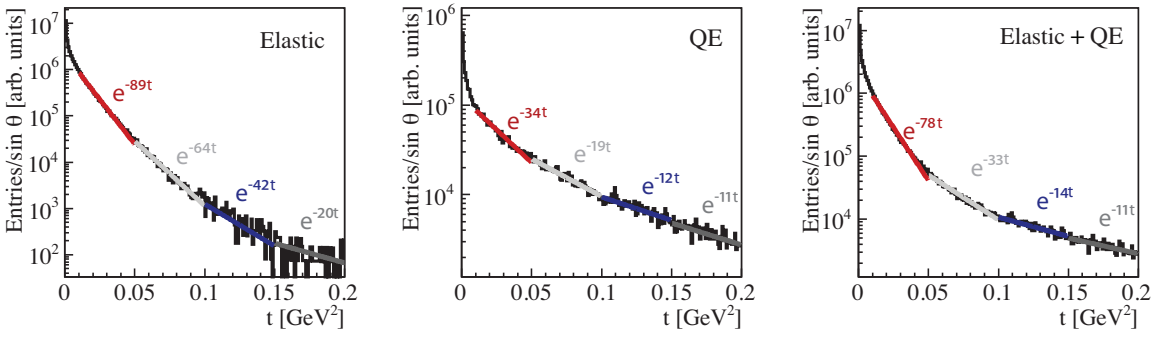

Figure 7.3: Four-momentum transfer squared (t) distributions for elastic (left) and quasi-elastic scattering (middle) protons of 30 GeV on carbon and their sum (right). Distributions have been obtained with GEANT4 simulations and fitted with exponential fits in four different t-regions.

σ **contribution**	**Exp. Measurements [mb]**	**GEANT4 [mb]**
σ_{inel}	254±6 [117], 247±4 [118], 248±7 [119]	243.8 ±0.4
σ_{el}	81±4 [117]	71.9±0.2
$\sigma_{el-Out\ of\ S4}$	51±3 [117] (63%)	47.2±0.2 (65.6%)
σ_{qe}	27.9±1.5	27.6±0.1
$\sigma_{qe-Out\ of\ S4}$	26.0 ± 4.4 (93.2%)	25.7±0.2 (93.3%)

Table 7.2: Comparison of the GEANT4 cross sections to the expected ones from previous measurements. The percentage indicates the fraction of protons missing S4. Calculation details for σ_{qe} and $\sigma_{el,qe-Out\ of\ S4}$ can be found in Appendix C and D, respectively. Note, that the value from [119] has been recalculated in order to use a consistent definition of σ_{inel}, where σ_{qe} is taken into account (for details see Appendix C). Also note, that, except for the values from previous experiments, only statistical errors are given here.

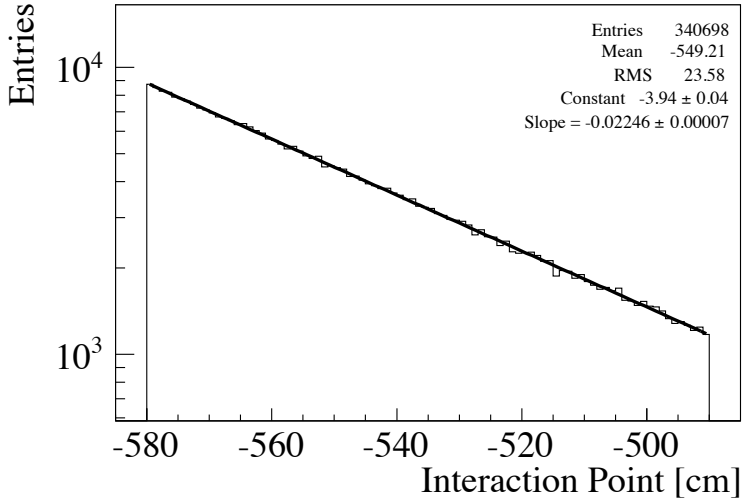

Figure 7.4: Simulated distribution of the inelastic interaction points in the T2K replica target using GEANT4.

The total inelastic cross section from GEANT4 has furthermore been evaluated with another simulation, where the thin carbon target has been replaced by the 90 cm long T2K replica target. From the exponential distribution of the interaction points of inelastic reactions in the long target, as presented in Figure 7.4, an absorption length of 44.5 cm can be derived. With this absorption length one obtains an inelastic cross section of 243.6 mb (see Eq. 6.14), which is consistent with the value from the thin target simulation (see Table 7.2).

The corrections used to evaluate the total inelastic cross section from the trigger cross section are given in Table 7.3. From the given numbers one can conclude, that the overall correction to the trigger cross section amounts to $(40.9 \pm 0.3 \pm 5.0)$mb. Rejected events mainly come from incoherent elastic scattering of the incident protons on the individual nucleons of the nuclei and produced protons hitting the S4 counter, while the contribution from produced pions or kaons hitting S4 is small. By far the largest correction to the trigger cross section comes from the additional events, that are due to large angle coherent elastic scattering out of S4.

To check, whether the elastic contribution out of S4, which represents by far the largest correction to the inelastic cross section, could also be evaluated from the data, simulations with the NA61 simulation chain, which includes the geometrical acceptance and the reconstruction efficiency of the NA61 detector, have been performed. It has been seen, that the acceptance for elastically scattered beam particles in the VTPC's and MTPC's is practically zero. For more information please refer to [135]. Further studies have been conducted with the thin target data, where the GTPC had been included during data taking. As the GTPC covers the forward acceptance, one could in principle determine the angular distribution and t-dependence of the elastically and quasi-elastically scattered tracks. It however arose that the resolution of the GTPC is not sufficient to allow for such measurements [120]. In summary, it follows, that the coherent elastic scattering out of S4, which makes up the largest correction to the trigger cross section, cannot be determined from the data. The current estimation of the elastic contribution out of S4 (see Table 7.3), which is based on GEANT4 simulations, however offers a fair accuracy for the evaluation of the inelastic cross section (see Chapter 8).

The systematic error on the trigger cross section, which is given in Table 7.3, has been estimated with the help of several cross-checks, that have been presented in Section 6.1. For the corrections, $\sigma_{el-Out\ of\ S4}$, σ_{loss-p} and $\sigma_{loss-\pi/K}$, the systematic errors have been evaluated by varying the different beam and target parameters of the GEANT4 simulation according to their respective expected uncertainty. The variations used for the systematic studies are given in Table 7.1 together with the standard values. The maximum discrepancy from the nominal value has been used as systematic error. For the elastic contribution out of S4 the discrepancy between the GEANT4 value and the one expected from the experimental measurement of [117] has furthermore been taken into account. The corrections to the trigger cross section result in a total inelastic cross section of

$$\sigma_{inel} = (257.2 \pm 1.9 \pm 8.9)\text{mb} \quad ,$$

with the first error denoting the statistical error and the second one the systematic error. From the total inelastic cross section one can determine what here is called the production cross section, which is given by the inelastic cross section minus the quasi-elastic one ($\sigma_{prod} = \sigma_{inel} - \sigma_{qe}$). If one uses a quasi-elastic proton–carbon cross section at 30 GeV of $(27.9 \pm 1.5(sys.))$mb

σ **Contribution**	**Value [mb]**
σ_{trig}	$298.1 \pm 1.9 \pm 7.3$
$\sigma_{el-Out\ of\ S4}$	$-47.2 \pm 0.2 \pm 5.0$
σ_{loss-p}	$+5.7 \pm 0.2 \pm 0.5$
$\sigma_{loss-\pi/K}$	$+0.57 \pm 0.02 \pm 0.35$
σ_{inel}	$257.2 \pm 1.9 \pm 8.9$

Table 7.3: Cross section corrections estimated using GEANT4 simulation.

(see Appendix C), one obtains a production cross section of

$$\sigma_{prod} = (229.3 \pm 1.9 \pm 9.0)\text{mb} \quad ,$$

again with the first error representing the statistical error and the second one the systematic error.

7.2 Comparison to Previous Measurements

The NA61 measurement on the inelastic cross section can be compared to measurements from previous experiments. When conducting such comparisons it is important to ensure, that the same definition of the inelastic cross section as in NA61 ($\sigma_{inel} = \sigma_{tot} - \sigma_{el}$), where the quasi-elastic contribution is taken into account, has been used. While for Bellettini *et al.* [117] this is the case, Carroll *et al.* [119] subtracted in addition to the coherent elastic contribution also the quasi-elastic contribution (σ_{qe}) from the total cross section, which is what here is called the production cross section. In order to use a consistent definition of the inelastic cross section for the comparison, the value from [119] has been recalculated by adding the quasi-elastic cross section to the published value. In Appendix C it is explained in detail how the recalculation has been performed. For the measurements from Denisov *et al.* [118] it has not been clearly stated in the publication, whether the quasi-elastic contribution had been subtracted or not. For clarification the authors were contacted, which resulted in the conclusion that the quasi-elastic contribution had not been subtracted. Therefore, comparisons presented here are based on the values as published in [118]. As this conclusion was, however, not completely unambiguous, recalculated values are also given in Appendix C. This ambiguity is stressed in [119], where the 60 GeV/c cross section measurement from Denisov *et al.* [118] was directly compared to the one from Carroll *et al.* [119], for which the quasi-elastic contribution was subtracted. It was remarked that no reason for their discrepancy, which amounts to 11%, could be found.

	p_{lab} [GeV/c]	σ_{inel} [mb]
NA61	30.8	$257.2 \pm 1.9 \pm 8.9$
Bellettini [117]	21.5	254±6
Carroll [119]	60	248±7
Denisov [118]	20	249±3
	30	247±4
	40	246±3
	50	248±3
	60	252±5

Table 7.4: Comparison of σ_{inel} from NA61 to previous measurements. The value for [119] has been recalculated as explained in Appendix C. For [118], σ_{inel} is given as published, recalculated values are presented in Appendix C.

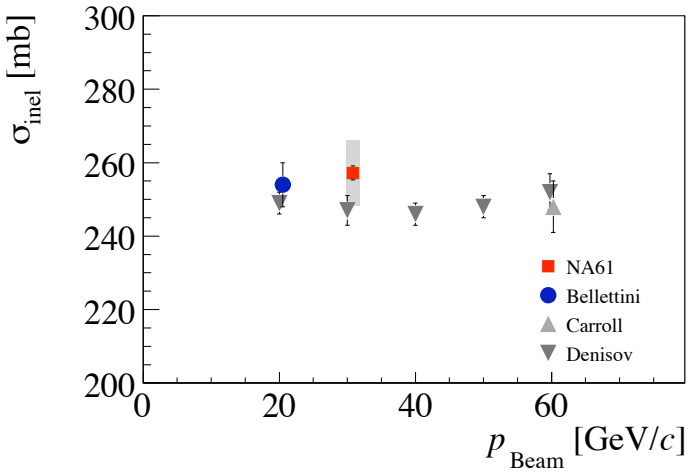

Figure 7.5: Comparison of the NA61 proton–carbon inelastic cross section to previous measurements [117, 118, 119]. For NA61, the line corresponds to the statistical errors, whereas the shaded area represents the systematic error. The value for [119] has been recalculated as explained in Appendix C. For [118], σ_{inel} is given as published, recalculated values are presented in Appendix C.

Figure 7.5 illustrates the comparison of the various inelastic cross sections and shows that the inelastic cross section determined by NA61 is consistent with the literature values [117, 118, 119] within the given uncertainties. Chapter 8 discusses the degree to which the accuracy of the NA61 inelastic cross section measurement satisfies the requirements of the T2K experiment.

Chapter 8

Normalized Particle Yields

The different proton-carbon cross section measurements presented in the previous chapters are used to normalize the various particle yields determined with the NA61 detector. While the trigger cross section is employed to normalize the particle yields to the inclusive cross section, the inelastic and production cross sections are utilized to respectively normalize the particle yields to the mean multiplicity in inelastic and production interactions. So far, yields for positively and negatively charged pions have been obtained from the 2007 data via three different particle identification methods. For particle identification in the low momentum region (below 1 GeV/c), which is not covered by the time-of-flight detectors, a dedicated analysis based on energy loss measurements in the time projection chambers is used [123]. To identify particles with momenta above 1 GeV/c, the energy loss measurements are combined with the time-of-flight information [124]. For the identification of negatively charged pions, the analysis of negatively charged particles, also referred to as h^- analysis, is furthermore employed [127]. For the three different particle identification methods a common Venus-GHEISHA [136, 92] and Geant Monte Carlo [92] simulation chain is used to calculate corrections for geometric acceptance, reconstruction efficiency, weak decays and vertex association [123, 124, 127]. The resulting particle yields are finally normalized as described here. The results have been published in [137].

Section 8.1 demonstrates how the particle yields obtained from the different particle identification methods are normalized to the inclusive cross section and to the mean multiplicity in inelastic and production interactions. Then, in Section 8.2, the normalized particle spectra are compared to the ones obtained from the GEANT4 simulations described in Chapter 7. In the final Section 8.3 the influence of the NA61 results on the T2K experiment is discussed.

8.1 Normalization of Particle Yields

The corrected particle yields in different momentum–polar angle bins, normalized to the double differential inclusive cross section of the respective particle type α, are given by

$$\frac{\mathrm{d}\sigma_\alpha}{\mathrm{d}p\mathrm{d}\theta} = \frac{1}{1-\epsilon}\frac{\sigma_{trig}}{N'_{trig}}\frac{\Delta n_\alpha}{\Delta p \Delta\theta} \quad [\mathrm{mb}/\ \mathrm{GeV}/c\ /\mathrm{mrad}]. \tag{8.1}$$

For this, the following normalization factors have to be employed

- $\sigma_{trig} = (298.1 \pm 1.9 \pm 7.3)$mb—the corrected trigger cross section as given in Section 6.4.
- N'_{trig}—the number of events left after the bias free event selection, that were used for the evaluation of the particle yields.
- $\Delta p \Delta\theta$—the experimental bin size in momentum and polar angle. In case one transforms the two-dimensional histograms into one-dimensional momentum spectra within a given polar angle range, one only has to normalize to the momentum bin size (Δp).
- $1/(1-\epsilon)$—the normalization factor, which corrects for the remaining out-of-target contribution. Note, that the target-out to target-in ratio (ϵ) has to be chosen according to the event cuts and the production, which were used for the evaluation of the particle yields (see Table 6.4). When using the event cut as proposed here, BPD Cut (I+II), and the 07L production, the resulting value for $1/(1-\varepsilon)$ amounts to $1.134 \pm 0.001(stat.)$.

The total error on the inclusive cross sections resulting from the normalization thus amounts to 2.5%.

For the normalization of the particle yields to the mean multiplicity in inelastic collisions

$$\frac{\mathrm{d}n_{inel,\alpha}}{\mathrm{d}p\mathrm{d}\theta} = \frac{1}{\sigma_{inel}} \cdot \frac{\mathrm{d}\sigma_\alpha}{\mathrm{d}p\mathrm{d}\theta} \quad [1/\ \mathrm{GeV}/c\ /\mathrm{mrad}], \tag{8.2}$$

the inclusive cross section, as given in Equation 8.1, has to be divided by

- $\sigma_{inel} = (257.2 \pm 1.9 \pm 8.9)$mb—the inelastic cross section as presented in Section 7.1. Note, that the errors on the trigger cross section and the inelastic cross section are correlated, so that their ratio results in $\sigma_{trig}/\sigma_{inel} = 1.159 \pm 0.002 \pm 0.023$.

The total error on the mean multiplicities in inelastic interactions, which are due to the normalization, amounts to 2.0%. Note once again, that the total inelastic cross section is here defined in such a way, that it includes all processes due to strong interactions, with the exception of the coherent elastic proton–carbon interactions.

For the hadro-production measurements required by the T2K experiment, it is most suitable to normalize the NA61 particle yields to the production cross section, given that the latter represents the inelastic cross section devoid of the quasi-elastic one, and thus, only involves processes, which are actually contributing to the hadron and consequently to the neutrino production. To normalize the NA61 particle yields to the mean multiplicity in production interactions

$$\frac{\mathrm{d}n_{prod,\alpha}}{\mathrm{d}p\mathrm{d}\theta} = \frac{1}{\sigma_{prod}} \cdot \frac{\mathrm{d}\sigma_{\alpha}}{\mathrm{d}p\mathrm{d}\theta} \quad [1/\ \mathrm{GeV}/c\ /\mathrm{mrad}], \tag{8.3}$$

one has to use

- $\sigma_{prod} = (229.3 \pm 1.9 \pm 9.0)$mb—the production cross section as given in Section 7.1. The errors of the trigger cross section and the production cross section are correlated, so that their ratio results in $\sigma_{trig}/\sigma_{prod} = 1.300 \pm 0.002 \pm 0.030$.

The total error on the mean multiplicities in production interactions caused by the normalization amounts to 2.3%.

Differential yields for positively and negatively charged pions have been obtained from the 2007 data, using the three particle identification methods: $\mathrm{d}E/\mathrm{d}x$ [123], combined $\mathrm{d}E/\mathrm{d}x$ + TOF [124] and h^- [127]. An agreement of better than 10% is, in general, observed between the three analyses. Figure 8.1 demonstrates how the resulting particle yields are normalized to the inclusive cross section and to the mean multiplicity in inelastic and production interactions. The final NA61 results have been obtained from the different normalized spectra by selecting the measurement with the smallest total error in each momentum-angle bin. The results have been published in [137].

8.2 Comparison to GEANT4 Simulations

The results from the NA61 combined analysis on the differential inclusive cross sections for positively and negatively charged pions in inelastic proton–carbon interactions at 30 GeV can be compared to the corresponding ones, which were obtained from the GEANT4 simulations described in Section 7.1. Figures 8.2 and 8.3 show the comparison for negatively and positively charged pions, respectively. One can see that especially for low production angles GEANT4 fails to reproduce the NA61 measurements. These differences have not been understood so far and should further be investigated. Comparison of the NA61 results to FLUKA [63], GHEISHA [92] and UrQMD [138] can furthermore be found in [137]. It appears that the hadronization model used in the T2K experiment, FLUKA, offers the best agreement with the NA61 data.

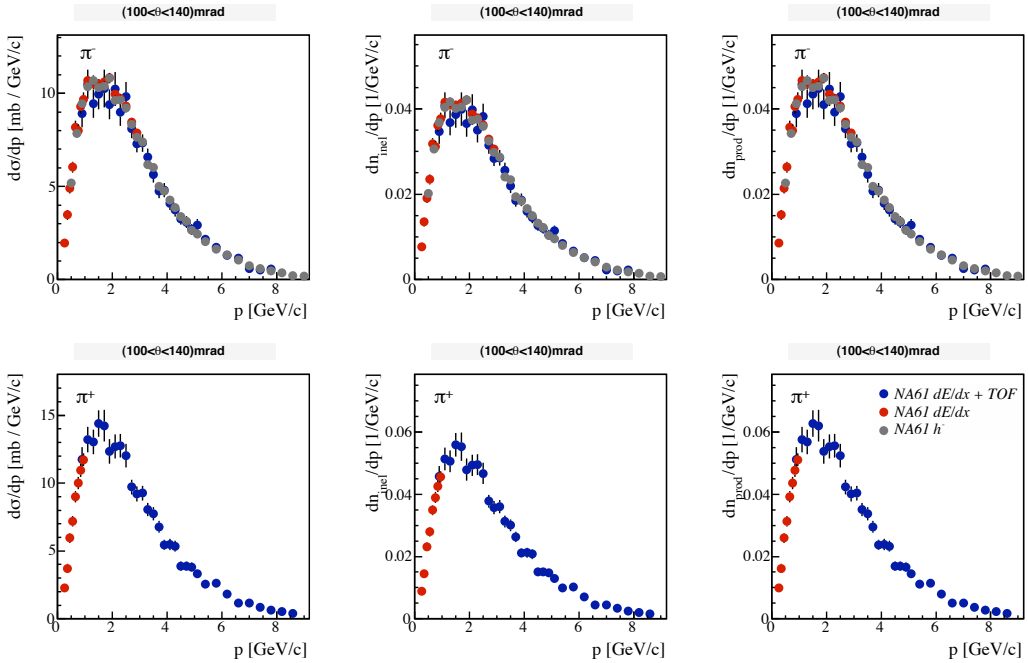

Figure 8.1: *Left:* Differential inclusive cross sections for π^- (top) and π^+ (bottom) versus momentum in the θ-angle interval ($100 < \theta < 140$ mrad) obtained from $\mathrm{d}E/\mathrm{d}x$ (red), $\mathrm{d}E/\mathrm{d}x$ + TOF (blue) and h^- (gray) analyses. *Middle and Right:* Mean multiplicity in inelastic (middle) and production (right) interactions, again for π^- (top) and π^+ (bottom) versus momentum in the θ-angle interval ($100 < \theta < 140$ mrad) for the different analyses. Error bars indicate statistical uncertainties only. The NA61 particle yields have been taken from [137].

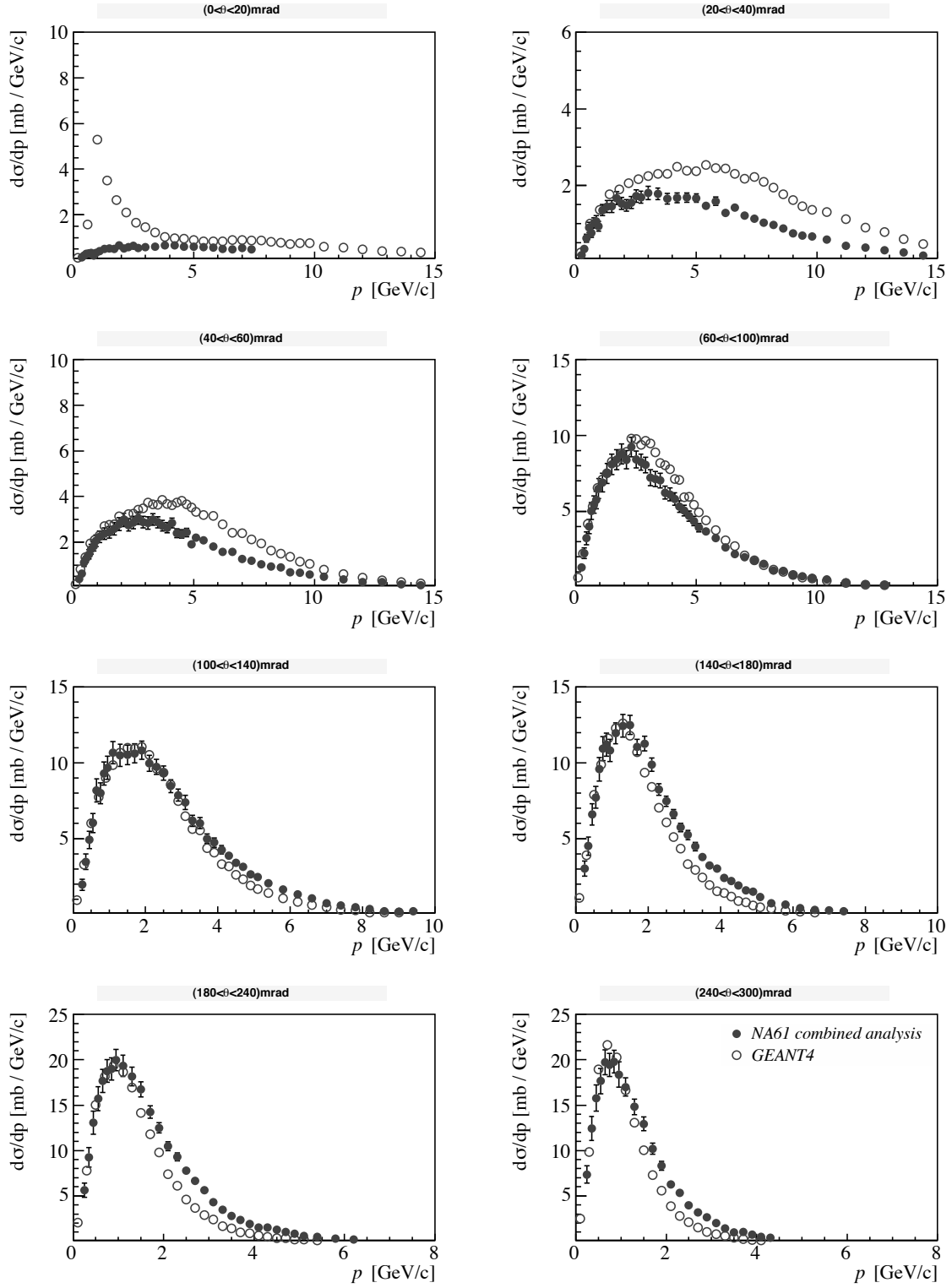

Figure 8.2: Differential inclusive cross sections for π^- versus momentum in different θ-angle intervals obtained from the combined NA61 analysis (full circles) compared to the corresponding results from GEANT4 (open circles). The NA61 particle yields are shown with total errors as given in [137].

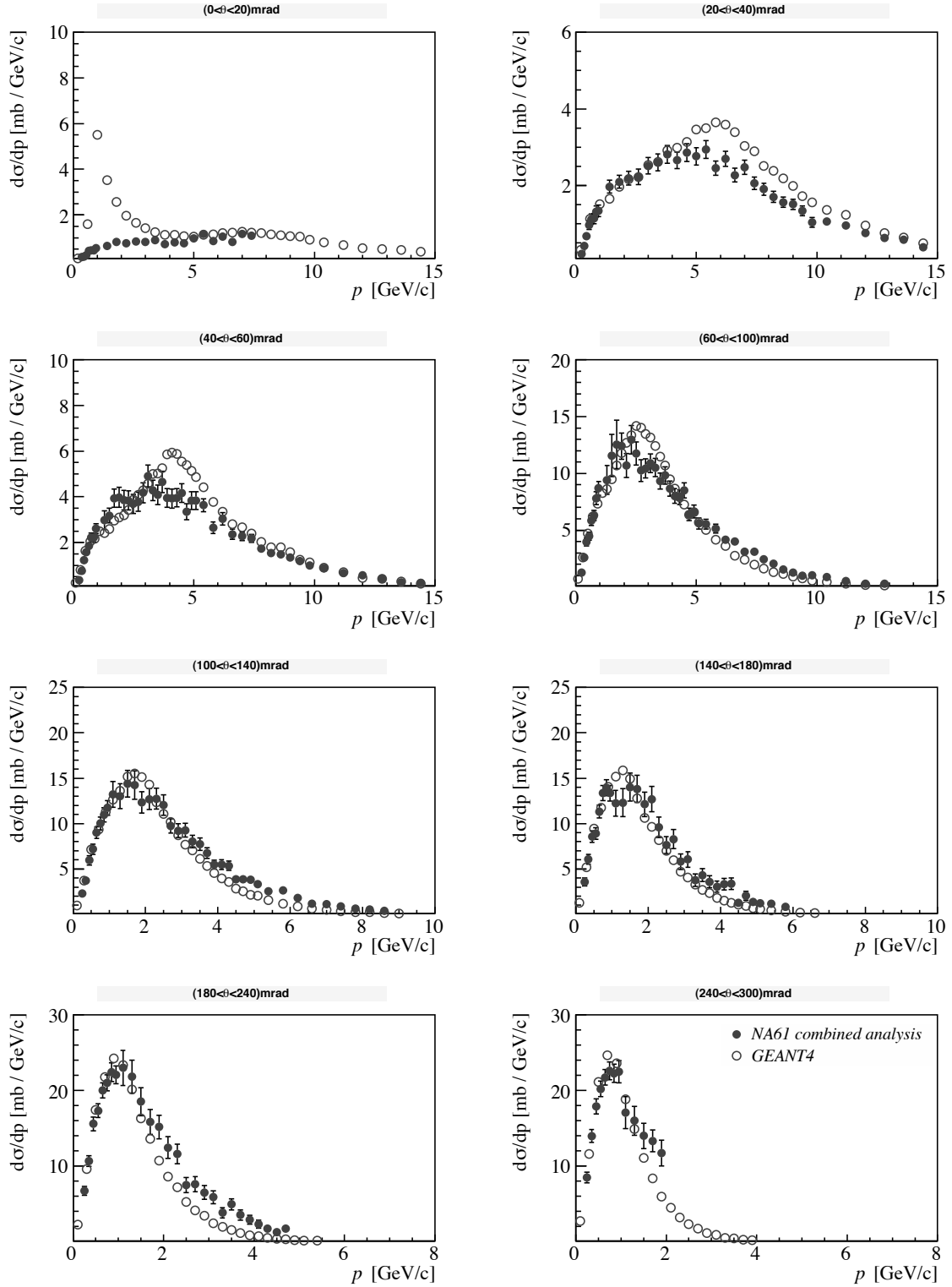

Figure 8.3: Differential inclusive cross sections for π^+ versus momentum in different θ-angle intervals obtained from the combined NA61 analysis (full circles) compared to the corresponding results from GEANT4 (open circles). The NA61 particle yields are shown with total errors as given in [137].

8.3 Influence on T2K

As described in Section 8.1, the differential particle yields from NA61 are normalized for T2K using the measured trigger cross section as well as the proton–carbon production cross section in order to obtain the mean multiplicities in production interactions. The total uncertainty caused by the normalization procedure hereby amounts to 2.3%. The minor effect that the NA61 cross section measurement uncertainties have on the absolute flux predictions in T2K can be verified with the following. Let N be the number of non-interacting beam particles in the target, which can be calculated from

$$N = N_0 \exp\left(-\frac{L}{\lambda}\right) \quad , \tag{8.4}$$

with N_0 denoting the number of incident beam particles, L the target length and λ the nuclear interaction length of the target. Then it follows that the relative change of non-interacting particles with respect to the total number of particles on target is given as a function of the uncertainty on the interaction length ($\Delta\lambda$) by

$$\frac{\Delta N}{N_0} = \frac{L}{\lambda}\frac{\Delta\lambda}{\lambda}\exp\left(-\frac{L}{\lambda}\right) \quad . \tag{8.5}$$

An uncertainty on the nuclear interaction length of 2.3% would thus lead to a relative change in the absolute flux of about 0.6%. Here a nuclear interaction length of 44.5 cm, as estimated from the GEANT4 simulations presented in Chapter 7, has been assumed. This demonstrates, that the uncertainties on the NA61 cross section measurements have a marginal effect on the absolute flux predictions in T2K. The achieved precision of the NA61 cross section measurements has thus proven satisfactory for T2K.

The preliminary NA61 results on the positively and negatively charged pions, as presented in [104, 105, 139], are already being employed in the T2K experiment. Their comparison to the hadronization models used in the T2K beam simulation has shown that FLUKA [63] reproduces the NA61 data best. This also holds true for the final results published in [137]. The comparison of the preliminary results from NA61 to the results from FLUKA are presented in Figure 8.4 for positively and negatively charged pions. The discrepancies lie within the given systematic uncertainties of 20%, which were conservatively estimated from the maximum difference between the three particle identification analyses used in NA61. Work on tuning the T2K beam simulation with the NA61 data is currently under investigation. At the time, NA61 results are implemented by reweighting the primary pion production in FLUKA with the NA61 measurements. The effect from the reweighting on the predicted neutrino flux at Super-Kamiokande is demonstrated in Figure 8.5. The latter shows the expected muon neutrino flux at Super-Kamiokande before and after tuning FLUKA with the preliminary NA61 data. In the region under the oscillation peak ($\approx$ 650 MeV), the NA61 tuning effect is below 1%, however,

going to higher neutrino energies it increases to almost 7%. The minimal tuning required demonstrates FLUKA's ability to predict the primary pion production, which until this study was unverified by data. Secondary pion as well as primary and secondary kaon production is yet to be investigated with the NA61 thin target and T2K replica target data.

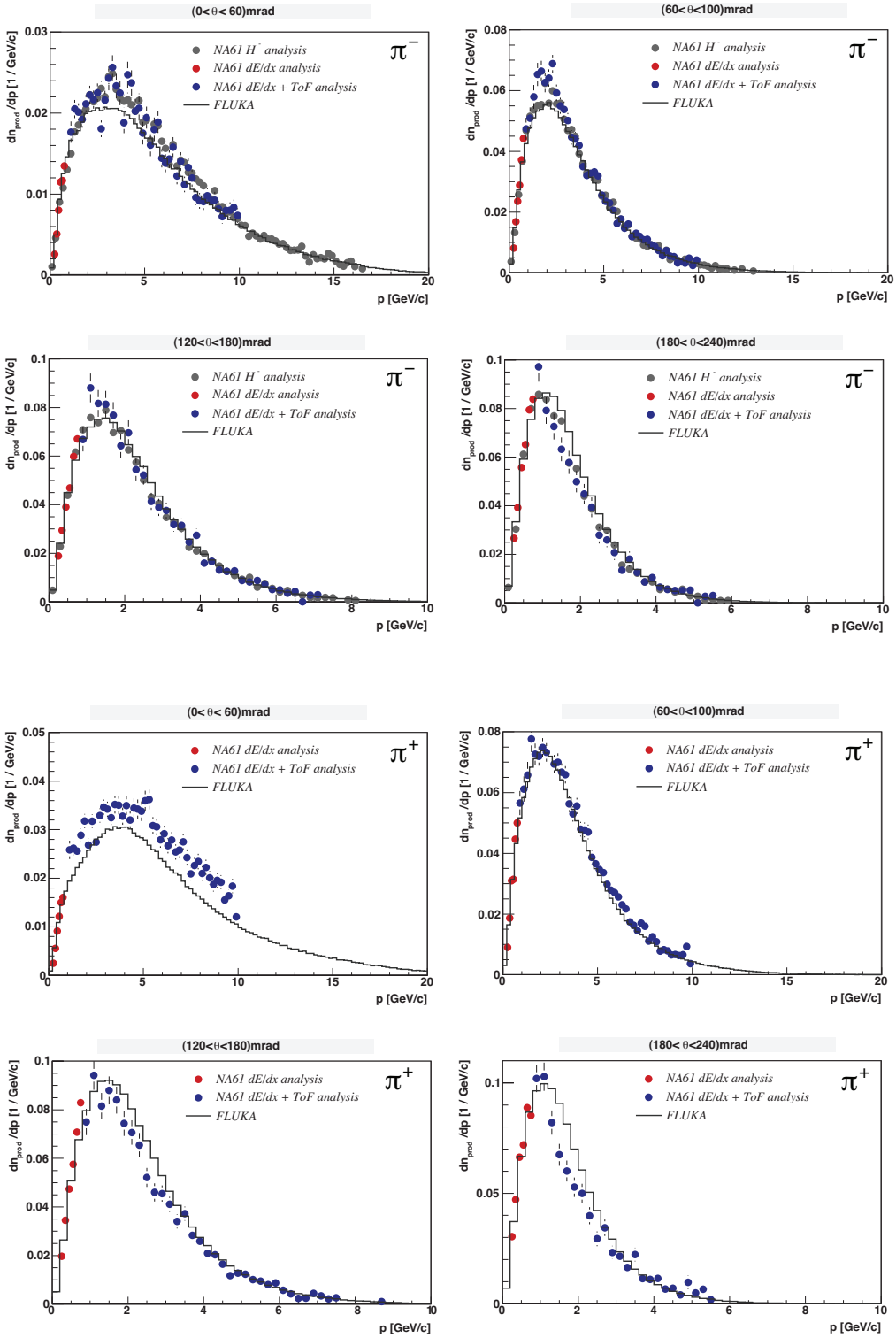

Figure 8.4: Preliminary π^- (upper panel) and π^+ (lower panel) mean multiplicities in production interactions versus momentum in different θ-angle intervals as presented by NA61 in [104, 105, 139] and simulated with FLUKA [63]. The 20% systematic error for the preliminary NA61 data is not shown in the plots.

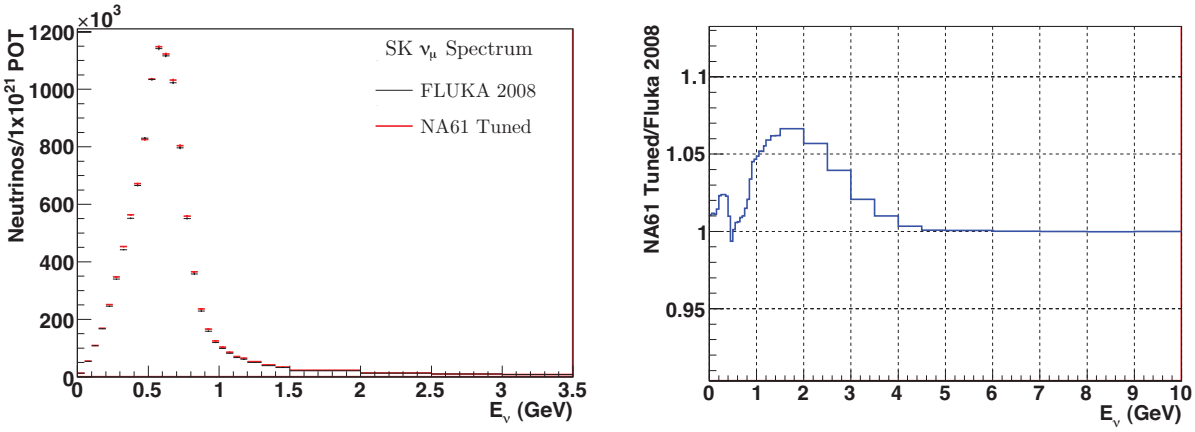

Figure 8.5: ν_μ flux at SK from FLUKA before and after NA61 tuning (left) and their ratio (right). Both figures are taken from: [140]

Chapter 9

Summary and Conclusions

In this work the inelastic and production cross sections of 30 GeV proton–carbon interactions, as well as the normalization procedure used for the evaluation of the inclusive cross sections and particle yields of positively and negatively charged pions have been presented. The results are based on data collected with the large acceptance NA61/SHINE spectrometer at the CERN SPS during 2007. The measurements have been performed with a 30 GeV proton beam and an isotropic graphite target of about 4% nuclear interaction length.

The trigger cross section was found to be (298.1±1.9±7.3)mb; calculated after careful event selection from the interaction probability for inserted target operation. It was also corrected for triggered events outside of the target as well as for the exponential beam attenuation in the target. The systematic error on the trigger cross section has been evaluated conservatively by comparing this value with the one obtained without any event selection.

The proton–carbon inelastic cross section resulted in $(257.2 \pm 1.9 \pm 8.9)$mb. This was derived from the measurement of the trigger cross section by applying corrections based on GEANT4 simulation of the beam line setup using the measured profile and divergence of the proton beam. The largest correction relates to the coherent elastic scattering out of S4, which has been cross-checked against an available experimental measurement. The discrepancy was taken into account in the calculation of the systematic error, which also includes uncertainties in other simulation parameters, namely beam position and divergence, and size of the S4 counter. Comparison of the given inelastic cross section to the ones from previous experiments has shown consistency within the assigned uncertainties.

The proton–carbon production cross section was found to be $(229.3 \pm 1.9 \pm 9.0)$mb. This was determined from the inelastic cross section by subtracting the cross section of quasi-elastic proton-carbon interactions at 30 GeV, which yields to $(27.9 \pm 1.5(sys.))$mb according to the Glauber model calculations.

The various cross section measurements were then used for the normalization of the measured particle yields. In the normalization distortions of the particle yields due to events outside of the carbon target were considered. Bias on the shape of the particle spectra due to the trigger condition, however, were found to be negligible. The total uncertainty for the normalization to the inclusive cross section and mean multiplicity in inelastic and production interactions amount to 2.5%, 2.0% and 2.3%, respectively.

The NA61 hadron production measurements are aimed for improving predictions of the initial neutrino flux of the long-baseline neutrino oscillation experiment T2K at JPARC, Japan. It has been demonstrated in this work, that the total error on the particle spectra caused by the normalization procedure do have a marginal effect on the absolute flux predictions in T2K. The achieved precision of the NA61 cross section measurements has thus proven satisfactory for T2K.

Appendix A

List of Standard Runs

Table A.1 and A.2 both list the 2007 thin target runs with standard trigger condition $S1 \cdot S2 \cdot \overline{V} \cdot C1 \cdot \overline{C2} \cdot \overline{S4}$ for the 07H and 07L production, respectively. For each run the number of triggered events before cuts, after BPD Cut (I), BPD Cut (II) and BPD Cut (I+II) are stated together with the number of gated beam particles as well as the interaction probability. Note, that the number of triggered events used to evaluate given numbers are slightly less than the total number of recorded events since counting is started after the end of the first spill. Furthermore one should note, that the cut reduction for the two productions are different due to changes in the BPD reconstruction client, where the threshold for the cluster reconstruction had been lowered for the 07L production (see Table 4.4). Table A.3 and A.4 give the same numbers for the 2007 target out runs with standard trigger condition.

Run	Events	BPD-Cut (I)	BPD-Cut (II)	BPD-Cut (I+II)	B_{gated}	P_{Tin} [%]
5560	42126	32200	24795	23008	590776	7.131 ± 0.035
5563	3170	2444	1873	1735	45771	6.926 ± 0.123
5566	2309	1771	1373	1275	30905	7.471 ± 0.155
5567	29	20	16	15	442	6.561 ± 1.218
5569	39960	30915	23530	21948	565412	7.067 ± 0.035
5570	37241	28776	21720	20306	522547	7.127 ± 0.037
5574	12016	5775	4362	4001	167666	7.167 ± 0.065
5575	17782	13555	6785	6309	249876	7.116 ± 0.053
5577	575	450	146	142	8046	7.146 ± 0.298
5578	8804	6943	5140	4930	121094	7.270 ± 0.077
5579	36712	28784	21583	20509	515896	7.116 ± 0.037
5580	14838	11723	8810	8390	207370	7.155 ± 0.059
5581	11125	8830	6265	6002	155648	7.147 ± 0.068
5582	9861	7633	5540	5240	138672	7.111 ± 0.072
5583	3539	1643	1292	1204	48803	7.251 ± 0.122
5584	2216	1692	1312	1218	30877	7.177 ± 0.152
5590	298	218	63	58	3681	8.096 ± 0.469
5591	37141	28594	22223	20550	522597	7.107 ± 0.037
5592	30850	23885	18513	17234	436918	7.061 ± 0.040
5595	23456	18128	14349	13317	330779	7.091 ± 0.046
5596	572	464	394	365	8144	7.024 ± 0.294
5598	2468	1940	1523	1431	34847	7.082 ± 0.143
5599	21328	16477	13110	12214	301080	7.084 ± 0.049
5600	300	241	186	178	4157	7.217 ± 0.417
5601	506	59	47	43	42092	1.202 ± 0.053
5602	33972	26537	20860	19514	478099	7.106 ± 0.039
5603	226	165	132	121	3271	6.909 ± 0.460
5604	134	100	82	75	1775	7.549 ± 0.652
5605	15927	12441	9740	9046	225116	7.075 ± 0.056
5607	13318	10398	8067	7520	188449	7.067 ± 0.061
5608	43097	33706	26336	24629	610178	7.063 ± 0.034
5611	34927	27401	21656	20293	491326	7.109 ± 0.038
5612	8287	6564	5133	4845	116021	7.143 ± 0.078
5617	29638	23218	18327	17119	422020	7.023 ± 0.041
5618	27645	21779	17251	16114	389251	7.102 ± 0.043
5625	6694	5286	4172	3929	92315	7.251 ± 0.089
5626	3766	3010	2361	2229	52682	7.149 ± 0.116
5629	14160	11081	8756	8255	198662	7.128 ± 0.060
5635	1637	1297	1024	968	22973	7.126 ± 0.176
5636	27244	21297	17051	15992	384001	7.095 ± 0.043
5637	12007	9484	7535	7128	167040	7.188 ± 0.066
5638	37630	29868	23854	22589	531466	7.080 ± 0.036
All (w/o 5601)	669025	516733	397240	371945	9416649	7.105 ± 0.009

Table A.1: List of 2007 target-in runs (07H).

Run	Events	BPD-Cut (I)	BPD-Cut (II)	BPD-Cut (I+II)	B_{gated}	P_{Tin} [%]
5560	42119	35481	33150	32733	590776	7.129 ± 0.035
5563	3170	2681	2504	2469	45771	6.926 ± 0.123
5566	2309	1933	1822	1795	30905	7.471 ± 0.155
5567	29	23	19	19	442	6.561 ± 1.218
5569	39953	33834	31610	31278	565412	7.066 ± 0.035
5570	37241	31573	29518	29262	522547	7.127 ± 0.037
5574	7598	6431	5948	5867	105829	7.180 ± 0.082
5575	17779	14986	8944	8831	249876	7.115 ± 0.053
5577	575	480	174	172	8046	7.146 ± 0.298
5578	8803	7450	6965	6927	121094	7.270 ± 0.077
5579	36707	31091	29112	28954	515896	7.115 ± 0.037
5580	15795	13421	12595	12527	220538	7.162 ± 0.057
5581	11122	9524	8844	8803	155648	7.146 ± 0.068
5582	9860	8353	7765	7710	138672	7.110 ± 0.072
5583	3538	1816	1701	1686	48803	7.250 ± 0.122
5584	2216	1851	1743	1725	30877	7.177 ± 0.152
5590	297	245	98	98	3681	8.068 ± 0.468
5591	37135	31595	29628	29338	522597	7.106 ± 0.037
5592	30844	26122	24590	24305	436918	7.059 ± 0.040
5595	23454	19911	18716	18517	330779	7.091 ± 0.046
5596	572	499	485	476	8144	7.024 ± 0.294
5598	2468	2112	1986	1971	34847	7.082 ± 0.143
5599	21326	18068	17067	16889	301080	7.083 ± 0.049
5600	299	256	242	240	4157	7.193 ± 0.416
5601	506	66	61	61	42092	1.202 ± 0.053
5602	33968	28967	27232	26974	478099	7.105 ± 0.039
5603	226	187	176	174	3271	6.909 ± 0.460
5604	134	108	103	100	1775	7.549 ± 0.652
5605	15926	13655	12888	12751	225116	7.075 ± 0.056
5607	13316	11330	10672	10585	188449	7.066 ± 0.061
5608	43090	36782	34657	34376	610178	7.062 ± 0.034
5611	34919	29746	28090	27849	491326	7.107 ± 0.038
5612	8281	7096	6682	6621	116021	7.138 ± 0.078
5617	29630	25281	23830	23611	422020	7.021 ± 0.041
5618	27638	23619	22358	22134	389251	7.100 ± 0.043
5625	6693	5704	5412	5377	92315	7.250 ± 0.089
5626	3766	3232	3067	3042	52682	7.149 ± 0.116
5629	14158	12019	11313	11216	198662	7.127 ± 0.060
5635	1636	1400	1326	1318	22973	7.121 ± 0.176
5636	27239	23136	21865	21656	384001	7.093 ± 0.043
5637	12004	10181	9663	9600	167040	7.186 ± 0.066
5638	37626	32136	30382	30167	531466	7.080 ± 0.036
All (w/o 5601)	665459	564315	524942	520143	9367980	7.104 ± 0.009

Table A.2: List of 2007 target-in runs (07L).

Run	Events	BPD-Cut (I)	BPD-Cut (II)	BPD-Cut (I+II)	B_{gated}	P_{Tout} [%]
5561	1754	677	499	467	99924	1.755 ±0.042
5562	9284	3685	2734	2565	539405	1.721 ± 0.018
5571	2385	901	665	617	137622	1.733 ± 0.035
5573	7607	2935	2193	2034	437850	1.737 ± 0.020
5593	3592	1435	1091	1013	216172	1.662 ± 0.028
5594	6380	2550	1933	1787	369856	1.725 ± 0.022
5615	3553	1402	1061	982	206686	1.719 ± 0.029
5616	2879	1108	825	767	171691	1.677 ± 0.031
5633	387	159	127	121	21778	1.777 ± 0.090
5634	6975	2829	2174	2038	406535	1.716 ± 0.021
All	44796	17681	13302	12391	2607519	1.718 ± 0.008

Table A.3: List of 2007 target-out runs (07H).

Run	Events	BPD-Cut (I)	BPD-Cut (II)	BPD-Cut (I+II)	B_{gated}	P_{Tout} [%]
5561	1754	731	660	654	99924	1.755 ± 0.042
5562	9983	4306	3816	3762	578169	1.727 ± 0.017
5571	2385	990	890	872	137622	1.733 ± 0.035
5573	7607	3255	2869	2830	437850	1.737 ± 0.020
5593	3592	1574	1411	1397	216172	1.662 ± 0.028
5594	6379	2815	2521	2485	369856	1.725 ± 0.022
5615	3553	1536	1358	1341	206686	1.719 ± 0.029
5616	2879	1237	1103	1087	171691	1.677 ± 0.031
5633	387	176	156	155	21778	1.777 ± 0.090
5634	6973	3034	2749	2719	406535	1.715 ± 0.021
All	45492	19654	17533	17302	2646283	1.719 ±0.008

Table A.4: List of 2007 target-out runs (07L).

Appendix B

List of Special Runs

Table B.1 summarizes the trigger conditions for the various runs with trigger on beam, which were recorded during the 2007 data taking. These runs were used to study the influence of the BPD cuts on the beam particles and to evaluate the reduction factor A (see Section 6.4). For some of the listed runs (5643, 5645, 5646) no particle identification via CEDAR nor threshold Cherenkov counter was present during data taking. Therefore, the factor A was only determined from those events for which at least a 6-fold coincidence for the CEDAR counter was present. The threshold Cherenkov counter, however, could not be used for these studies since its information had not been stored on tape. Table B.2 gives the results on the factor As for the different BPD cuts for production 07H. Corresponding numbers for the 07L production can be found in Table 6.5.

Run	Comment
5621	T_{in}, S1 $\cdot$ S2 $\cdot \overline{\text{V}} \cdot$ C1 $\cdot \overline{\text{C2}}$, std B-field
5622	T_{in}, S1 $\cdot$ S2 $\cdot \overline{\text{V}} \cdot$ C1 $\cdot \overline{\text{C2}}$, std B-field
5639	T_{in}, S1 $\cdot$ S2 $\cdot \overline{\text{V}} \cdot$ C1 $\cdot \overline{\text{C2}}$, std B-field
5640	T_{out}, S1 $\cdot$ S2 $\cdot \overline{\text{V}} \cdot$ C1 $\cdot \overline{\text{C2}}$, B-field ramped up
5641	T_{out}, S1 $\cdot$ S2 $\cdot \overline{\text{V}} \cdot$ C1 $\cdot \overline{\text{C2}}$, full B-field, not used
5642	T_{out}, S1 $\cdot$ S2 $\cdot \overline{\text{V}} \cdot$ C1 $\cdot \overline{\text{C2}}$, full B-field, not used
5643	T_{out}, S1 $\cdot$ S2 $\cdot \overline{\text{V}}$, full B-field, CEDAR
5645	T_{out}, S1 $\cdot$ S2 $\cdot \overline{\text{V}}$, full B-field, CEDAR
5646	T_{out}, S1 $\cdot$ S2 $\cdot \overline{\text{V}}$, B-field ramped up, CEDAR

Table B.1: List of runs with trigger on beam. CEDAR denotes, that when analyzing respective runs, only those events were used for which a 6-fold coincidence for the CEDAR counter was present.

Run	N_{trig}	BPD-Cut (I)		BPD-Cut (II)		BPD-Cut (I+II)	
		N'_{trig}	A	N'_{trig}	A	N'_{trig}	A
5621	690	620	0.899 ± 0.036	487	0.706 ± 0.032	458	0.664 ± 0.031
5622	11730	10798	0.921 ± 0.009	8610	0.734 ± 0.008	8247	0.703 ± 0.008
5639	14026	12800	0.913 ± 0.008	9945	0.709 ± 0.007	9468	0.675 ± 0.007
5640	9564	8541	0.893 ± 0.010	6493	0.679 ± 0.008	6091	0.637 ± 0.008
5641	5495	4760	0.866 ± 0.013	3729	0.679 ± 0.011	3412	0.621 ± 0.011
5642	5233	4442	0.849 ± 0.013	3573	0.683 ± 0.011	3201	0.612 ± 0.011
5643	295	274	0.929 ± 0.056	208	0.705 ± 0.049	202	0.685 ± 0.048
5645	430	392	0.912 ± 0.046	289	0.672 ± 0.040	272	0.633 ± 0.038
5646	859	764	0.889 ± 0.032	593	0.690 ± 0.028	552	0.643 ± 0.027
All Runs w/o 5641, 5642	37594	34189	0.910 ± 0.005	26625	0.708 ± 0.004	25290	0.673 ± 0.004

Table B.2: Summary table of runs with trigger on beam which have been studied for the evaluation of A. N_{trig} and N'_{trig} correspond to the number of events before and after applying BPD-Cut (I/II/I+II), respectively. Numbers are based on the 07H production.

Appendix C

Quasi-Elastic p+C Cross Section

Quasi-elastic hadron-nucleus scattering is defined as an interaction, where the incident hadron scatters off the individual nucleons of the nuclei. The nucleus is thereby brought into an excited state, which possibly decays subsequently, however, no secondary particle production occurs. The quasi-elastic proton–carbon cross section at 30.8 GeV/c is relevant for NA61 in order to evaluate the production cross section from the measured inelastic cross section (see Section 7.1). Next to that, the quasi-elastic cross section is needed for comparing the NA61 inelastic cross section to the ones from other experiments, as the definition of the inelastic cross section varies in literature. While Bellettini *et al.* [117] used the same definition as NA61, Carroll *et al.* [119] subtracted in addition to the coherent elastic contribution also the quasi-elastic contribution from the total cross section, so that it corresponds to what here is called the production cross section. In order to use a consistent definition of the inelastic cross section for the comparison of the various measurements, the value from [119] has to be recalculated by adding the quasi-elastic contribution to the published value. For the measurements from Denisov *et al.* [118] it has not been clearly stated in the publication, whether the quasi-elastic contribution had been subtracted or not. For clarification the authors were contacted, which resulted in the conclusion that the quasi-elastic contribution had not been subtracted. Therefore, comparisons presented in Section 7.2 have been conducted with the values as published in [118]. As this conclusion was, however, not completely unambiguous, the recalculated values from [118] are evaluated here, too. In order to recalculate measurements from [118] and [119], one needs to compute the quasi-elastic cross section for 20, 30, 40, 50 and 60 GeV/c beam momentum.

The required quasi-elastic proton–carbon cross sections have been evaluated by [141] using the Glauber model [142, 143]. The resulting values are summarized in Section C.1. The results are cross-checked with two different approximations described in Sections C.2 and C.3. All values are finally summarized and compared in Section C.4.

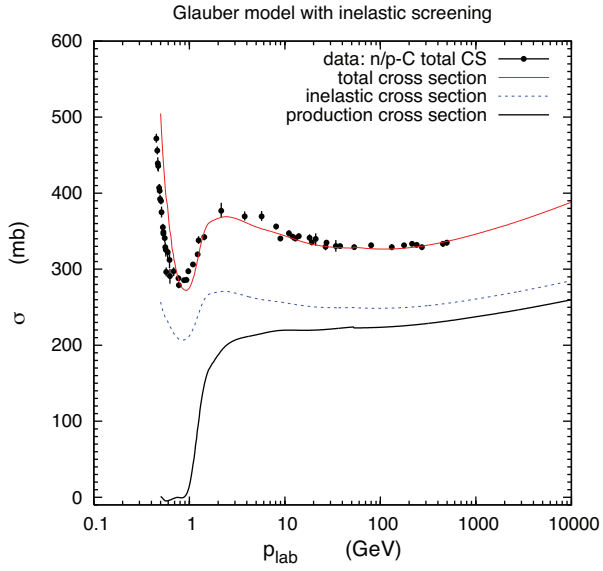

Figure C.1: Comparison of Glauber model predictions of neutron– and proton–carbon scattering with data. The model calculations include inelastic screening corrections following the parameterization of [144]. The figure is taken from: [141].

p_{lab} **[GeV/c]**	20	30	30.8	40	50	60
σ_{qe} **[mb]**	30.4 ± 1.5	28.0 ± 1.5	27.9 ± 1.5	26.5 ± 1.5	25.6 ± 2.0	26.2 ± 2.0

Table C.1: Quasi-elastic p+C cross sections at different momenta from Glauber model calculations with inelastic screening effects. Uncertainties have been evaluated by comparing these values to the ones obtained without inelastic screening. Numbers are taken from [141].

C.1 The Glauber Model

The Glauber model [142, 143] is a formalism for calculating hadron-nucleus cross sections at intermediate and high energies. It is based on the assumption, that interactions of the incident particle with the nucleons of the nuclei may individually be treated by means of the general methods of diffraction theory. The Glauber model has been widely used to calculate the hadron-nucleus cross sections and has offered a good overall description of measurements. In Figure C.1 this is demonstrated using the example of the neutron– and proton–carbon cross sections at different laboratory beam momenta (p_{lab}). The Glauber model parameterization used by [141] leads to the quasi-elastic proton–carbon cross sections as given in Table C.1.

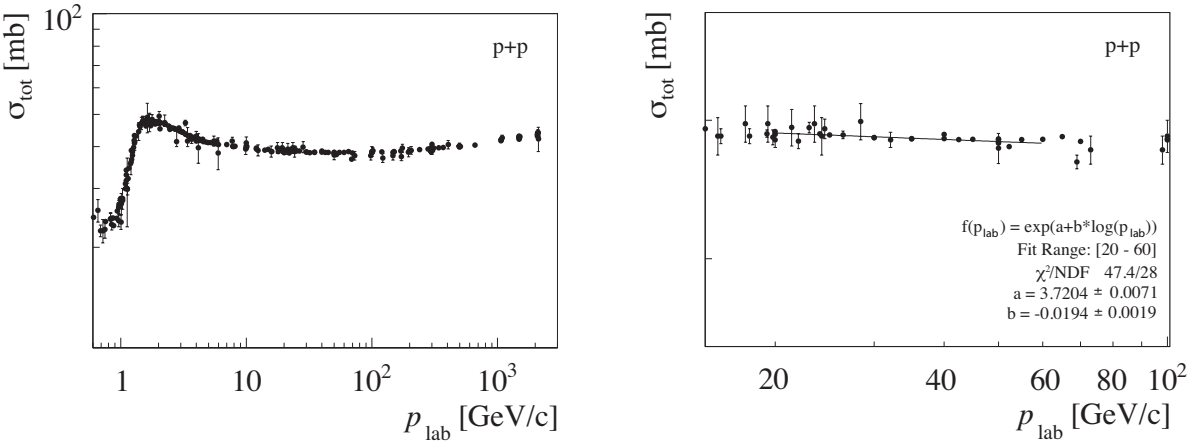

Figure C.2: All total cross sections for p+p collisions from [4] as a function of the laboratory beam momentum (p_{lab}) (left) and the ones fitted in the range of ($20 \leq p_{lab} \leq 60$) GeV/c (right).

C.2 Approximation I

According to [117], the differential quasi-elastic proton–carbon cross section at a given momentum (p) can be approximated on the basis of the optical theorem by

$$\frac{d\sigma}{d\Omega} = N(A) \left(\frac{p\sigma_{tot}(pp)}{4\pi\hbar} \right)^2 \exp\left(-C|t|\right) \quad . \tag{C.1}$$

with Ω denoting the solid angle and $|t|$ the four-momentum transfer squared. $N(A)$ is a factor describing the effective number of nucleons taking part in the incoherent process for target nuclei of mass A. The term $p\sigma_{tot}(pp)/4\pi\hbar$, with $\sigma_{tot}(pp)$ giving the total proton–proton cross section, describes the proton–proton forward scattering amplitude. Note, that the proton–proton and proton–neutron scatterings are here assumed to be the same. The exponential term, where C is a constant independent of the mass number A, characterizes the behavior of the proton–proton differential cross section as a function of the four momentum transfer squared (t).

The factor $N(A)$ has been measured for proton–carbon interactions [117] resulting in $N(A) = 3.4$. In the same publication it is stated that a satisfactory description of the dependence of $N(A)$ on A is given by the expression $N(A) = 1.6A^{1/3}$, which has the geometrical interpretation, that the beam particle can emerge from the collision with full energy only if it hits a nucleon situated on the surface of the nucleus. Since no error is given for the measurement, both, the measurement and the approximation, are used here and compared to each other for an error estimation.

To obtain the total proton–proton cross section at respective momenta, all available mea-

p_{lab} [GeV/c]	$\sigma_{tot}(pp)$ [**mb**]	C	σ_{qe} [**mb**]	
			$N(A) = 3.4$	$N(A) = 1.6A^{1/3}$
20	38.9 ± 0.4	10.2 ± 1.1	25.7 ± 2.9	27.7 ± 3.1
30	38.6 ± 0.4	10.6 ± 1.2	24.4 ± 2.8	26.3 ± 3.0
30.8	38.6 ± 0.4	10.7 ± 1.2	24.3 ± 2.8	26.2 ± 3.0
40	38.4 ± 0.4	10.9 ± 1.3	23.5 ± 2.7	25.3 ± 3.0
50	38.3 ± 0.4	11.1 ± 1.3	22.5 ± 2.7	24.2 ± 2.9
60	38.1 ± 0.4	11.3 ± 1.3	22.3 ± 2.7	24.0 ± 2.9

Table C.2: The total p+p cross section ($\sigma_{tot}(pp)$), the factor C and the quasi-elastic cross section (σ_{qe}) for $N(A) = 3.4$ as measured by [117] and $N(A) = 1.6A^{1/3}$ at different laboratory beam momenta.

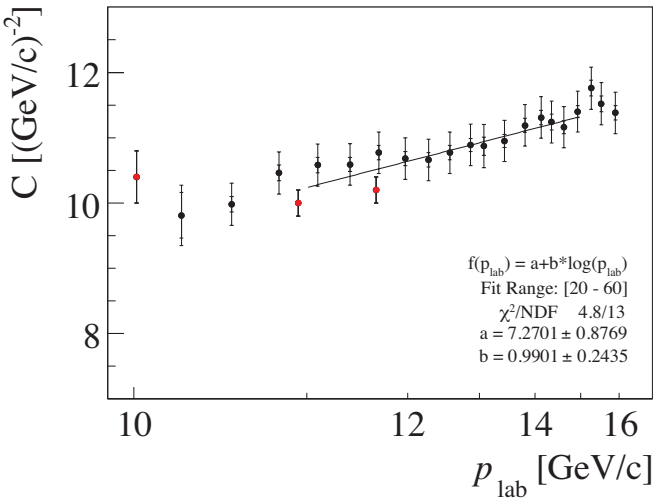

Figure C.3: The measured slope parameter C from data given in [145] (black) and [146] (red) as a function of the proton momentum. For the measurements from [145] statistical and systematic errors are presented.

surements summarized in [4] have been plotted as a function of the laboratory beam momentum and fitted with an exponential distribution as specified in Figure C.2 in the momentum range of interest ($(20 \leq p_{lab} \leq 60)$GeV/$c$). The resulting values for the total proton–proton cross sections are given in Table C.2.

The slope parameter C of the proton–proton differential cross section, C, has been determined as a function of the momentum by fitting as stated in Figure C.3 the available measurements [145, 146] in the momentum range of interest. The resulting values for the slope parameters as well as the quasi-elastic cross sections are given in Table C.2.

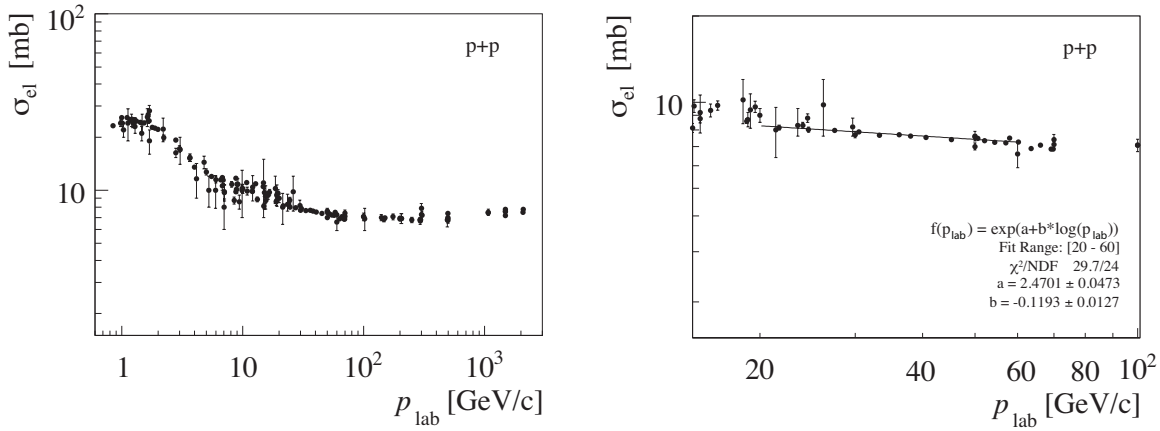

Figure C.4: All elastic cross sections for p+p collisions from [4] as a function of the laboratory beam momentum (p_{lab}) (left) and the ones fitted in the range of ($20 \leq p_{lab} \leq 60$) GeV/c (right).

p_{lab} [GeV/c]	$\sigma_{el}(pp)$ **[mb]**	σ_{qe} **[mb]**	
		$N(A) = 3.4$	$N(A) = 1.6A^{1/3}$
20	8.3 ± 0.5	28.1 ± 1.7	30.3 ± 1.8
30	7.9 ± 0.5	26.8 ± 1.7	28.9 ± 1.8
30.8	7.9 ± 0.5	26.7 ± 1.7	28.8 ± 1.8
40	7.6 ± 0.5	25.9 ± 1.7	27.9 ± 1.9
50	7.4 ± 0.5	25.2 ± 1.7	27.2 ± 1.9
60	7.3 ± 0.5	24.7 ± 1.7	26.6 ± 1.9

Table C.3: The elastic p+p cross section ($\sigma_{el}(pp)$), the factor C and the quasi-elastic cross section (σ_{qe}) for $N(A) = 3.4$ as measured by [117] and $N(A) = 1.6A^{1/3}$ at different laboratory beam momenta.

C.3 Approximation II

According to [117], the quasi-elastic proton–carbon cross section at a given momentum can also be evaluated from the elastic proton–proton cross-section $\sigma_{el}(pp)$ at the respective momentum using the following approximation

$$\sigma_{qe} = N(A)\sigma_{el}(pp) \quad . \tag{C.2}$$

where, $N(A)$ is again the factor describing the effective number of nucleons taking part in the incoherent process for target nuclei of mass A (see Section C.2). In order to obtain the elastic proton–proton cross section at a given momentum, all available measurements summarized in [4] have been plotted as a function of laboratory beam momentum (p_{lab}) and fitted with an exponential distribution in the range of interest ($(20 \leq p_{lab} \leq 60)$ GeV/c) (see Figure C.4). The resulting values for the elastic proton–proton and quasi-elastic cross sections are given in Table C.3.

C.4 Summary

The quasi-elastic proton–carbon cross sections from the different calculations presented in the previous sections are summarized in Table C.4. The results from the Glauber model (see Section C.1) are believed to give the most precise estimation of the quasi-elastic cross sections, as this formalism has offered a good overall description of a wide range of hadron-nucleus measurements. Comparison of the Glauber model values to the weighted mean of the respective results obtained from the two approximations presented in Sections C.2 and C.3, for which previous measurements on the total and elastic proton–proton cross sections have been taken into account, shows agreement within the assigned uncertainties. Only for the quasi-elastic cross section at 20 GeV/c a slightly larger discrepancy is observed, wherefore the error on the Glauber model calculation, as given in Table C.4, has been increased from 1.5 mb to the observed difference of 1.9 mb.

p_{lab}	**Approx. I [mb]**		**Approx. II [mb]**		$\langle$**Approx.**$\rangle$	**Glauber**
[GeV/c]	$N(A) = 3.4$	$= 1.6A^{1/3}$	$N(A) = 3.4$	$= 1.6A^{1/3}$	**[mb]**	**[mb]**
20	25.7 ± 2.9	27.7 ± 3.1	28.1 ± 1.7	30.3 ± 1.8	28.5	30.4 ± 1.9
30	24.4 ± 2.8	26.3 ± 3.0	26.8 ± 1.7	28.9 ± 1.8	27.1	28.0 ± 1.5
30.8	24.3 ± 2.8	26.2 ± 3.0	26.7 ± 1.7	28.8 ± 1.8	27.0	27.9 ± 1.5
40	23.5 ± 2.7	25.3 ± 3.0	25.9 ± 1.7	27.9 ± 1.9	26.1	26.5 ± 1.5
50	22.5 ± 2.7	24.2 ± 2.9	25.2 ± 1.7	27.2 ± 1.9	25.3	25.6 ± 2.0
60	22.3 ± 2.7	24.0 ± 2.9	24.7 ± 1.7	26.6 ± 1.9	24.8	26.2 ± 2.0

Table C.4: The quasi-elastic cross sections from the two approximations presented in Sections C.2 and C.3, their weighted mean, and the Glauber model calculations described in Section C.1.

The quasi-elastic cross-sections have then been used to recalculate the measured cross sections from [118] and [119]. Resulting values on the recalculated values are given in Table C.5.

p_{lab} [GeV/c]	σ_{inel}^{pub} **[mb]**	σ_{qe} **[mb]**	σ_{inel}^{recalc} **[mb]**
20	249 ± 3 [118]	30.4 ± 1.9	279 ± 4
30	247 ± 4 [118]	28.0 ± 1.5	275 ± 4
40	246 ± 3 [118]	26.5 ± 1.5	273 ± 3
50	248 ± 3 [118]	25.6 ± 2.0	274 ± 4
60	252 ± 5 [118]	26.2 ± 2.0	278 ± 5
60	222 ± 7 [119]	26.2 ± 2.0	248 ± 7

Table C.5: The inelastic p+C cross section as published in [118] and [119] (σ_{inel}^{pub}), the quasi-elastic cross section (σ_{qe}) and the recalculated inelastic cross section (σ_{inel}^{recalc}), where σ_{qe} has been added to σ_{inel}^{pub}, for the respective laboratory beam momentum.

p_{lab} [GeV/c]	σ_{inel} **[mb]**	σ_{qe} **[mb]**	σ_{prod} **[mb]**
30.8	$257.2 \pm 1.9 \pm 8.9$	27.9 ± 1.5	$229.3 \pm 1.9 \pm 9.0$

Table C.6: The inelastic p+C cross section as measured in NA61, the quasi-elastic cross section (σ_{qe}) and the production cross section (σ_{prod}).

The comparison of the recalculated value from [119] to the measurement from NA61, as well as the published values from [117] and [118], is presented in Section 7.2. The resulting value of the production cross section at 30.8 GeV/c is given in Table C.6. In Chapter 8 it is used to normalize the particle yields measured with the NA61 detector.

Appendix D

Elastic and Quasi-Elastic Scattering Out of S4

GEANT4 simulations are used in this work to determine the corrections needed to obtain the total inelastic proton–carbon cross section from the measured trigger cross section (see Chapter 7). The total cross section (σ_{inel}) from GEANT4 as well as the total coherent elastic (σ_{el}) and quasi-elastic (σ_{qe}) ones have been cross-checked against available experimental measurements (see Table 7.2).

Next to that, also the fraction of the elastic and the quasi-elastic cross section in which the proton misses the S4 counter can be compared. To calculate this fraction from the total cross sections measured by previous experiments, one can use the measurement of the dependence of the differential proton–carbon cross section on the four-momentum transfer squared ($|t|$) (see Section 7.1) published in [117] and [145, 146] (see Figures D.1 and C.3). While the observed steep decline in the lower $|t|$-region can be explained by predominant coherent elastic scattering, where the nucleus remains close to its ground state, the events at larger $|t|$ can instead be described by leading quasi-elastic scattering, in which one of the nucleons present in the nucleus recoils violently enough to break the nuclear bond (~ 8 MeV). The results at the smallest angles, thus, give information about the nuclear form factor of carbon, while those at the largest angles give information about the probability that proton–nucleon elastic collisions take place in the nucleus. It has been found that the lower $|t|$-region is described by

$$\frac{\mathrm{d}\sigma}{\mathrm{d}\Omega} = Ae^{-67t} \quad , \tag{D.1}$$

with $\mathrm{d}\Omega$ denoting the solid angle unit. Using $\mathrm{d}\Omega = \mathrm{d}t$, which is true for small angles ($\sin\Theta \approx \Theta$), and using the measurement of the total coherent elastic contribution from [117] one can

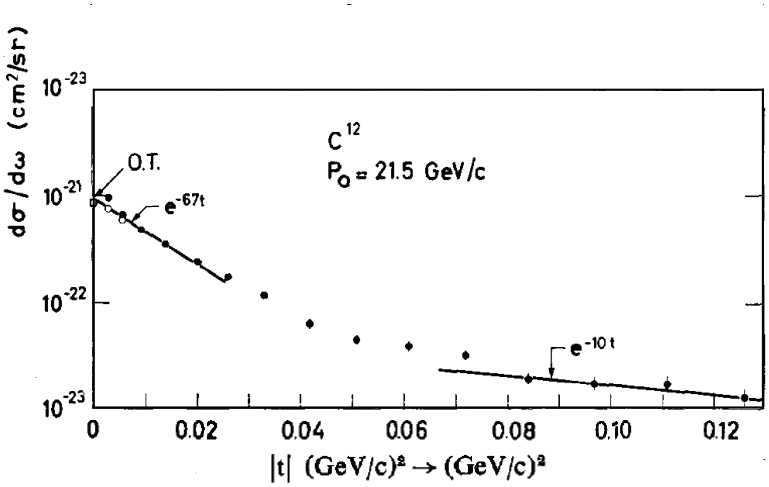

Figure D.1: Differential p+C cross section at 21.5 GeV/c laboratory beam momentum as a function of the four-momentum transfer squared (black dots: experimental results, open circles: experimental cross sections after subtracting the Coulomb contribution, O.T.: optical theorem cross section). The fit to the first points gives the nuclear form factor, while the fit to the points at larger $|t|$ has the same slope (10 (GeV/c)^2) as exhibited by the p+p differential cross section. The figure is taken from: [117].

determine A

$$\int_0^\infty Ae^{-67t}\mathrm{d}t = 81 \pm 4 \;\rightarrow\; A = 5427 \pm 268 \quad . \tag{D.2}$$

Given the fact that S4 has an angular acceptance of 2.7 mrad, which, for 30.8 GeV/c protons, corresponds to $t = 6.9 \times 10^{-3}$ (GeV/c)^2, one can then calculate the elastic contribution out of S4

$$\int_{6.9\times10^{-3}}^\infty Ae^{-67t}\mathrm{d}t = 51 \pm 3 \quad . \tag{D.3}$$

The fraction of events with elastic scattering outside of S4 is therefore 63%. Its comparison to the value obtained from GEANT4 simulations is presented in Table 7.2.

The same method can be used to calculate the fraction of the quasi-elastic contribution out of S4. For that, one can use the measured dependence of the differential proton–carbon cross section on the four-momentum transfer squared in the large $|t|$-region, which is described by

$$\frac{\mathrm{d}\sigma}{\mathrm{d}\Omega} = Ae^{-Ct} \quad . \tag{D.4}$$

Here, a slope parameter of $C = 10.7 \pm 1.2$ at 30.8 GeV/c is used, which results from the fit to all the available measurements [145, 146] on the slope parameter of the proton–proton differential

cross section as a function of the proton momentum (see Figure C.3 and Table C.2). Using the total quasi-elastic cross section for 30.8 GeV/c, as given in Table 7.2, one can determine the respective quantity A

$$\int_0^\infty Ae^{-Ct}\mathrm{d}t = 27.9 \pm 1.5 \;\rightarrow\; A = 298.5 \pm 37.1 \quad . \tag{D.5}$$

and calculate the quasi-elastic contribution out of S4

$$\int_{6.9\times10^{-3}}^\infty Ae^{-Ct}\mathrm{d}t = 26.0 \pm 4.4 \quad . \tag{D.6}$$

The fraction of events with quasi-elastic scattering outside of S4 thus amounts to 93%. Comparison of this value to the one obtained from GEANT4 simulations is again presented in Table 7.2.

Bibliography

[1] E. Fermi, *Versuch einer Theorie der β-Strahlen*, Z. Phys. **88** 161 (1934).

[2] W. Cottingham and D. A. Greenwood, *An Introduction to the Standard Model of Particle Physics*, Cambridge University Press, ISBN 0-521-58832-4 (1998).

[3] Y. Itow *et al.* [T2K Collaboration], *The JHF-Kamioka neutrino project,* Nucl. Phys. Proc. Suppl. **111**, 146 (2001).

[4] C. Amsler *et al.* [Particle Data Group], *Review of particle physics*, Phys. Lett. **B667**, 1 (2008).

[5] M. Gell-Mann, P. Ramond and R. Slansky, *Complex spinors and unified theories*, Supergravity Workshop, Stony Brook, 315 (1979).

[6] T. Yanagida, *Horizontal symmetry and masses of neutrinos*, Progress of Theoretical Physics **64**, 1103 (1980).

[7] T. Bloxham *et al.* [COBRA Collaboration], *First results on double beta decay of Cd, Te and Zn isotopes with the COBRA experiment,* Phys. Rev. **C76**, 025501 (2007).

[8] C. Arnaboldi *et al.* [CUORICINO Collaboration], *Results from a search for the 0 neutrino beta beta-decay of Te-130,* Phys. Rev. **C78**, 035502 (2008).

[9] A. M. Bakalyarov *et al.*, *Results of the experiment on investigation of Germanium-76 double beta decay,* Phys. Part. Nucl. Lett. **2**, 77 (2005).

[10] C. E. Aalseth *et al.* [IGEX Collaboration], *The Igex 76ge Neutrinoless Double-Beta Decay Experiment,* Phys. Rev. **D65**, 092007 (2002).

[11] J. Argyriades *et al.* [NEMO Collaboration], *Measurement of the Double Beta Decay Halflife of 150-Nd and Search for Neutrinoless Decay Modes with the NEMO-3 Detector,* Phys. Rev. **C80**, 032501 (2009).

[12] B. Pontecorvo, *Neutrino experiments and the problem of conservation of leptonic charge,* Zh. Eksp. Teor. Fiz. **53**, 1717 (1967).

[13] Z. Maki, M. Nakagawa and S. Sakata, *Remarks on the Unified Model of Elementary Particles,* Progress of Theoretical Physics **28**, 870 (1962).

[14] L. Wolfenstein, *Neutrino oscillations in matter,* Phys. Rev. D. **17(9)**, 2369 (1978).

[15] S. P. Mikheyev and A. Y. Smirnov, *Resonance enhancement of oscillations in matter and solar neutrino spectroscopy,* Yad. Fiz **42**, 1441 (1985).

[16] B. T. Cleveland *et al.*, *Measurement of the solar electron neutrino flux with the Homestake chlorine detector,* Astrophys. J. **496**, 505 (1998).

[17] J. N. Abdurashitov *et al.* [SAGE Collaboration], *Measurement of the solar neutrino capture rate with gallium metal. III: Results for the 2002–2007 data-taking period,* Phys. Rev. **C80**, 015807 (2009).

[18] W. Hampel *et al.* [GALLEX Collaboration], *GALLEX solar neutrino observations: results for GALLEX IV,* Phys. Lett. **B447**, 127 (1999).

[19] M. Altmann *et al.* [GNO Collaboration], *Complete results for five years of GNO solar neutrino observations,* Phys. Lett. **B616**, 174 (2005).

[20] K. S. Hirata *et al.* [KAMIOKANDE-II Collaboration], *Experimental Study of the Atmospheric Neutrino Flux,* Phys. Lett. **B205**, 416 (1988).

[21] J. Hosaka *et al.* [Super-Kamiokande Collaboration], *Solar neutrino measurements in Super-Kamiokande-I,* Phys. Rev. **D73**, 112001 (2006).

[22] J. P. Cravens *et al.* [Super-Kamiokande Collaboration], *Solar neutrino measurements in Super-Kamiokande-II,* Phys. Rev. **D78**, 032002 (2008).

[23] B. Aharmim *et al.* [SNO Collaboration], *Low-energy-threshold analysis of the Phase I and Phase II data sets of the Sudbury Neutrino Observatory,* Phys. Rev. **C81**, 055504 (2010).

[24] C. Arpesella *et al.* [Borexino Collaboration], *Direct Measurements of the ^{7}Be Solar Neutrino Flux with 192 Days of Borexino Data,* Phys. Rev. Lett. **101**, 091302 (2008).

[25] S. Abe *et al.* [KamLAND Collaboration], *Precision Measurement of Neutrino Oscillation Parameters with KamLAND,* Phys. Rev. Lett. **100**, 221803 (2008).

[26] J. N. Bahcall, http://www.sns.ias.edu/ jnb.

[27] P. Adamson *et al.* [MINOS Collaboration], *Measurement of Neutrino Oscillations with the MINOS Detectors in the NuMI Beam,* Phys. Rev. Lett. **101**, 131802 (2008).

[28] S. Fukuda *et al.* [Super-Kamiokande Collaboration], *Determination of solar neutrino oscillation parameters using 1496 days of Super-Kamiokande I data,* Phys. Lett. **B539**, 179 (2002).

[29] B. Aharmim *et al.* [SNO Collaboration], *Electron Energy Spectra, Fluxes, and Day-Night Asymmetries of 8B Solar Neutrinos from the 391-Day Salt Phase SNO Data Set,* Phys. Rev. **C72**, 055502 (2005).

[30] K. Eguchi *et al.* [KamLAND Collaboration], *First results from KamLAND: Evidence for reactor anti-neutrino disappearance,* Phys. Rev. Lett. **90**, 021802 (2003).

[31] W. Gajewski *et al.* [IMB Collaboration], *A search for oscillation of atmospheric neutrinos with the IMB detector,* Nucl. Phys. Proc. Suppl. **28A**, 161 (1992).

[32] Y. Fukuda *et al.* [Super-Kamiokande Collaboration], *Evidence for oscillation of atmospheric neutrinos,* Phys. Rev. Lett. **81**, 1562 (1998).

[33] K. Daum *et al.* [Frejus Collaboration], *Determination of the atmospheric neutrino spectra with the Frejus detector,* Z. Phys. **C66**, 417 (1995).

[34] M. Aglietta *et al.* [NUSEX Collaboration], *Experimental study of atmospheric neutrino flux in the NUSEX experiment,* Europhys. Lett. **8**, 611 (1989).

[35] M. Ambrosio *et al.* [MACRO Collaboration], *Atmospheric neutrino oscillations from upward through going muon multiple scattering in MACRO,* Phys. Lett. **B566**, 35 (2003).

[36] M. C. Sanchez *et al.* [Soudan-2 Collaboration], *Measurement of the L/E distributions of atmospheric neutrinos in Soudan 2 and their interpretation as neutrino oscillations,* Phys. Rev. **D68**, 113004 (2003).

[37] M. H. Ahn, *et al.* [K2K Collaboration], *Measurement of Neutrino Oscillation by the K2K Experiment,* Phys. Rev. **D74**, 072003 (2006).

[38] D. G. Michael *et al.* [MINOS Collaboration], *Observation of muon neutrino disappearance with the MINOS detectors and the NuMI neutrino beam,* Phys. Rev. Lett. **97**, 191801 (2006).

[39] N. Agafonova *et al.* [OPERA Collaboration], *Observation of a first ν_τ candidate in the OPERA experiment in the CNGS beam,* Phys. Lett. **B691**, 138 (2010).

[40] T. K. Gaisser, *Atmospheric neutrino fluxes,* Phys.Scripta **T121**, 51 (2005).

[41] Y. Ashie *et al.* [Super-Kamiokande Collaboration], *Evidence for an oscillatory signature in atmospheric neutrino oscillation,* Phys. Rev. Lett. **93**, 101801 (2004).

[42] V. D. Barger *et al.*, *Neutrino decay and atmospheric neutrinos,* Phys. Lett. **82**, 109 (1999).

[43] E. Lisi, A. Marrone and D. Montanino, *Probing possible decoherence effects in atmospheric neutrino oscillations,* Phys. Rev. Lett. **85**, 1166 (2000).

[44] P. Adamson *et al.* [MINOS Collaboration], *Measurement of Neutrino Oscillations with the MINOS Detectors in the NuMI Beam,* Phys. Rev. Lett. **101**, 131802 (2008).

[45] Y. Ashie *et al.* [Super-Kamiokande Collaboration], *A Measurement of atmospheric neutrino oscillation parameters by SUPER-KAMIOKANDE I,* Phys. Rev. **D71**, 112005 (2005).

[46] K. Kodama *et al.* [DONUT Collaboration], *Observation of tau neutrino interactions,* Phys. Lett. **B504**, 218 (2001).

[47] M. Apollonio *et al.* [CHOOZ Collaboration], *Search for neutrino oscillations on a long baseline at the CHOOZ nuclear power station,* Eur. Phys. J. **C27**, 331 (2003).

[48] F. Boehm *et al.* [Palo Verde Collaboration], *Final results from the Palo Verde neutrino oscillation experiment,* Phys. Rev. **D64**, 112001 (2001).

[49] M. Mezzetto and T. Schwetz, *θ_{13}: phenomenology, present status and prospect,* arXiv:1003.5800 (2010).

[50] I. Ambats *et al.* [NOνA Collaboration], *NOνA proposal to build a 30-kiloton off-axis detector to study neutrino oscillations in the Fermilab NuMI beamline,* hep-ex/0503053 (2004).

[51] X. Guo *et al.* [Daya-Bay Collaboration], *A precision measurement of the neutrino mixing angle θ_{13} using reactor antineutrinos at Daya Bay,* hep-ex/0701029 (2007).

[52] F. Ardellier *et al.* [Double Chooz Collaboration], *Double Chooz: A search for the neutrino mixing angle θ_{13},* hep-ex/0606025 (2006).

[53] J. K. Ahn *et al.* [RENO Collaboration], *RENO: An experiment for Neutrino Oscillation Parameter θ_{13} Using REactor Neutrinos at Yonggwang,* 1003.1391 (2010).

[54] V. Barger, D. Marfatia and K. Whisnant, *Breaking eightfold degeneracies in neutrino CP violation, mixing, and mass hierarchy,* Phys. Rev. **D65**, 073023 (2002).

[55] M. Ishitsuka *et al.*, *Resolving Neutrino Mass Hierarchy and CP Degeneracy by Two Identical Detectors with Different Baselines,* Phys. Rev. **D72**, 033003 (2005).

[56] A. Badertscher *et al.*, *A Possible Future Long Baseline Neutrino and Nucleon Decay Experiment with a 100 kton Liquid Argon TPC at Okinoshima using the J-PARC Neutrino Facility,* 0804.2111 (2008).

[57] C. Volpe, *Topical review on beta-beams,* J. Phys. **G34**, R1 (2007).

[58] *International design study of the neutrino factory,* http://www.ids-nf.org.

[59] J. Bernabeu *et al.*, *EUROν WP6 2009 yearly report: Update of the physics potential of Nufact, superbeams and betabeams,* arXiv:1005.3146v1 (2010).

[60] D. Beavis *et al.*, Proposal of BNL AGS E-889 (1995).

[61] A. A. Aguilar-Arevalo *et al.* [MiniBooNE Collaboration], *The MiniBooNE Detector*, Nucl. Instrum. Meth. **A599**, 28 (2009).

[62] N. V. Mokhov *et al.*, *The MARS Monte Carlo*, Fermilab FN-628 (1995).

[63] FLUKA, http://www.fluka.org/fluka.php.

[64] M. Bonesini *et al.*, *On Particle production for high-energy neutrino beams*, Eur. Phys. J. **C20**, 12 (2001).

[65] J.R. Sanford and C.L. Wang, AGS Internal Reports, BNL-11479 & BNL-11299, Brookhaven National Laboratory, unpublished (1967).

[66] C. L. Wang, *Pion, Kaon, and Antiproton Production Between 10 and 70 BeV*, Phys. Rev. Lett. **25**, 1068 (1970).

[67] S. Kopp, *Accelerator Neutrino Beams*, Phys. Rept.**439**, 101 (2007).

[68] G. Ambrosini *et al.* [NA56/SPY Collaboration], *Measurement of charged particle production from 450-GeV/c protons on beryllium*, Eur. Phys. J. **C10**, 605 (1999).

[69] S. Afanasev *et al.* [NA49 Collaboration], *The NA49 large acceptance hadron detector*, Nucl. Instrum. Meth. A **430** 210 (1999).

[70] M. G. Catanesi *et al.* [HARP Collaboration], *Proposal to study hadron production for the neutrino factory and for the atmospheric neutrino flux*, CERN-SPSC-99-35.

[71] M. G. Catanesi *et al.* [HARP Collaboration], *The HARP detector at the CERN PS*, Nucl. Instrum. Meth. **A571**, 527 (2007).

[72] M. G. Catanesi *et al.* [HARP Collaboration], *Measurement of the production cross-section of positive pions in p–Al collisions at 12.9 GeV/c*, Nucl. Phys. **B732**, 1 (2006).

[73] M. G. Catanesi *et al.* [HARP Collaboration], *Measurement of the production cross-section of positive pions in the collision of 8.9 GeV/c protons on beryllium*, Eur. Phys. J. **C52**, 29 (2007).

[74] I. Chemakin *et al.* [E910 Collaboration], *Pion production by protons on a thin beryllium target at 6.4 GeV/c, 12.3 GeV/c, and 17.5 GeV/c incident proton momenta*, Phys. Rev. **C77**, 015209 (2008).

[75] M. G. Catanesi *et al.* [HARP Collaboration], *Measurement of the production cross-sections of $\pi^{\pm}$ in p–C and $\pi^{\pm}$–C interactions at 12 GeV/c*, Astropart. Phys. **29**, 257 (2008).

[76] A. A. Aguilar-Arevalo *et al.* [MiniBooNE Collaboration], *A Search for electron neutrino appearance at the $\Delta m^2 \sim 1eV^2$ scale*, Phys. Rev. Lett. **98**, 231801 (2007).

[77] E. Aliu *et al.* [K2K Collaboration], *Evidence for Muon Neutrino Oscillation in an Accelerator-Based Experiment*, Phys. Rev. Lett. **94**, 081802 (2005).

[78] H. Meyer *et al.* [MIPP Collaboration], *The main injector particle production experiment (MIPP) at Fermilab*, J. Phys. Conf. Ser. **69**, 0120225 (2007).

[79] D. A. Crane *et al.* [NuMI Beam Group], *Status report: Technical design of neutrino beams for the Main Injector (NuMI)*, FERMILAB-TM-1946, NUMI-B-92 (1995).

[80] J. Paley *et al.* [MIPP Collaboration], *First results from MIPP*, AIP Conf. Proc. **981**, 154 (2008).

[81] N. Antoniou *et al.* [NA61 Collaboration], *Study of Hadron Production in Collisions of Protons and Nuclei at the CERN SPS,* CERN-SPSC-2006-034.

[82] N. Antoniou *et al.* [NA61 Collaboration], *Additional Information Requested in the Proposal Review Process,* CERN-SPSC-2007-004.

[83] N. Abgrall *et al.* [NA61 Collaboration], *Further Information Requested in the Proposal Review Process,* CERN-SPSC-2007-019.

[84] N. Abgrall *et al.* [NA61 Collaboration], *Calibration and Analysis of the 2007 Data,* CERN-SPSC-2008-018.

[85] *$T2K - ND280$ Collaboration*, http://www.nd280.org..

[86] B. Still, *T2K ND280 π^0 Electromagnetic Calorimeter,* Ph.D. thesis, University of Sheffield (2009).

[87] C. Giganti and M. Zito, *Study of the T2K beam electron neutrino component with the ND280 tracking detectors,* T2K-TN-009 (2009).

[88] T2K Collaboration, http://www.t2k.org.

[89] J. Albert, *Plots of T2K Sensitivity to θ_{13} for the 30 GeV ν_μ beam,* T2K-SK group report, July 17, 2009.

[90] L. Esposito for NA61/SHINE and T2K Collaborations, *NA61/SHINE data for T2K flux calculation,* Poster prepared for Neutrino 2010, Athens, Greece (2010).

[91] N. Abgrall, B. Popov and J.-M. Levy, *Predictions of neutrino fluxes for T2K: NA61 analysis and data taking strategy,* NA61/T2K Internal note 2009-01 draft 2.1 (2010).

[92] *GEANT: Detector Description and Simulation Tool,* CERN Programming Library Long Writeup W5013, GEANT version 3.21.

[93] *GCALOR Simulation Package,* http://www.staff.uni-mainz.de/zeitnitz/Gcalor/gcalor.html.

[94] C. Meurer *et al.* [HARP Collaboration], *New p+C data in fixed target experiments and the muon component in extensive air showers,* arXiv:astro-ph/0612157v1.

[95] C. Alt *et al.* [NA49 Collaboration], *Inclusive production of charged pions in p + C collisions at 158-GeV/c beam momentum,* Eur. Phys. J. C **49** (2007) 897.

[96] K. Matsuoka, Contributions to the T2K beam MC group meetings (2009-2010).

[97] Internal NA61-T2K document on T2K requirements on NA61 data taking (2009).

[98] J. Abraham *et al.* [Pierre Auger Collaboration], *Properties and performance of the prototype instrument for the Pierre Auger Observatory,* Nucl. Instrum. Meth. A **523** 50 (2004).

[99] T. Antoni *et al.* [KASCADE Collaboration], *The Cosmic ray experiment KASCADE,* Nucl. Instrum. Meth. A **513** 490-510 (2003).

[100] D. Varga, *Study of Inclusive and Correlated Particle Production in Elementary Hadronic Interactions*, Ph.D. thesis, University Budapest (2003).

[101] G. Brianti, *The CERN Synchrotrons*, Presented at : CAS - CERN Accelerator School (1996).

[102] The PS Staff, *40 years of CERN's Proton Synchrotron*, CERN Courier **39** (10) (1999).

[103] The Large Hadron Collider Project, http://lhc.web.cern.ch/.

[104] M. Posiadala, *Measurements of hadron production for neutrino and cosmic-ray physics – program of the NA61/SHINE experiment at CERN SPS*, In proceedings of ISMD Conference, Gomel Region, Belarus (2009).

[105] C. Strabel, *Hadro-production measurements for the T2K experiment with the NA61/ SHINE detector at the CERN SPS*, Presented at WIN'09 Conference, Perugia, Italy (2009).

[106] R. Zybert and P. Buncic, *DSPACK: Object manager for high energy physics*, Prepared for International Conference on Computing in High-energy Physics (CHEP 95), Rio de Janeiro, Brazil, 18-22 Sep 1995.

[107] D. Irmscher, *Philosophy and parts of the global tracking chain*, NA49 Note number **131** (1997).

[108] C. Strabel, *Energieabhängigkeit der K_s^0-Produktion in zentralen Pb+Pb Reaktionen*, Diploma thesis, Goethe University Frankfurt (2006).

[109] C. Meurer, $\overline{\Xi}^-$- *und* $\overline{\Xi}^+$- *Produktion in Pb+Pb Stößen bei 40 AGeV am CERN SPS*, Diploma thesis, Goethe University Frankfurt (2003).

[110] The ROOT System, http://root.cern.ch/.

[111] R. Brun and F. Rademakers, *ROOT: An object oriented data analysis framework*, Nucl. Instrum. Meth. A **389** 81 (1997).

[112] ROOT61 Documentation, https://na61.web.cern.ch/na61/pages/root61/.

[113] C. Strabel, Contributions to the NA61 analysis meetings (2008-2010).

[114] M. Posiadala, Private Communication.

[115] C. Alt *et al.* [NA49 Collaboration], *Inclusive production of charged pions in p + p collisions at 158-GeV/c beam momentum,* Eur. Phys. J. C **45** (2006) 343.

[116] S. Agostinelli *et al.* [GEANT4 Collaboration], *GEANT4: A simulation toolkit,* Nucl. Instrum. Meth. A **506**, 250 (2003).

[117] Bellettini *et al.*, *Proton-Nuclei Cross-Section at 20 GeV,* Nucl. Phys. **79**, 609 (1966).

[118] S. P. Denisov *et al.*, *Absorption Cross-Sections For Pions, Kaons, Protons And Anti-Protons On Complex Nuclei In The 6-Gev/C To 60-Gev/C Momentum Range,* Nucl. Phys. B **61**, 62 (1973).

[119] A. S. Carroll *et al.*, *Absorption Cross-Sections Of Pi+-, K+-, P And Anti-P On Nuclei Between 60-Gev/C And 280-Gev/C,* Phys. Lett. B **80**, 319 (1979).

[120] C. Strabel, *Update on Cross Section Normalization,* Presentation given at the NA61 Collaboration Meeting, CERN, June 2010.

[121] N. Abgrall, Ph.D. Thesis in preparation, University of Geneva, Geneva Switzerland.

[122] C. Bovet *et al.*, *The CEDAR counters for particle identification in the SPS secondary beams : A description and an operation manual,* CERN-82-13 (1982).

[123] M. Posiadala, Ph.D. Thesis in preparation, University of Warsaw, Warsaw Poland.

[124] S. Murphy, Ph.D. Thesis in preparation, University of Geneva, Geneva Switzerland.

[125] W. Rauch *et al.* [The NA49 Collaboration], *The NA49 Data Acquisition System*, IEEE Trans. Nucl. Instrum. Meth. **A 451**, 416 (2000).

[126] E. Dénes *et al.*, *The NA61 TPC Read-Out*, Document Reference Number: NA 61 TPC Read-out (2009).

[127] T. Palczewski, Ph.D. Thesis in preparation, University of Warsaw, Warsaw Poland.

[128] C. Strabel, *Cross Section Normalization*, Presented at NA61 Software and Analysis Meeting, Cracow, February 2009.

[129] C. Strabel, *Update on S4 Bias Correction*, Presented at NA61 T2K/CR Analysis Meeting, November 2010.

[130] T. Palczewski, Private Communication.

[131] The GEANT4 Collaboration, *GEANT4 recommended physics lists*, http://www.geant4.org/geant4/support/physicsLists/referencePL/useCases.shtml (2009).

[132] G. Folger *et al.*, *String parton models in Geant4*, In CHEP-2003-MOMT008, La Jolla, California (2003).

[133] H. W. Bertini, *Low-energy intranuclear cascade calculation*, Phys. Rev.**131**, 1801 (1963).

[134] A. Heikkinen *et al.*, *Bertini intra-nuclear cascade implementation in Geant4*, In CHEP-2003-MOMT008, La Jolla, California (2003).

[135] A. Marchionni *et al.*, *Cross-Section Normalization in NA61,* NA61 Internal note 2009-02, draft 0.1 (2009).

[136] K. Werner, *Strings, pomerons, and the venus model of hadronic interactions at ultra-relativistic energies*, Phys. Rept. **232**, 87 (1993).

[137] N. Abgrall *et al.* [NA61 Collaboration], *Cross Section and Charged Pion Spectra in Proton–Carbon Interactions at 31 GeV/c*, to be submitted to Phys. Rev. C.

[138] *The UrQMD Model*, http://urqmd.org/.

[139] C. Strabel, *Hadro-production measurements for T2K by NA61/SHINE at the CERN SPS*, In proceedings of Lake Louise Winter Institute 2010.

[140] M. Hartz, Private Communication.

[141] R. Engel, Private Communication.

[142] R. J. Glauber, *Cross Sections in Deuterium at High Energies*, Phys. Rev. **100**, 242 (1955).

[143] R. J. Glauber and G. Matthiae, *High-energy scattering of protons by nuclei*, Nucl. Phys. **B21**, 135 (1970).

[144] R. P. V. Murthy *et al.*, *Neutron total cross sections on nuclei at Fermilab energies*, Nucl. Phys. **B92**, 269 (1975).

[145] G. G. Beznogikh *et al.*, *The slope parameter of the differential cross-section of elastic p–p scattering in energy range 12–70 GeV*, Phys. Lett. **30B**, 274 (1969).

[146] G. Bellettini *et al.*, *Absolute measurements of proton–proton small angle elastic scattering and total cross sections at 10, 19 and 26 GeV/c*, Phys. Lett. **14**, 164 (1965).

List of Figures

List of Tables